Formation of Salt Crystal Whiskers on Nanoporous Coatings and Coating onto Open Celled Foam

A DISSERTATION
SUBMITTED TO THE FACULTY OF THE GRADUATE SCHOOL
OF THE UNIVERSITY OF MINNESOTA
BY

Heng Zhang

IN PARTIAL FULFILLMENT OF THE REQUIREMENTS
FOR THE DEGREE OF
DOCTOR OF PHILOSOPHY

Lorraine F. Francis, Advisor

January 2012

© Heng Zhang 2012

ACKNOWLEDGEMENTS

I would like to thank many people who gave me help during my graduate study and made it a memorable experience. First and most importantly, I offer my sincerest gratitude to my advisor, Dr Lorraine F. Francis, who supported me throughout my graduate study. This thesis would not have been possible without her guidance, patience and encouragement.

I also want to thank previous group member Dr. Zhen Wu, who started the whisker project and shared with me his valuable experience.

I owe my deepest gratitude to professor Michael Tsapatsis and research fellow Wieslaw Suszynski for their guidance and help in foam coating project.

I thank all my colleagues, Tim Reynolds, Sreeram Kalpathy, Jin-Oh Song, Kumar Varoon, Erica Redline, Dr. Hui Luo, Dr. Karan Jindal, Dr. Qiang Lan and Dr. Christine Cardinal Roberts for their help in different ways.

I am grateful to the research funding from Petroleum Research Fund, the generous supporters who established the Shell Profesorship, the L.E. Scriven Chair and the ADMIRE Coating Process Fundamentals Program.

Finally and most importantly, my parents, Ms. DanPing Zhu and Mr. ZhongYuan Zhang deserve my deepest thanks for their love and support, which allow me to get to where I am today.

ABSTRACT

Salt crystal whiskers were grown from salt solution saturated nanoporous silica coatings. Coated substrates were partially immersed into an aqueous potassium chloride solution and then kept in a controlled relative humidity chamber for whisker growth. The salt solution was first wicked into the coating by capillary action, and then evaporation ensued and a supersaturated condition was reached. Crystals grew from the surface by a base growth mechanism in which salt ions were added to the surface of the crystal that was in contact with the nanoporous coating. Optical microscopy and SEM results demonstrated this mechanism. Crystals with whisker morphologies, typically 2 - 50 μm in lateral dimension and up to ~1 cm in length, emerged from the coating surface at a position above the original liquid level. Sheet-like crystals also formed from whiskers that had fallen flat onto the porous coating surface. Inspired by the sheet formation mechanism and liquid transportation phenomenon, a seeding technique was developed to reduce whisker width. Attritor ground salt particles were placed on the nanoporous coating surface to initiate simultaneous whiskers growth and salt nano-whiskers with lateral dimension as small as 50 nm were obtained on the surface of the coating. This crystal growth method can be applied to different materials, namely water soluble materials, and creates whisker crystals with controllable size and location on the nanoporous coating.

Open celled foam is a three dimensional structure. In some applications, other materials are coated on internal surface of the foam to provide desired final product functionality. Because of their complicated 3D structures, coating onto foam is challenging. A new coating process that combines dip coating and spin coating was developed. Dip coating step was used to load the solution into the foam and a spin treatment step was added to remove the trapped liquid and redistribute the liquid to obtain uniform coating. The dip and spin process was also used to create γ-alumina and zeolite coatings, which are of interest for catalysis applications.

TABLE OF CONTENTS

LIST OF TABLES ..... **vi**

LIST OF FIGURES ..... **vii**

CHAPTER 1 BACKGROUND AND OVERVIEW **1**

1.1 History of Whiskers 1
1.2 Fundamental Theory of Crystal Growth 3
1.3 NaCl Crystal Nucleation and Growth on Atomic Level 18
1.4 History of Whisker Growth on Porous Media 22
1.5 Background of Whisker Growth Mechanism. 26
1.5.1 Tip Growth Mechanism from Sears *26*
1.5.2 Base Growth Mechanism from Shichiri *30*
1.5.3 Base Growth Mechanism from Amelinckx. *31*
1.6 Motivation and Objective 34
1.7 Potassium Chloride 36
1.8 Overview of Thesis Structure 37

CHAPTER 2 WHISKER GROWTH ON NANOPOROUS COATING **40**

2.1 Introduction 40
2.2 Whisker Growth under Standard Growth Condition 42
2.2.1 Experimental Section *42*
2.2.2 Results *46*
2.2.3 Discussion *60*
2.3 Conclusion 71

CHAPTER 3 OTHER FACTORS INFLUENCING WHISKER GROWTH **72**

3.1 Effect of Coating Thickness on Whisker Growth 72
3.1.1 Experimental *72*
3.1.2 Results *73*
3.1.3 Discussion *74*
3.2 Effect of Porous Coating Particle Size on Whisker Growth 75
3.2.1 Experimental *75*
3.2.2 Results *77*
3.2.3 Discussion *83*
3.3 Effect of Growth Angle on Whisker Growth 87
3.3.1 Experiment *87*
3.3.2 Results *89*
3.3.3 Discussion *90*
3.4 Cryo SEM study of liquid supporting layer 99
3.4.1 Experimental *99*
3.4.2 Results *100*

3.4.3 Discussion *106*
3.5 WHISKER GROWTH BY FREE PARTICLE METHOD 110
3.5.1 Experimental *110*
3.5.2 Results *110*
3.5.3 Discussion *112*

CHAPTER 4 WHISKER SIZE CONTROL 114

4.1 INTRODUCTION 114
4.2 EXPERIMENTAL 117
4.2.1 Whisker Growth on Patterned Porous Coating *117*
4.2.2 Whisker Growth by Seeding. *118*
4.3 RESULTS AND DISCUSSION 120
4.3.1 Liquid supply at the whisker base *120*
4.3.2 Whisker growth on patterned porous coating *125*
4.3.3 Whisker growth by seeding *127*
4.4 FUTURE WORK 142
4.4.1 Whisker Size Control *142*
4.4.2 Examination of Dislocation *143*
4.4.3 Growth of Whisker of Other Materials *143*
4.4.4 Applications of Whisker *144*

CHAPTER 5 COATING ONTO OPEN CELLED FOAM 146

5.1 INTRODUCTION 146
5.2 EXPERIMENTAL MATERIALS AND METHODS 148
5.2.1 Solid foams *148*
5.2.2 Model coating solutions *148*
5.2.3 Dip coating *149*
5.2.4 Spin treatment *151*
5.2.5 Alumina coatings *152*
5.2.6 Zeolite coatings *153*
5.3 RESULTS AND DISCUSSION 155
5.3.1 Dip coating *155*
5.3.2 Spin treatment *164*
5.3.3 Alumina and zeolite coatings *169*

CHAPTER 6 SUMMARY 174

REFERENCES 178

LIST OF TABLES

Table 1.1 Statistics on the sum of created and decayed nuclei during the 1.2ns MD simulations with 43% supersaturation at 298K. Table adapted from[28]. 19

Table 1.2 Whiskers growth on various porous substrate. Adapted from[33]. 22

Table 1.3 Properties of potassium chloride.....36

Table 2.1 Conditions used for 2-day whisker growth studies 44

Table 3.1 Thicknesses of coating composed of different particle size. 77

Table 3.2 Ratio of surface tension force to gravity force (whisker weight). Assuming whisker aspect ratio is 100. 93

Table 3.3 Ratio of $\tau_{support}$ / τ_{fall} at different tilt angle θ for tilted whisker if whisker aspect ratio is 100. 96

Table 3.4 Ratio of $\tau_{support}$ to τ_{fall} at different tilt angle θ for tilted whisker if whisker aspect ratio is 1000....97

Table 3.5 Ratio of $\tau_{support}$ to τ_{fall} at different tilt angle θ for tilted whisker if whisker aspect ratio is 100 and whisker growth angle is 90°. 98

Table 5.1 Viscosity and surface tension of glycerol/water solutions 149

LIST OF FIGURES

Figure 1.1 (a) Early photograph of spontaneously growing tin whiskers from Bell Laboratories investigation of electrical short circuit failures from tin plated details in telephone switching equipment in the 1940's.Adapted from [4](b) an optical images of sodium chloride whisker grown. Adapted from[5]. 1

Figure 1.2 Solubility dependence of various salts on temperature. Adapted from[18].....3

Figure 1.3 The concentration-temperature diagram. Adapted from[20]. 5

Figure 1.4 Free energy diagram for nucleation explaining the existence of a critical nucleus. Adapted from[20].....8

Figure 1.5 A model of crystal/solution interface. Adapted from[22].....12

Figure 1.6 Two dimensional model of crystal growth. Adapted from[20]. 13

Figure 1.7 The crystal growth from a screw dislocation. Adapted from[20]. 14

Figure 1.8 Morphology of a crystal depending on the growth rate of the different faces. Adapted from[20].15

Figure 1.9 Morphology of snowflake at different water supersaturation level and temperature. Adapted from[27].....17

Figure 1.10 Crystal structure of NaCl. 18

Figure 1.11 Formation of $[Na_xCl_y]^{x-y}$ aggregate in water. Sodium and chloride ions are colored blue and green. Entirely nonhydrated ions are purple. Adapted from[30].....20

Figure 1.12 The growth of crystal at NaCl(001)- water interface. Sodium and chloride ions are colored green and purple. Water molecules are represented by sticks, white for hydrogen, and red for oxygen. (a) t=0.3ps. (b) t=19.59 ps. (a) t=1200ps. (a) t=2550ps. 300K. Adapted from[28].....20

Figure 1.13 Schematic drawing for tip growth mechanism of whisker proposed by Sears. Adapted from[44]. 27

Figure 1.14 Concentration dependence of surface tension at various temperatures. Adapted from[45]. 28

Figure 1.15 Schematic drawing for base growth mechanism of whisker proposed by Shichiri. 31

Figure 1.16 Schematic drawing for base growth mechanism of whisker proposed by Amelinckx. Adapted from Amelinckx[25]. 32

Figure 2.1 Experimental set-up for whisker growth on porous coatings. Not to scale. 43

Figure 2.2 SEM images of the silica nanoparticle porous coating used as a platform for whisker growth: (a) cross section and (b) top surface. 46

Figure 2.3 Digital image of a specimen after standard whisker growth on a porous coating. Growth occurred for two days at 80% RH using a 2.9 wt% KCl solution. 48

Figure 2.4 SEM micrographs of whisker growth zone after standard growth conditions: (a) overview and (b) high magnification of a whisker base. 49
Figure 2.5 SEM micrographs of an early growth stage (1 day under standard conditions): (a) typical morphologies and (b) silica particles from porous coating on the top of a whisker. 50
Figure 2.6 Schematic drawing of the experimental setup for X-ray microdiffraction. 51
Figure 2.7 X-ray microdiffraction data gathered from a single crystal whisker. The whisker was mounted with its long axis vertical and rotated 360° around its axis during data collection. The plot was created by integrating the signal points gathered on an area detector. 52
Figure 2.8 SEM micrographs of (a) fallen whiskers that are propped up and remain in contact with the porous coating such that an extension grows. (b) the initial stage of sheet formation. Here the fallen whisker is beginning to be pushed up by base growth. (c) fallen whisker in contact with substrate that continues growth into two sheets connected by the original fallen whisker in the middle (inset figure). (d) two sheets grown from the same fallen whisker as a starting point, one sheet is lifted up by the other. The inset shows the continuity between the whisker and the sheet. 53
Figure 2.9(a) Digital images of the liquid front in the porous coating; left to right 1 min; 20 min; 1 hour after immersion into the KCl solution at 80% RH. (b) Effect of relative humidity on liquid front position for KCl solution (2.9 wt% KCl) in porous coatings, and liquid front position for water in porous coating at 80% RH. 54
Figure 2.10 Optical micrographs of the growth of whiskers on a porous silica coating with increasing growth time ($t_1 < t_2 < t_3 < t_4$ with time interval 5 s). The central whisker has a small crystal attached to its tip, making apparent the growth by extension from the base. 56
Figure 2.11 Optical micrographs of whiskers on a porous silica coating with increasing growth time ($t_1 < t_2 < t_3 < t_4 < t_5 < t_6$; total growth time = 108 s). Whiskers are labeled with numbers for easy tracking. 57
Figure 2.12 Digital images of specimens grown from solutions of varying KCl concentrations, as indicated, with all other conditions the same as the standard condition. The right end was the one immersed in the salt solution. 58
Figure 2.13 SEM micrographs of the whisker growth zone under conditions of (a) 65% relative humidity with all other conditions the same as the standard condition and (b) 60% relative humidity with all other conditions the same as the standard condition. 59
Figure 2.14 Digital images of specimens grown from solutions of varying KCl concentrations, as indicated, with all other conditions the same as the standard condition. The right end was the one immersed in the salt solution. 60

Figure 2.15 Schematic drawing of whisker and sheet growth mechanism in time sequence. ($t_1 < t_2 < t_3 < t_4 < t_5 < t_6$). t_1 whisker starts growing; t_2 whisker continues to grow; t_3 whisker tilts; t_4 whisker falls; t_5 sheet starts to grow, fed from liquid in porous coating beneath; t_6 salt sheet is formed. 69

Figure 3.1 Digital images of specimens grown on different coatings with varied thicknesses. All other conditions remained the same as the standard condition described in chapter 2. The right end was the one immersed in the salt solution. 73

Figure 3.2 Digital images of specimens grown from KCl solutions on porous coating with different particle sizes as labeled on the image. The relative humidity is also labeled and the growth time is two days for all the samples. 78

Figure 3.3 SEM images of specimens grown from KCl solutions on 200nm silica particle porous coating under standard growth condition. (KCl 2.9wt%, 80% RH) 80

Figure 3.4 SEM images of specimens grown from 2.9wt% KCl solutions on 22nm silica particle porous coating at 75% RH. 81

Figure 3.5 SEM images of specimens grown from KCl solutions on 200nm silica particle porous coating at 83%RH. 82

Figure 3.6 Schematic drawing of whisker sits on porous coating with large and small particle size. 86

Figure 3.7 Experimental setup for whisker growth at varying growth angle. above: growth angle is 60° and below: growth angle is 180°. 88

Figure 3.8 Whisker growth on porous coating with different growth angle under standard whisker growth condition. 89

Figure 3.9 SEM image of salt crystal at the base of the whisker with growth angle at 60° (a,b) and 90° (c,d). 90

Figure 3.10 Schematic drawing of meniscus at the root of the whisker. (Left) growth angle is 0° and (right) growth angle is 180° 92

Figure 3.11 Schematic drawing of torque balance when whisker tilts. 94

Figure 3.12 Plot of dependence of ratio of $\tau_{support}$ / τ_{fall} on tilt angles for a 10 µm whisker with aspect ratio of 100. 97

Figure 3.13 Schematic drawing of coated silicon wafer with liquid drop dispensed on top surface porous coating and the whiskers grown on the edge surface. 100

Figure 3.14 Cryo-SEM images of surface morphology of pure water (a) and KCl salt solution 2.9wt% (b) after freezing with liquid nitrogen. 101

Figure 3.15 Cryo-SEM images of whisker-like salt crystal growth on the porous coating of edge surface of the silicon wafer (a,b). High magnification image of a tilted whisker-like crystal base. (150 nm aggregates particle, KCl 2.9wt%, growth time: 20 mins, ~50%RH).....103
Figure 3.16 Cryo-SEM images of salt whisker growth on the porous coating of edge surface of the silicon wafer. (150 nm aggregates particle, KCl 2.9wt%, growth time: 10 mins, ~50%RH) 104
Figure 3.17 Cryo-SEM images of salt whisker growth on the porous coating of edge surface of the silicon wafer. (150 nm aggregates particle, KCl 2.9wt%, growth time: 20 mins, ~50%RH) 105
Figure 3.18 Digital image of specimen after free particle whisker growth. Growth occurred for two days at 70% relative humidity using a 0.03 g/ml KCl solution that contained 0.00025 wt% silica particles (150 nm aggregates). 111
Figure 3.19 SEM of whiskers grown on bare substrates by the free particle method. Growth occurred for two days at 70% relative humidity using a 2.9 wt% KCl solution that contained 0.00025 wt% silica particles (150 nm aggregates). 112
Figure 4.1 SEM image of whisker growth on porous coating under standard growth condition for 10 hours. (KCl 2.9wt% 80%RH) 121
Figure 4.2 Cross-section SEM image of small salt crystal formed on the surface of porous coating at initial whisker growth stage. (KCl 2.9wt%, 80%RH, 2 hours) 122
Figure 4.3 Experimental setup for whisker growth on porous coating. 123
Figure 4.4 SEM image of whiskers grown on porous coating in growth zones A (a,b) and growth zone B (c,d,e,f). (please refer to Figure 4.3) 124
Figure 4.5 Schematic drawing of porous film on patterned substrate.....126
Figure 4.6 SEM images of whisker growth on patterned substrate under standard growth condition.....127
Figure 4.7 SEM image of manually ground KCl seeds.....128
Figure 4.8 SEM image of whiskers grown on porous coating by manually ground KCl seeds under standard growth condition. 129
Figure 4.9 SEM image of attritor ground KCl seeds.....131
Figure 4.10 SEM image of whiskers grown on (a) 150nm aggregates 80%RH and (b) 22 nm particle porous coating 70% RH by seeding with attritor ground seeds. (KCl 2.9 wt% , 2 days.).....132
Figure 4.11 SEM image of whiskers grown on 150nm aggregates porous coating by seeding with agglormerate of attritor ground seeds under standard condition. 134
Figure 4.12 SEM image of whiskers grown on 22nm particle porous coating by seeding with too many attritor ground seeds. (KCl 2.9wt%, 70% RH, 2 days.) 136

Figure 4.13 SEM image of whiskers grown on 22nm particle porous coating by seeding with proper amount of attritor ground seeds. The growth condition are KCl 2.9wt%, 75%RH, 2 days. 138
Figure 4.14 SEM image of tapered whisker grown on porous coating under standard growth condition. 139
Figure 4.15 SEM image of filtered attritor ground KCl seeds with 200nm filter. 140
Figure 4.16 SEM image of whiskers grown on 22nm particle porous coating by seeding with 200nm filtered seeds. The growth condition are KCl 2.9wt%, 75%RH, 2 days. 141
Figure 4.17 SEM images of NaCl (a) and KBr (b) whiskers grown on porous coating. (NaCl: NaCl 2.9wt%, 70%RH, 2 days. KBr: KBr 2.9wt%, 67%RH, 2 days) 144
Figure 5.1 SEM image of a fractured 30PPI carbon foam. 148
Figure 5.2 The setup for dip coating, including a computer controlled stage and a dynamic weight monitoring system. 150
Figure 5.3 Schematic cross-section (top) and photograph (bottom) of the adaptor used to hold the foam on the Headway Research spin coater during spin treatment. 152
Figure 5.4 Weight of a 10 PPI carbon foam, relative to its dry weight, measured as it was immersed at 1 mm/s and withdrawn at 0.25 mm/s from a 90 wt% glycerol/10% water solution. Path ABCDEFGHI is the initial data taken with dry foam, and path A'B'C'D'E'F'G'H'I' is the data for a second cycle of immersion and withdrawal. (top). A schematic drawing of foam position relative to liquid level. (bottom).....156
Figure 5.5 Effect of withdrawal speed on the average coating thickness from dip coating of glycerol/water solutions onto 10PPI carbon foam. Data are labeled with the wt% glycerol in the solution. 159
Figure 5.6 Effect of viscosity (in cP) on the average coating thickness from dip coating glycerol/water solutions onto 10 PPI carbon foam. Data are labeled with the withdrawal speed. The slope shown is the results from linear least squares fitting. 160
Figure 5.7 Effect of surface tension effect on the average thickness from dip coating of 70% glycerol/30% water solution of various surface tensions onto 30PPI carbon foam. Data are labeled with the surface tension of the solution. 161
Figure 5.8 Effect of withdrawal speed on the average coating thickness from dip coating of glycerol/water solutions onto 10 PPI and 30 PPI carbon foam. Data are labeled with the % glycerol in the solution and the pore content of the foam. 163
Figure 5.9 Optical images of Excess liquid trapped in the pores of carbon foam (left). A solidified film formed on the pore window (right). 164

Figure 5.10 Effect of initial liquid load on final coating thickness for 30 PPI carbon foam dip coated with 90% glycerol 10% water at various withdrawal speeds and spin treated at speed of 1500 rpm for 30 seconds. 165
Figure 5.11 Effect of spin time on coating thickness for 30 PPI carbon foam dip coated with 100% glycerol (above) and 80%glycerol 20%water (below) and spin treated at speeds from 1000 rpm to 3000 rpm with each increment of 250 rpm. 166
Figure 5.12 Effect of spin speed and solution composition on the coating thickness from spinning 30PPI carbon foams. Data are label with the % glycerol. The spin time is 120 seconds and the slope shown is determined by linear least squares fitting. 168
Figure 5.13 Effect of spin speed on the average coating thickness for spin coating of 80% glycerol/20% water solution onto 10, 20 and 30 PPI carbon foams. The spinning time was 120 s. 169
Figure 5.14 Optical micrographs (left) and SEM top view and cross section (right) of alumina coating onto carbon foam with spin treatment. (2000 rpm; 30 secs) 170
Figure 5.15 SEM micrographs of alumina coatings using three depositions and calcinations on 30 PPI carbon foam: variation in coating thickness near the edge of a strut (left) and coating thickness at the center of the strut (right). 172
Figure 5.16 SEM micrographs of the exfoliated MCM-22 zeolite coating on the alumina foam. Low magnification (left) and high magnification (right). 173

Chapter 1 Background and Overview

1.1 History of Whiskers

Any fibrous growth of a solid may be regarded as a form of whisker growth.[1] However, whiskers are normally considered more or less perfect single crystals with a minimum length to diameter ratio of 5 and a diameter ranging from 2 μm to 100 μm.[2, 3]

Whisker history dates back to 1574. Ercker[1] reported that by cutting or scratching a silver ore decorative figure and holding it on the charcoal fire until it got hot, hair like silver would sprout out from the cut or scratch. Also, numerous minerals, such as asbestos, chrysotile, millerite and chalcotrichite, have been found in fibrous form. Over the years, numerous references to these fibrous crystals have appeared in the literature. However, due to limit knowledge of the crystalline state, no significant progress in understanding these fibrous structures was made until 20th century.

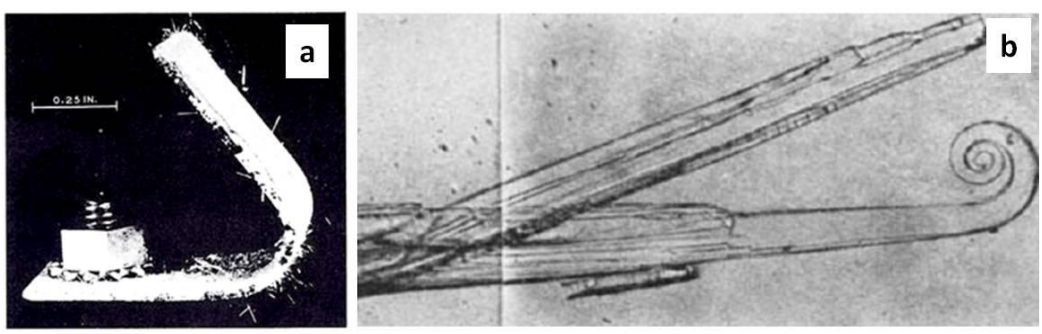

Figure 1.1 (a) Early photograph of spontaneously growing tin whiskers from Bell Laboratories investigation of electrical short circuit failures from tin plated details in telephone switching equipment in the 1940's.Adapted from[4](b) an optical images of sodium chloride whisker grown. Adapted from[5].

In 1945, successive failures in electronic equipment were attributed to microscopic conducting fibrous crystals sprouting from electroplated surface of zinc, cadmium and tin.[6] An early image of tin whisker is shown in Figure 1.1a. At that time, scientists focused their researches on how to prevent these fibrous crystals from growing. Since then the fibrous crystal became to be known as "whiskers". In 1952, a tin whisker about two micrometer in diameter was found to be able to be elastically bent to strains of more than two percent while bulk tin began to flow at strains of less than 10^{-4}.[3] The superior elastic strength aroused much interest and extensive researches were carried out on whiskers from 1950's to 1970's and one example of sodium chloride whisker is shown in Figure 1.1b. Copious studies [2, 3, 7-14] showed the mechanical strength of some whiskers approached the theoretical limit. Herring[15] suggested that the whiskers are strong because they are free of dislocations or few dislocations were present inside. Some properties of whiskers, which are related to specific materials were also widely investigated. For example, Deblois[1] reported experimentally obtained coercive force of 483 Oe for an iron whisker, which is within 15 percent of the theoretically predicted value for an ideal specimen of iron at 25°C. Masanori[16] grew $(Y_{0.86}Ca_{0.14})Ba_2Cu_3O_x$ whisker showing superconducting property with a critical temperature of 83K and a critical current density of 4.4×10^4 A/cm.[2]

Many methods of growing whiskers have been developed. These methods include direct growth of whiskers from the solid phase or melts, vapor phase growth of whisker by condensation of supersaturated vapor, whisker precipitation directly in supersaturated solution, and whisker growth from solution via porous media.

1.2 Fundamental Theory of Crystal Growth

Crystallization is fundamental to whisker growth, and a brief review of crystal growth is provided in this section.

Supersaturation. The constituents of liquid solutions are solutes and solvents. Solubility refers to the ability for a given substance, the solute, to dissolve in a solvent.[17] It is often defined as the maximum amount of solute that can be dissolved in a solution at equilibrium. The resulting solution is called a saturated solution. The solubility of solute in a given solvent is related to the temperature. For around 95% of solid solutes, the solubility increases with rising temperature. However, the solubility for gaseous solute is generally inversely proportional to the temperature.[18]

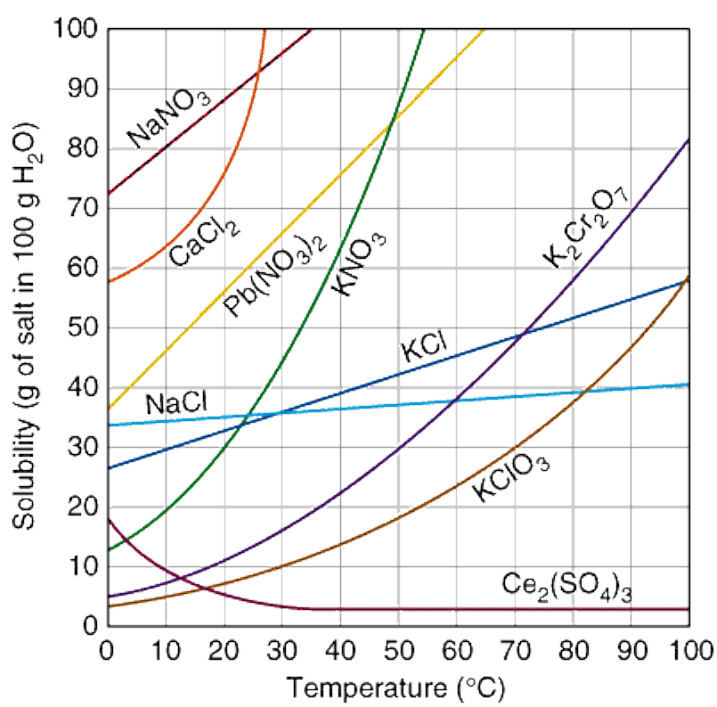

Figure 1.2 Solubility dependence of various salts on temperature. Adapted from[18].

Figure 1.2 shows the effect of temperature on solubility of various salts in water. Many salts such as $CaCl_2$ and $NaNO_3$ display a large increase of solubility with temperature. Some solutes like NaCl have solubility relatively independent of temperature. Solubility of a few salts such as $Ce_2(SO_4)_3$ decreases at higher temperature.

If a hot concentrated solution is slowly cooled down without agitation, a state of supersaturation can be attained. Supersaturation refers to a state in which the solvent contains more dissolved solute than can ordinarily be accommodated at that temperature.[20] Such a solution is said to be supersaturated. Generally speaking, supersaturation is a necessary condition for crystallization to begin. Figure 1.3 shows the effects of concentration and temperature on solution state. The continuous line defines the saturation curve. The upper broken curve indicates a spontaneous crystallization state. These two lines divide the diagram into three regions:[20] (1) the undersaturation region below the saturation curve, where crystallization does not happen; (2) the metastable region between the two lines, where spontaneous crystallization is also not possible unless nuclei or crystal seed exists in the solution; (3) the unstable region, where spontaneous crystallization is possible.

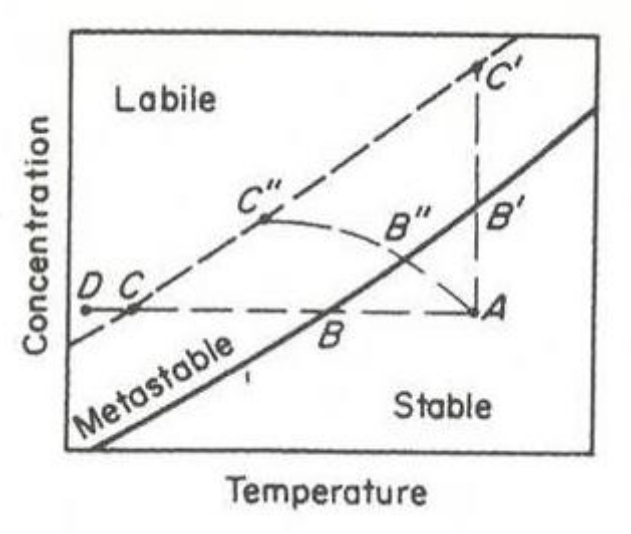

Figure 1.3 The concentration-temperature diagram. Adapted from[20].

There are several methods to reach supersaturation, including cooling, solvent evaporation, drowning and chemical reaction. Cooling method is shown as line ABCD in Figure 1.3. If temperature decreases from point A, saturation concentration is reached at Point B. With further cooling, supersaturation continues to increase till point C. During cooling, the system is in a supersaturated state; However, as in the metastable region, crystallization will not happen spontaneously. If cooling continues, D point will be reached and spontaneous crystallization will occur.[20, 21]

Solvent evaporation is another way to achieve supersaturation, which could be illustrated by line AB'C' in Figure 1.3. As solvent evaporate, solution concentration rises from Point A to C'. Because evaporation takes place at the surface, limited by solute diffusion, the concentration at the surface is larger than that in the bulk. Crystals will first form on the surface and then fall by gravity into the bulk solution as seed or nuclei to promote further crystallization.[20, 21] The supersaturation of a solution may be expressed in

a number of different ways. One of the most common expressions is the fundamental supersaturaton ratio S, which is defined by [20]

$$S = \frac{a}{a^*} \qquad 1.1$$

where a is the activity of a supersaturated solution, and a* is the activity of the saturated solution.

The thermodynamic driving force for crystallization is the difference between the chemical potential of the solute in the solution(state 1) and the solute in the crystal (state 2), $\Delta\mu$

$$\Delta\mu = \mu_1 - \mu_2 \qquad 1.2$$

In order to crystallize $\Delta\mu$ should be greater than zero. The chemical potential, μ, is defined in terms of the standard potential, μ_0 and the activity, a, by

$$\mu = \mu_0 + RT \ln a \qquad 1.3$$

where R is the gas constant and T is the absolute temperature. Therefore,

$$\mu_1 = \mu_0 + RT \ln a \qquad 1.4$$

As saturated solution is in a equilibrium state, the chemical potential of solute in solution is equal to the chemical potential of solute in solid phase, so

$$\mu_2 = \mu_0 + RT \ln a^* \qquad 1.5$$

Then $\Delta\mu$ can then be expressed as: [20]

$$\Delta\mu = RT\ln\left(\frac{a}{a*}\right) = RT\ln S \qquad 1.6$$

Hence

$$S = \exp\left(\frac{\Delta\mu}{RT}\right) \qquad 1.7$$

Nucleation. Supersaturation alone is not sufficient for a system to start crystallization. A number of minute solid particles, such as nuclei or seeds, are necessary to exist in the solution, and these tiny particles can then act as the centers for crystallization to occur. The formation of these particles is considered as nucleation. Generally, the nucleation can be divided into two types: primary and secondary nucleation. The primary nucleation refers to the case that there is no crystalline particle in the system. It includes homogeneous nucleation and heterogeneous nucleation. On the other hand, secondary nucleation occurs if crystal nuclei or seeds exist in the supersaturated solution.[20]

Homogeneous nucleation. It is difficult to describe the formation of crystal nuclei. This results from not only the agglomeration of solute molecules, but also from the arrangement of these molecules into a certain periodic crystal structure. The number of molecules in a stable crystal nucleus can vary from a few to several thousand. For example, 100 molecules are needed for ice nuclei. The stable nuclei could be formed by a serials addition of solute molecules. Further addition of molecules results in nucleation and subsequent growth of the nucleus. The structure of a critical nucleus is too small to

be observed directly and remains unknown. It could be a tiny perfect crystal or a rather diffuse body of molecules or ions loosed bounded to each other.[20, 21]

The classical theory of nucleation is based on the thermodynamic model. The overall excess free energy, ΔG, for a nucleus is equal to the sum of the excess free energy between the surface of the particle and the bulk of the particle, ΔG_s, and the volume excess free energy, ΔG_v, (the excess free energy between a crystal particle and the solute in solution). It could be expressed as, [20, 21]

$$\Delta G = \Delta G_V + \Delta G_s = \frac{4}{3}\pi r^3 \Delta G_v + 4\pi r^2 \gamma \qquad 1.8$$

where γ is the interfacial energy between solvent and crystal.

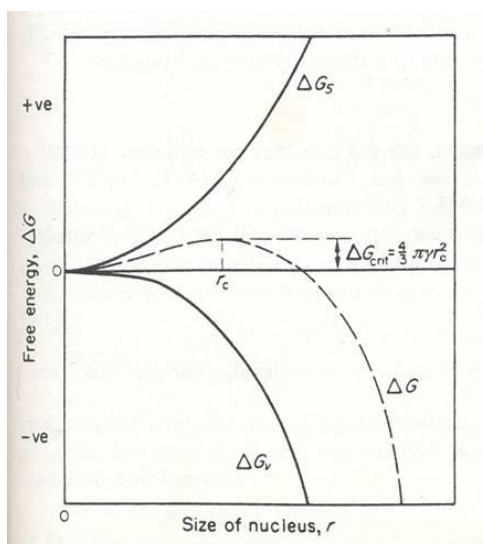

Figure 1.4 Free energy diagram for nucleation explaining the existence of a critical nucleus. Adapted from[20].

The volume excess free energy, ΔG_V, has a negative value while surface excess free energy ΔG_s is positive. These two energy terms depend differently on the nucleus radius. So the free energy of formation, ΔG, may reach a maximum point as shown in Fig.2.3. This maximum energy value defines the critical energy, ΔG_c, and the radius of nuclei corresponding to this maximum energy is the critical nucleus radius r_c. For a spherical particle, ΔG_c and r_c could be obtained by maximizing eqn.1.8. [20, 21]

$$\frac{d\Delta G}{dr} = 4\pi r^2 \Delta G_v + 8\pi r\gamma = 0 \qquad 1.9$$

therefore,

$$r_c = \frac{-2\gamma}{\Delta G_v} \qquad 1.10$$

from eqn1.8 and eqn1.10,

$$\Delta G_{Crit} = \frac{16\pi\gamma^3}{3(\Delta G_v)^2} = \frac{4\pi r_c^{\,2}\gamma}{3} \qquad 1.11$$

The critical size r_c determines the minimum size of a stable nucleus. Particles with radius smaller than r_c will redissolve and if the particle size is larger than r_c, it will continue to grow.

The rate of nucleation J (the number of nuclei formed per unit time per unit volume) could be expressed in the form of the Arrhenius reaction velocity equation commonly used for the rate of thermally activated process, [20]

$$J = A\exp\left[\frac{-\Delta G}{kT}\right] \qquad 1.12$$

where k is the Boltzmann constant and T is absolute temperature. By combining eqn1.1, eqn1.11 and eqn1.12 with the Gibbs-Thomson relationship:

$$\ln S = \frac{2\gamma\nu}{kTr} \qquad 1.13$$

where ν is the molecular volume. The nucleation rate could be written as

$$J = A\exp(-\frac{16\pi\gamma^3\nu^2}{3k^3T^3(\ln S)^2}) \qquad 1.14$$

This equation suggests the rate of nucleation is governed by temperature, T; degree of supersaturation, S; and interfacial tension γ. The critical supersaturation could be found if the nucleation rate is chosen. If the J is selected to be one nucleus per second per unit volume, then eqn1.14 becomes[20]

$$\ln S_{crit} = (\frac{16\pi\gamma^3\nu^2}{3k^3T^3\ln A^2})^{1/2} \qquad 1.15$$

Heterogeneous nucleation. The nucleation rate of a solution can be affected greatly by the presence of impurities in the system. In this case, the interfacial energy of liquid-substrate interface, γ_{LS}, the crystal-substrate interface energy, γ_{CS} and the liquid-crystal interface energy, γ_{LC} should be considered. The critical free energy for heterogeneous nucleation could be expressed as[20]

$$\Delta G'_{Crit} = \frac{16\pi\gamma^3}{3(\Delta G_v)^2}\left(\frac{(2+\cos\theta)(1-\cos\theta)^2}{4}\right) \quad 1.16$$

where θ is the contact angle between the crystalline deposit and the foreign solid surface, which corresponds to the angle of wetting in liquid-solid systems. It obeys Young's equation

$$\cos\theta = \frac{\gamma_{LS} - \gamma_{CS}}{\gamma_{LC}} \quad 1.17$$

Generally speaking, heterogeneous nucleation is more energetically favorable as the critical free energy needed for heterogeneous nucleation is less than that for homogeneous nucleation. Most crystallization processes start by heterogeneous nucleation due to the inevitable presence of impurities in the solution. For example, aqueous solutions normally prepared in the laboratory may contain>10^6 solid particles per cm^3. Filtration operation can lessen the impurity particles to <10^3 per cm^3, but a solution free of foreign particles is generally not possible to make.[20]

Crystal growth. After nuclei have been formed in a supersaturated solution, they start to grow into larger crystals. When solute molecules or ions reach the surface of crystal, a less organized adsorption layer will first be formed. The loosely bounded molecules or ions in the adsorption layer will then be integrated into the crystal lattice. Thus crystal growth is generally divided into three stages: diffusion, adsorption and integration. Because the growing crystal consumes the solute in the surrounding area of the crystal, a concentration gradient appears and drives diffusion of solute from the bulk solution to the crystal.[20, 22]

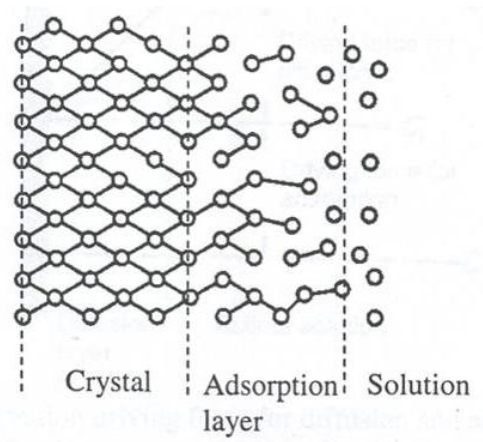

Figure 1.5 A model of crystal/solution interface. Adapted from [22].

The driving forces for diffusion, adsorption and integration are different. There are two steps in the mass deposition as shown in Figure 1.5. First the solute molecules are transported from the bulk of the fluid phase to the surface of adsorption layer, which could be expressed by Eqn.1.18[20]

$$\frac{dm}{dt} = k_d A(c - c_i) \qquad 1.18$$

where k_d is mass diffusion coefficient; c is the concentration in bulk solution and c_i is the solute concentration in the adsorption layer-solution interface.

Second, the solute molecules arrange themselves into the crystal lattice by a first order reaction. This can be represented by Eqn.1.19.

$$\frac{dm}{dt} = k_r A(c_i - c^*) \qquad 1.19$$

where K_r is a rate constant for the surface reaction (integration) process, and c^* is the solute concentration in the absorption layer-crystal interface.

Equation1.18 and 1.19 are not easy to apply to real experiment because interfacial concentration is difficult to measure. By eliminating c_i, an equation for crystallization based on the overall driving force can be written as [20]

$$\frac{dm}{dt} = k_G A(c - c^*) \qquad 1.20$$

where K_G is an overall crystal growth coefficient.

For integration stage, the solute molecules or ions are most easily bonded to the imperfection site, e.g. step or kink. The Figure 1.6 illustrates a two dimensional model of a step on the crystal surface. The solute molecule preferentially bonds to the site A, which provides a higher coordination number, and greater stability relative to integration onto the flat surface. As a result, the step advances over the entire surface and a new surface is generated.

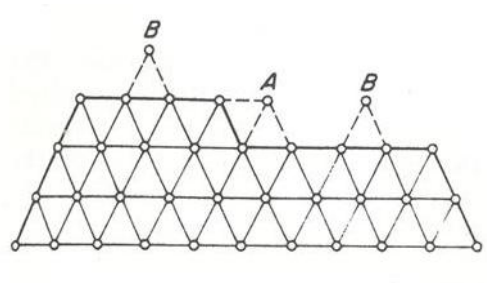

Figure 1.6 Two dimensional model of crystal growth. Adapted from[20].

Generally, for crystal growth to occur continuously, a fresh step must be created on the completed crystal surface. Volmer suggested that, as reviewed by Mullin[20], a monolayer island nucleus was created on a singular crystal surface, so that the other

solute ions or molecules can easily incorporate into the crystal at the step formed by this nucleus. This theory is called surface nucleation or two dimensional nucleation mechanism.[20]

However, experiments indicate that many crystals grow at a much faster rate than the rate predicted by two dimensional nucleation mechanisms. Frank[23] first proposed a spiral growth mechanism in 1949 to explain the crystal growth at low supersaturation with high growth rate. In this theory, once a screw dislocation with a Burgers vector perpendicular to the crystal surface has been formed, it will provide a continuous source of steps as shown in Figure 1.7.[20] Therefore, this screw dislocation avoids the necessity for nucleation on flat surface. The presence of a screw dislocation appears in one mechanism suggested for whisker growth.[24, 25]

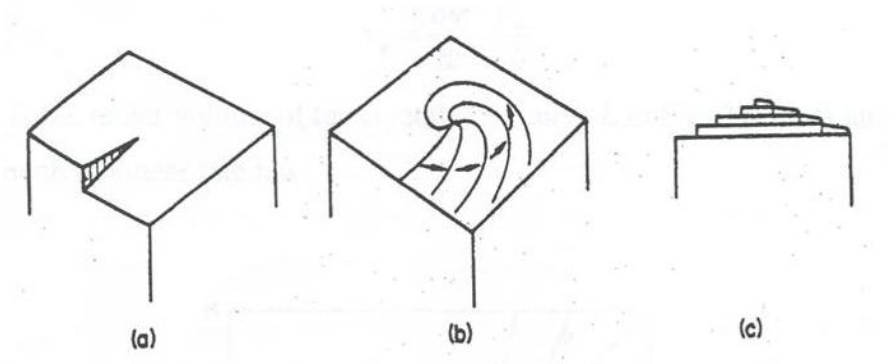

Figure 1.7 The crystal growth from a screw dislocation. Adapted from[20].

Crystal habit. The external appearance of the crystals is referred to as crystal habit or crystal morphology.[20] The morphology of a crystal depends on the growth rates

of the different crystallographic faces. Some faces (Face B in Figure 1.8) grow very fast and will disappear during crystal growth. They have little influence on the crystal habit. The slow-growing faces(Face A in Figure 1.8) have great effect on crystal habit.

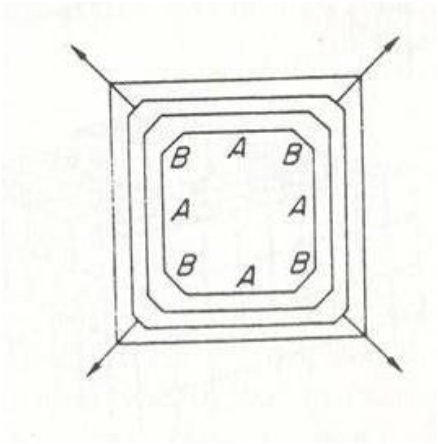

Figure 1.8 Morphology of a crystal depending on the growth rate of the different faces. Adapted from[20].

The growth of a given face is governed by the crystal structure, defects, and the environmental conditions. For instance, Davey[26] studied the growth of succinic acid crystal from water and isopropanol solutions. The succinic acid crystal platelets grown in aqueous solution changed to crystal needles if grown in isopropanol solution. Davey[26] stated that the water molecule adsorption on (001) face would slow down the growth rate on (001) surface, which resulted in the platelet shape. However, if grown from isopropanol solution, the adsorption of isopropanol molecules had stronger interaction with both (010) and (001) faces, which blocked the further growth on these two faces, crystal needles were hence formed.

Besides solvent, certain kinds of impurity or poison can be added to the solution to change the crystal habit. This is mainly owing to a special interaction between the active impurities with specific faces of the crystal. Such interaction induced preferential adsorption of impurity on particular crystal face will block or reduce further crystal growth on this face and finally changes the crystal morphology. For example, the equilibrium shapes of NaCl crystals are commonly cube enclosed by {100} faces. However, if polyvinyl alcohol is added to the NaCl solution, one dimensional growth of NaCl is achieved and NaCl whisker can be obtained.

The habits of crystals can also be influenced by temperature and supersaturation. This also occurs in daily life, especially in Minnesota. Snowflakes are generally considered to have only one crystal form; however, there are many kinds of snowflakes observed by Kenneth.[27] Figure 1.9 shows different morphology of snowflakes grown at different temperature and supersaturation. It illustrates that at -2°C, thin plated and stars grow. Columns and slender needles appear near -5°C. Plates and stars form again at around -15°C. Furthermore, the supersaturation of water also affects the structure of snow. At low humidity (saturation), simpler shapes form. While humidity increases, complex shapes are observed as shown in Figure 1.9. Two extreme shapes will form at -5°C(long needles) and 15°C(thin plates) if the humidity is especially high.

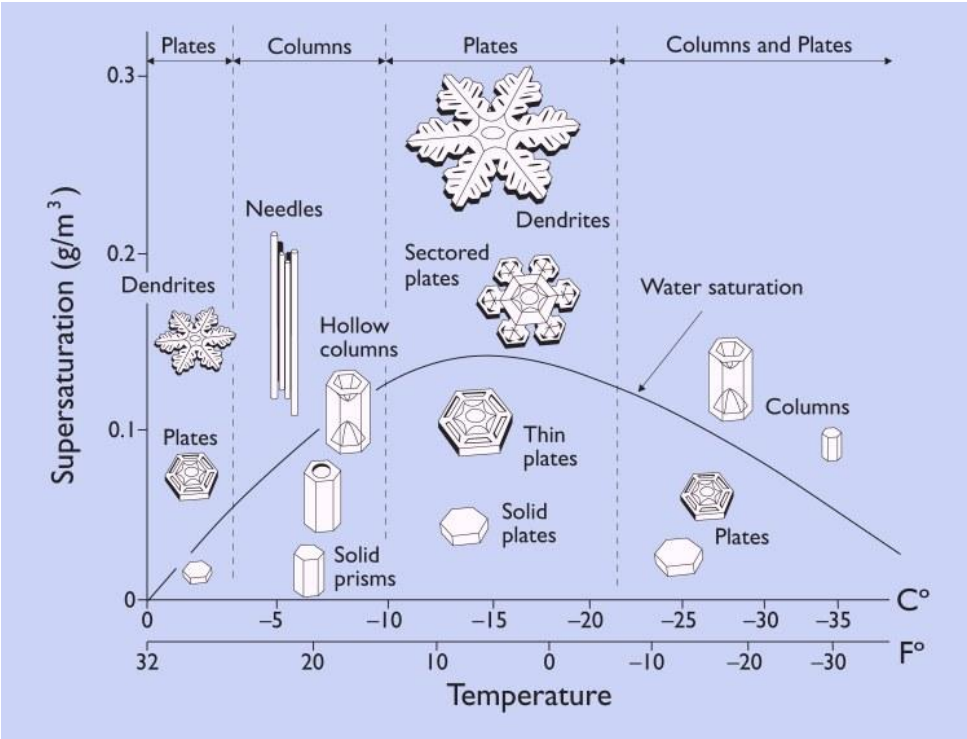

Figure 1.9 Morphology of snowflake at different water supersaturation level and temperature. Adapted from[27].

1.3 NaCl Crystal Nucleation and Growth on Atomic Level

In our experiment, materials such as KCl, KBr and NaCl are used for whisker growth. These salts belong to NaCl (rocksalt) crystal structure. A brief introduction of NaCl crystal nucleation and growth based on computational simulation is illustrated in this section.

In NaCl (rocksalt) structure, two kinds of ions are arranged in a cubic closed-packing. Each ion is surrounded by six ions with the opposite sign as shown in Figure 1.10.

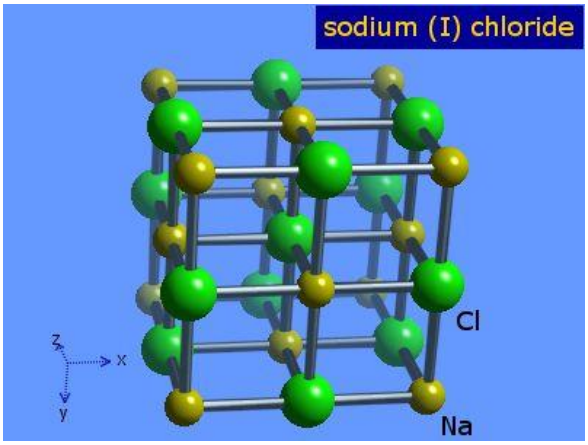

Figure 1.10 Crystal structure of NaCl.

The classic theory of crystal nucleation and growth mentioned in previous sections provides a general idea of how a crystal is nucleated and formed. However, limited to characterization techniques, in-situ observation of nuclei formation and crystal growth at the atomic level is impossible. Recently, extensive studies have been carried

out on the nucleation and crystal growth process and dynamics based on computer simulation. As NaCl is one of the simplest ionic crystals, many groups[28-31] have investigated the spontaneous nucleation and crystal growth of NaCl in aqueous solution. Yang[28] adopted molecular dynamic simulation method to obtain the critical nucleus size for NaCl. They counted the total numbers of the nuclei created and decayed within 1.2 ns simulation time to determine the critical size. The detailed data is shown in Table 1.1. The decay is defined as the process that atom detached from the nucleus during the simulation time. The data in Table 1.1 demonstrated that the probability of decay for one-atom was larger than 0.5, and such nucleus was considered as unstable. While for the nucleus composed of more than two atoms, the probability of decay was less than 0.5, and two atom nucleus in this case was regarded as the critical nucleus. If the supersaturation was reduced to 24% compared to 43% in the previous case, the critical size of the nucleus was found to be three atoms.

Table 1.1 Statistics on the sum of created and decayed nuclei during the 1.2ns MD simulations with 43% supersaturation at 298K. Table adapted from[28].

	One-atom Na^+	One-atom Cl^-	Two atom	Three atom
$Number_{total}$	138	110	90	69
$Number_{decay}$	74	77	40	23
$Percentage_{decay}$	0.54	0.7	0.44	0.33

Zahn[30] also investigated nucleation of NaCl from aqueous solution. Several kinds of $[Na_xCl_y]_{x-y}$ aggregates formed in a 150 ps trajectory from path sampling method was observed as is shown in Figure 1.11. Zahn found that at early stage of nucleation, the nucleus with a Cl ion in the center was not stable. Only sodium ions could act as centers of stability of the aggregates and was coordinated octahedrally by chloride ions.

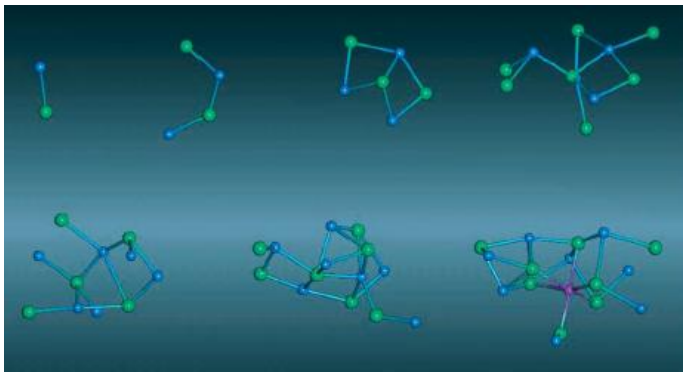

Figure 1.11 Formation of $[Na_xCl_y]^{x-y}$ aggregate in water. Sodium and chloride ions are colored blue and green. Entirely nonhydrated ions are purple. Adapted from[30].

Yang[28] also studied the crystal growth of NaCl on (001) face of bulk NaCl crystal in aqueous solution by molecular dynamic simulation as shown in Figure 1.12.

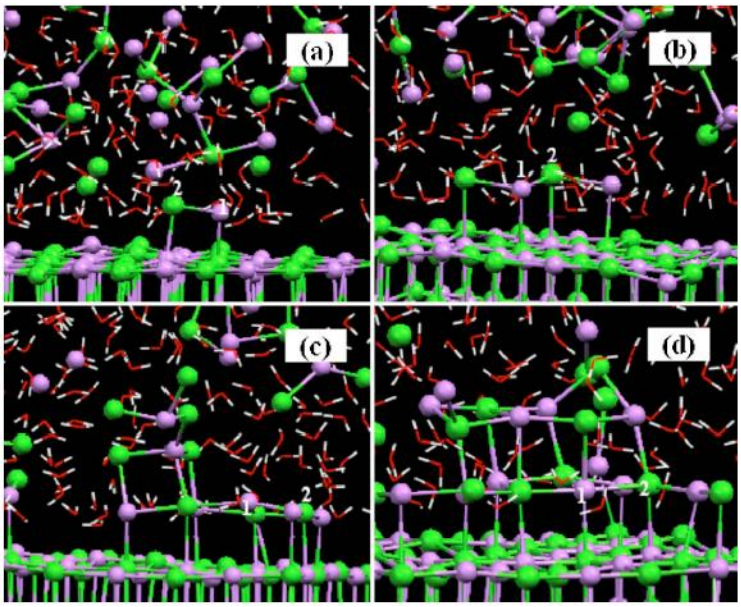

Figure 1.12 The growth of crystal at NaCl(001)- water interface. Sodium and chloride ions are colored green and purple. Water molecules are represented by sticks, white for hydrogen, and red for oxygen. (a) t=0.3ps. (b) t=19.59 ps. (a) t=1200ps. (a) t=2550ps. 300K. Adapted from[28].

Na^+ ions was found to obtain a higher deposition rate than the Cl^- ions, which led to a larger number of Na^+ ions on the (001) surface. This suggested that the water-NaCl(001) interface is positively charged. The accumulation of the positive charge from Na^+ will then attract the Cl^- ions to deposit onto the crystal surface. Yang proposed that in addition to the chemical potential difference in classic crystal growth theory, this columbic force would also serve as the driving force for the NaCl crystal growth.

Further investigation was carried out to find out the reason for higher deposition rate of Na^+. The results revealed that the different deposition rate of Na^+ and Cl^- ions originated from a relative stable water network existing at the liquid-solid(NaCl) interface. When a Na^+ approached the NaCl(001) surface, it would substitute the water molecules atop the Cl^- ion at the water-NaCl(001) interface because of the columbic interaction between Na^+ and Cl^- ions. For Cl^- ion adsorbing to the NaCl(001) surface, it replaced the water molecules atop the Na^+ ion. The water molecule atop Cl^- was bounded to Cl^- ion by H-Cl^- hydrogen bonding while O-Na^+ interaction stabilized the water molecules on the Na^+ ion. From ab initio calculation for water monomer on NaCl(001), Yang[28] discovered that the adsorption energy for water on Cl^- and Na^+ was 0.174eV and 0.401eV respectively. This 2.3 times energy difference resulted in a more energetically stable position atop the Na+ for water molecule. Thus the Na+ ions in the supersaturated solution had a better chance to deposit on the NaCl(001) surface and obtain a larger deposition rate. However, due to computer hardware, the number of ions in the simulation box and the time scale are limited. Further investigations are necessary to provide more insight into the crystal nucleation and growth.

1.4 History of Whisker Growth on Porous Media

The earliest accounts of the formation of whisker-like salt crystals on the surfaces of porous materials saturated with salt solution date back to the late 1800's, as reviewed by Nabbaro and Jackson.[1,11]

In 1817 Hoffmann found sodium chloride whiskers formed on the clay. Schmidt[32] studied the growth of sodium chloride whiskers on porous substrate and found the whiskers could be 5-6 cm long and 4 mm wide in 1911. Later, more systematic researches were carried out on this topic.

Various types of porous media have been used to grow whiskers. The typical ones includes: (a) Bulk porous material such as porous glass and porcelain; (b) Film type porous media such as cellulose acetate membranes; (c) Particle formed porous media such as silica particle gel. A brief overview of whisker growth on porous media is summarized in Table 1.2.

Table 1.2 Whiskers growth on various porous substrate. Adapted from[33].

Porous materials	Crystal needles and whiskers
Porcelain [9-11, 34, 35] and porous glass.[36]	**KCl, NaCl, NaNO3, and KMnO4, et al.**
Cellulose acetate membranes[11, 37-41]	**KCl, NaCl, KH_2PO_4, $NaNO_2$,CH_3COONa, $NaKC_4H_4O_6$ tri-glycine sulfate and Rochelle salt, and L- alanine, et al.**
Silicic acid gel and silica gel [12, 13, 42, 43]	**KCl, NaCl, NaBr, NaI and urea**

Whisker growth on bulk porous material. Bulk porous materials were used based on their similar structure as clay, from which NaCl whisker was first observed in the nature. Porcelain was the choice of many research groups.[9-11, 34, 35]. Usually, a piece of porcelain was placed in a concentrated or saturated solution of alkali halide for several hours. The piece was then placed in the room or in a dessicator filled with certain saturated salt solution for several days, and salt whiskers would grow on the surface of porcelain. Reported orientations of the NaCl and KCl whiskers were inconsistent. [110] or [100] were reported to be the orientation of axis of whisker. Charsley[9] found that nineteen of the whiskers in his study were oriented in the [100] direction and the remaining one had [110] direction as an axis. Powell[11] claimed 100% of ten whiskers grown oriented in [100].

Shichiri[34] found two kinds of whiskers, one was straight with a regular shape, and the other one had an irregular form. By detaching the whiskers from porcelain and putting them into 15% supersaturated salt solution, no further growth in axial or lateral direction was observed for the straight whisker while lengthening and thickening occurred to the irregular whisker. Shichiri claimed that the straight whisker was free of dislocation, but imperfections existed in the irregular whisker. Dissimilar morphology of the whiskers was then related to different whisker growth mechanisms and will be discussed in details later.

Yellin[36] used porous glass to grow whisker, unlike porcelain, the glass disc was half-submerged in the salt solution to ensure continuous salt supply. Yellin observed that no whisker penetrated the glass disc and the whisker stemmed from the crater rather than

from the internal pore structure and he concluded that the habit modification was a result of the surface structure of the exposed porous glass and the open porous internal structure served only as channels for transporting liquid from the solution reservoir to the exposed surface.

Whisker growth on porous film. Cellulose-acetate(CA) membrane was known for its use in ultra-filtration and desalination by reverse osmosis process. With CA membrane, Yellin[37] grew whiskers of a large number of soluble inorganic salts with different structures and properties. CA membrane was formed in the shape of a bag and was filled with concentrated salt solution. Centimeter long whiskers could be found on the external surface of the membrane. Because typical dimensions of cross section of whiskers were several micrometers, similar in size to the pore diameter of the support matrix, Yellin concluded that the pore structure modified the crystal morphology. However, Yellin[36] also used porous glass to grow whisker. The pore size of the glass was only 4nm and the whisker diameter is more than 500nm. In addition, there was no whisker penetrating the porous glass. The experiment result indicated the pore size was not the habit modifier, and the morphology of the whisker was related to the exposed glass surface. Regular and irregular whiskers were obtained by CA membrane method;[38] however no further experiment was done to check whether imperfection was present in the whisker.

Whisker growth on silica gel. Silica gel was a little different from the above two porous materials. Gel is soft and tends to contract during drying. Usually, whisker would not grow until the surface of the gel started to dry. Fell[12] believed the whiskers

extruded from the pores due to the contraction of gel. Wu[33] grew KCl whiskers from gel and found that most of the whiskers were in irregular shapes and had large bases. He stated that whiskers were not extruded through rigid die by hydrostatic pressure produced by the shrinkage of the gel, because the base of a whisker could not grow bigger than the extension if this theory was correct.

1.5 Background of Whisker Growth Mechanism.

1.5.1 Tip Growth Mechanism from Sears

In1955, Kato[7] grew $NaClO_3$ whisker from aqueous solution on a $NaClO_3$ single crystal and he claimed that the whisker was grown from the tip. However, no whisker growth mechanism was reported. Based on their experimental results, in 1957, Sears[39] proposed a growth mechanism for fibrous $NaClO_3$ growth based on the whisker growth mechanism from vapor deposition. The main idea of this tip growth mechanism was that the whisker contained a single screw dislocation with its Burgers vector parallel to the whisker axis. The screw dislocation induced steps on the tip surface assisted the whisker growth. An adherent liquid film from base to tip of the whisker provided Na^+ and ClO_3^- ions for continuous whisker growth. Water evaporated from the adherent film at the whisker tip more rapidly than at the whisker base, which resulted in a gradient in solute concentration. This concentration gradient then caused a gradient in surface tension, and the surface tension gradient served as the driving force for liquid film flow. It was postulated that the wall of whisker was smooth, so that whisker thickening could occur only by two-dimensional nucleation at high supersaturations, while tip growth could happen by the screw dislocation assisted growth mechanism at relatively low supersaturation. A schematic drawing was shown in Figure 1.13.

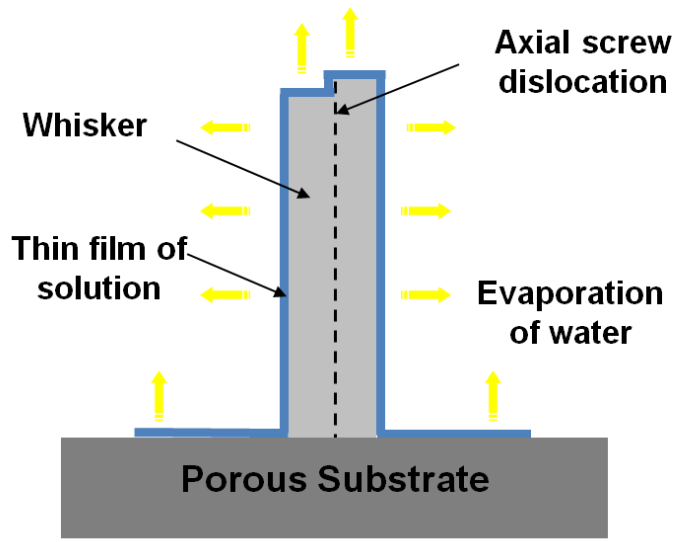

Figure 1.13 Schematic drawing for tip growth mechanism of whisker proposed by Sears. Adapted from[39].

Surface tension gradient flow is the key to the whisker growth mechanism suggested by Sears and a brief summary of this phenomenon is stated below. The surface tension gradient could be induced by temperature or by concentration. In our case, surface tension driven flow is induced by the concentration gradient. The surface tension of a binary solution could be expressed as

$$\gamma = \gamma_1 N_1 + \gamma_2 N_2 - \beta N_1 N_2 \qquad 1.21$$

where γ is the surface tension of the solution; γ_1, γ_2 is the surface tension of component1 and component 2 respectively; N_1, N_2 is the mole fraction of component1 and 2 and β is semiempirical constant.

In case of aqueous solution, simple electrolytes such as sodium chloride would increase the surface tension of the solution from that of the pure water.[40] For example,

Figure 1.14 shows the concentration dependence of surface tension for KCl aqueous solution. It shows that surface tension increases with KCl concentration at various temperatures. For a liquid, The presence of a gradient in surface tension causes the liquid to flow away from regions of low surface tension to high surface tension.

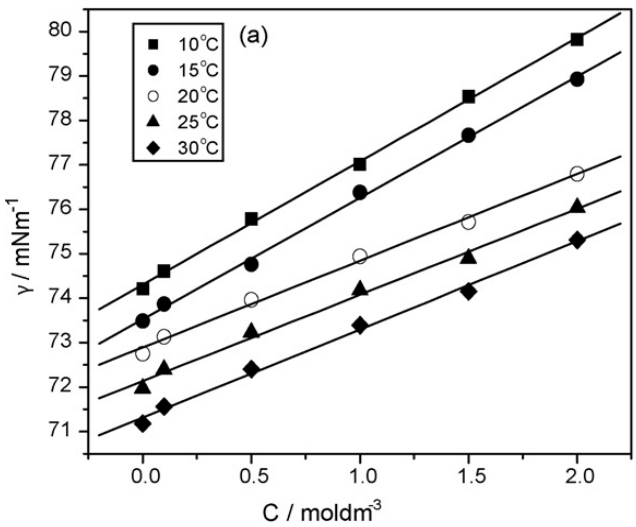

Figure 1.14 Concentration dependence of surface tension at various temperatures. Adapted from[40].

Based on Sears' model, theoretical calculation could be carried out for the surface tension gradient induced surface tension flow. The driving force for liquid flow could be expressed as[39],

$$F_{driving} = \frac{2\pi r}{M}(C_0 - C_1)\frac{d\gamma}{dC} \qquad 1.22$$

where C_0 is the solution concentration on the whisker tip; C_1 is the solution concentration at the base; γ is the surface tension of solution; C is the concentration; r is the radius of

whisker; M is the molecular weight of the solute. The drag force from viscous stress could be written as,

$$F_{drag} = \frac{2\pi r l \eta V}{\tau} \qquad 1.23$$

where l is the whisker length; η is the viscosity of solution, V is the mean velocity of the liquid film and τ is the thickness of liquid film. By equating the driving and drag force,

$$V = \frac{(C_0 - C_1)\tau}{2Ml\eta}\frac{d\gamma}{dC} \qquad 1.24$$

Hence the rate of transport of salt to the whisker tip is

$$Rate = 2\pi r \tau V C_0 \qquad 1.25$$

The rate of whisker growth could be given by

$$\frac{dl}{dt} = \frac{\tau^2 C_0 (C_0 - C_1)}{Ml\rho r \eta}\frac{d\gamma}{dC} \qquad 1.26$$

where ρ is the density of whisker. By integration

$$l^2 = \frac{2\tau^2 C_0 (C_0 - C_1)t}{M\rho r \eta}\frac{d\gamma}{dC} \qquad 1.27$$

By substituting numerical values, the liquid film thickness was calculated to be about 0.05 μm, which is reasonable.

1.5.2 Base Growth Mechanism from Shichiri

Shichiri[35] grew NaCl whisker from saturated solution wetted porcelain and he proved experimentally that the whisker grew from the base. Shichiri proposed a base growth mechanism for NaCl whisker grown from porcelain surface. This mechanism was totally different from Sears' theory. Shichiri concluded that:

(a) The growth of whisker was from the base and during growth the whisker inclined on the porcelain was supported by the surface tension of a liquid layer between whisker and porcelain surface.

(b) The porosity of the porcelain was considered only as a factor in maintaining the wetness of the porcelain.

(c) As no further growth of the whisker was observed when the whisker was immersed in a supersaturated salt solution, the whiskers grown from the porcelain substrate was considered to be free of dislocation.

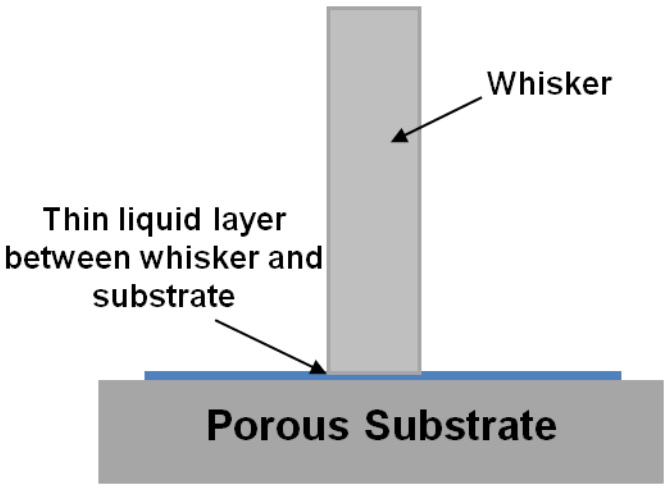

Figure 1.15 Schematic drawing for base growth mechanism of whisker proposed by Shichiri.

1.5.3 Base Growth Mechanism from Amelinckx.

Amelinckx [25] produced whiskers of NaCl, KCl and KBr by storing slightly under saturated salt solution in a container of thin cellophane. Amelinckx found that the whiskers grew from the base and proposed a base growth mechanism. However, it is quite different from Shichiri's theory[35]. Amelinckx found that some of the whiskers were hollow and presented a channel along their axis over part or the whole of their length. Some whiskers were kinked over 90° and some had a small platelet at the tip. Based on these observations, Amelinckx suggested the mechanism of whisker growth as follows;

(a) The growth of whisker took place at the base.

(b) The whisker started with a small crystal containing a screw dislocation perpendicular to the base.

(c) The crystal was kept in place by capillary force.

(d) As the major part of the solution that fed the crystal come from outside, growth started first at the periphery of the crystal.

(e) If enough solution was available, growth could proceed to the center of the dislocation induced spiral, a solid whisker was obtained. If only small quantity of solution was available, growth would be restricted to the periphery and a tube like whisker would form.

(f) In the final stage peripheral growth dominated and a pyramidal base was developed.

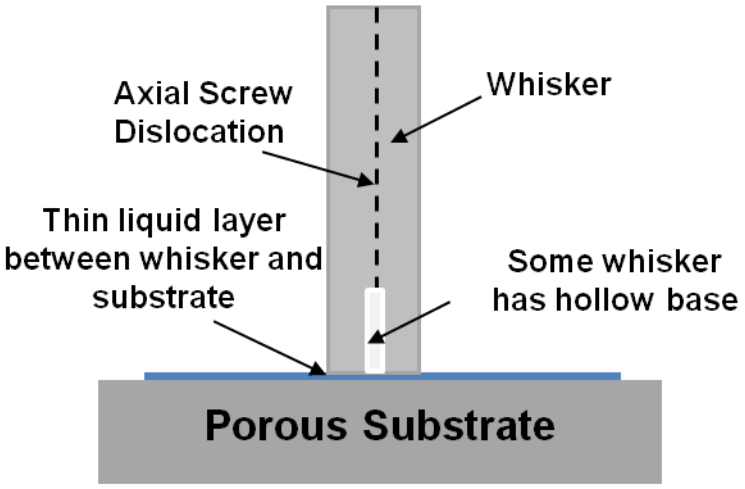

Figure 1.16 Schematic drawing for base growth mechanism of whisker proposed by Amelinckx. Adapted from Amelinckx[25].

These mechanisms conflicted with each other, and seemed to work only in certain circumstance. A dislocation was necessary in Sears and Amelinckx's model, while it was excluded by Shichiri in his theory. The whisker grown from tip or from base was only

observed by naked eye, no detailed microstructure information was provided till now. No advances have been made over the last 30 years. With advanced characterization techniques, further investigation is possible and necessary.

1.6 Motivation and Objective

In early studies of whiskers, the optical microscope was the main tool used to observe the whiskers.[7, 34, 41, 42] This limited the whisker research to the micron scale, and the microstructures of the whiskers were not investigated in finer detail. With rapid development of the techniques, advanced characterization methods such as high-resolution scanning electron microscopy (SEM), transmission electron microscopy (TEM), atomic force microscopy (AFM) and scanning tunneling microscopy (STM) enable scientists to investigate materials further into the nanometer scale and sometimes atomic resolution can also be achieved and it provides a good opportunity for scientists to revisit the researches of whiskers decades ago in smaller scale.

The resurgence of interest in one dimensional crystal started in 1990s after the discovery of carbon nanotube. Assisted by the TEM, Iijima[43] discovered carbon nanotube, which is the forth form of elemental carbon besides diamond, graphite and fullerene. A new era for nanoscience and nanotechnology began since then. Many papers about nano-related materials have been published each year.

Nanomaterials, such as nanotubes and nanowires extensively studied today can actually be considered as whiskers of nanometer scale. Furthermore the most popular fabrication methods for these nanomaterials nowadays are also similar to the techniques used for whisker growth 50 years ago such as vapor-liquid-solid (VLS) method and direct growth in solution method. As discussed in section 1.4, whisker growth from solution on

porous media was another well developed fabrication method in early years. However, one dimensional nanomaterials grown by this method has not been reported till now. It is an opportunity for us to carry out further investigation on whisker growth by this method at submicron and perhaps nanometer scale.

The objective of this research project is to explore whisker growth from solution on porous substrate and finally establish a technique to fabricate whiskers in a controllable way and reduce the diameter of whisker to nanometer scale.

1.7 Potassium Chloride

Several candidate salts (NaCl, NaBr, KCl, KBr) are tried for whisker growth. These salts are all ionic salt with same rocksalt crystal structure, and they were expected to show similar whisker growth results. KCl is finally picked out to be our main research focus due to its outstanding ability to crystallize in the whisker form. Whisker grown with potassium chloride solution usually took less time to reach same length than whiskers made of other material. Potassium chloride (KCl) was also widely used in previous studies about whisker growth.[9,10,36,37]

Potassium chloride is a metal halide. It is an odorless, white or colorless crystal. Potassium chloride crystal is face centered cubic (Rock Salt). Potassium chloride is a strong electrolyte. When it dissolves in water, it dissociates completely into K^+ and Cl^- ions. The main properties of potassium chloride are listed in the Table 1.3.

Table 1.3 Properties of potassium chloride

KCl Properties	
Color	White
Melting Point	771°C
Boiling Point	1500°C
Density	1988kg/m^3
Formula weight	74.551
Relative humidity of saturated solution at 25°C	84.34%
Solubility	Water 35.5 g/100ml 25°C
K^+ Ionic Radii	1.52 Å
Cl^- Ionic Radii	1.67 Å
Lattice Constant	6.29Å
Crystal structure	Rocksalt

1.8 Overview of Thesis Structure

In this thesis, Chapter 1 to Chapter 4 covers the studies on the salt crystal whisker growth on solution saturated nanoporous coating and Chapter 5 focuses on coating onto open celled foam.

Chapter 1 introduces whisker growth fundamentals and provides an overview of critical issues related to crystal growth. In section 1.1, the history of whisker is introduced. The discovery of whisker, the traditional whisker growth methods and the special mechanical and physical properties associated with whisker are briefly discussed. In Section 1.2, the basics of crystallization including supersaturation, nucleation and the crystal growth are covered. Section 1.3 discusses the computer simulation study of NaCl crystal growth on atomic level. Section 1.4 covers the background of whisker growth on porous media and Section 1.5 summarizes three conflicting whisker growth mechanisms proposed by different scientists decades ago. Section 1.6 states the motivation and objective of the whisker growth project. Section 1.7 lists some physical properties of potassium chloride, which is the main material used for whisker growth in the whisker growth research.

Chapter 2 covers the investigation of the single crystal salt whisker growth on nanoporous coating and a base growth mechanism is proposed. In Section 2.1, a brief review of researches on salt solution transportation and crystallization in porous media for art objects protection is provided. In Section 2.2, salt whisker growth on nanoporous

coating under standard growth condition is presented. The effects of relative humidity and salt concentration on whisker growth are studied. Based on the experimental results, transportation phenomenon of liquid in porous coating is discussed and the whisker base growth mechanism is proposed. A special crystal morphology- salt crystal sheet is also mentioned.

Chapter 3 includes investigations of the effects of other experimental variables on whisker growth. In Section 3.1, the effect of porous coating thickness on whisker growth is studied. In Section 3.2, the effect of porous coating particle size on whisker growth is investigated. The relationship between particle size and whisker lateral dimension is suggested. In Section 3.3, the effect of growth angle on whisker growth is examined. The existence of a liquid supporting layer at the whisker base that maintains the stability of whisker during growth is proposed and a brief calculation of the torque and force balance for tilting whisker is presented. In Section 3.4, whisker growth was studied by Cryo SEM method in order to reveal support liquid layer at whisker base. In Section 3.5, free particle method for whisker growth is studied. Colloidal silica particles were added to the salt solution and whisker growth could be observed on the self-assembled nanoporous coating.

Chapter 4 focuses on reducing whisker lateral dimension to nanometer scale. In Section 4.1, traditional strategies for one dimensional crystal synthesis are reviewed, and possible growth mechanism for salt whisker in our research is discussed. In Section 4.2, experimental details about whisker lateral size control are provided. In Section 4.3, two strategies to reduce whisker width are studied. For the 1st strategy, patterned nanoporous

coatings are used to limit liquid supply to the whisker growth and for the 2nd strategy, seeds are purposely placed onto the nanoporous coating surface to initiate simultaneous whiskers growth. In Section 4.4, future work about whisker growth on nanoporous coating is discussed.

Chapter 5 covers the studies of coating onto open celled foam structure. In Section 5.1, background of open celled foam is provided. Motivation and objective of this research are also discussed. In Section 5.2 includes the experimental. In Section 5.3, a noval two step coating process combining dip coating and spin treatment for open celled foam structure is demonstrated and the effect of experimental variables on coating thickness is studied. This coating process is successfully used to apply γ-Al_2O_3 coating onto carbon foam and zeolite coating onto alumina foam for catalytic applications.

Chapter 6 is a brief summary of the entire thesis.

Chapter 2 Whisker Growth on NanoPorous Coating

2.1 Introduction

Besides researches of whisker growth on porous media, the crystallization of salts inside and on masonry, concrete and art objects also has been studied for many years.[44-49] In service, building materials may be exposed to a source of water that contains a dissolved salt, and on drying, salt crystallizes on the surface (efflorescence) and inside the material (subflorescence). The microstructure of efflorescence takes a variety of forms; in some cases, whiskers are found.[50, 51]

Researchers in this field have considered the transport phenomena that govern the position of the liquid meniscus in the porous material. Lewin[52] predicted the location of the saltwater meniscus, and presumably the site of salt deposition, by setting equal the rate of liquid flow to the surface and the rate of exit from the surface by evaporation. The rate of liquid flow to the surface is influenced by the pore structure and fluid properties, while the evaporation rate depends mainly on the relative humidity. Experimental studies of efflorescence agree with this general framework; namely, efflorescence is more likely under conditions of high relative humidities[53-55] where this balance allows the meniscus to remain at the surface. Puyate and coworkers[54, 55] described the transport phenomena in more detail. They developed a 1D model that includes a diffusion-convection equation to determine the ionic composition distribution in the pore liquid.

In this chapter, we develop a method to create salt crystals from solution using nanoporous coatings as a platform for growth and potassium chloride as a representative alkali halide. The effects of humidity and solution concentration are characterized. Electron and optical microscopy results are used to determine the transport phenomena that influence whisker formation and the mechanism of whisker growth. In addition, a new morphology – a salt crystal sheet – is also described.

This chapter is adapted from paper "Formation of Salt Crystal Whiskers on Porous Nanoparticle Coatings" published in Langmuir 26, 2847, 2010. by Heng Zhang H, Zhen Wu and Lorraine F. Francis.

2.2 Whisker Growth under Standard Growth Condition

2.2.1 Experimental Section

Preparation of porous coatings. Coatings were prepared by dip coating of aqueous silica dispersions onto 1” x 3” glass slides. Glass slides were cleaned with detergent in an ultrasonic bath, then rinsed with ethanol and distilled water, and dried in an oven at 120 ℃ for one hour. Coating dispersions were prepared using Cabot PG-022 (Cabot Corporation), an aqueous dispersion of cationically surface treated, silica nanoparticle aggregates (150 nm aggregates of 20 nm individual particles). The stock dispersion was diluted with distilled water to a solids loading of 10 wt% and ultrasonicated for 10 minutes before coating. Coatings were prepared by dip coating at a rate of 0.2 mm/s. Immediately after deposition, the back and side edges of the substrate were wiped clean and then the glass slide with coating on one side was dried at 70 ℃ for one hour.

Whisker growth on porous coatings. The experimental set-up for whisker growth is shown in Figure 2.1. Salt solution was prepared by mixing the required amount of potassium chloride (99.6%, Mallinckrodt) with distilled water and ultrasonicating until completely dissolved (~10 min). The salt solution was added to a 50 ml graduated cylinder outfitted with a small rubber stop to hold the coated substrate. The graduated cylinder with solution was then placed into a humidity-controlled box (Electro-tech

Systems, Inc., Model 503). The 24”W x 18”D x 15”H box contains a humidity sensor and a small fan for circulation. Preliminary experiments showed that the position of the graduated cylinder relative to the fan was important to the growth and hence the position was kept constant (25 cm vertical distance and 20 cm horizontal distance from the fan) for all studies reported here.

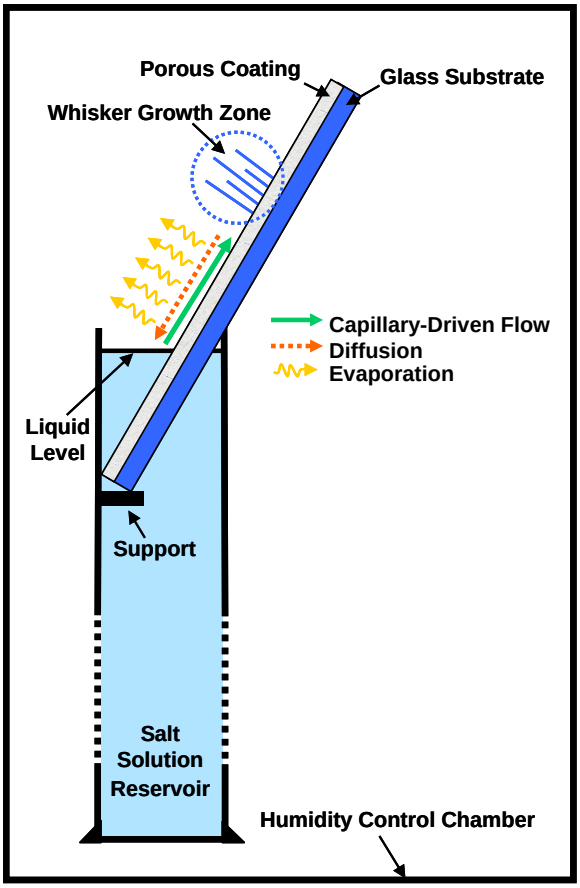

Figure 2.1 Experimental set-up for whisker growth on porous coatings. Not to scale.

After the desired relative humidity was achieved, the box was briefly opened to put the coated substrate in place, starting the experiment. The set-up was then left

undisturbed for the growth period, typically two days. During this time, the level of the salt solution dropped due to evaporation; the concentration of the salt solution in the graduated cylinder remained nearly constant as the liquid volume change was less than ~2%. At the completion of a growth experiment, the coated substrate was carefully removed and allowed to dry in ambient conditions.

The effects of two variables, relative humidity and solution concentration, were explored, as described in Table 2.1. The standard conditions, chosen after considerable preliminary research, represent conditions that produced mostly solitary and straight whiskers. The standard solution concentration, 2.9 wt%, is about 10% of the saturation concentration for KCl in water. Variations from the standard conditions were made to explore the effects of experimental conditions on growth.

Table 2.1 Conditions used for 2-day whisker growth studies

Case	**RH (%)**	**KCl Conc. (wt%)**	**Whisker Morphology**
Standard	80	2.9	Long, straight
Relative Humidity (RH) Effect	60 65 70 75 80	2.9	Short with crystal crust Short with crystal crust Short, curved Long, straight or curved Long, straight
Solution Concentration Effect	80	1.5 2.9 9.1 23.1	Straight Straight Straight Straight, with equiaxed crystals

Studies of liquid flow. The initial flow of salt solution into the porous coating was visualized using a digital optical microscope (Hirox MX series). For imaging purposes, the coated substrate was held vertically in a 10 ml beaker and the assembly was placed near the transparent wall of the humidity control box. The microscope's macrozoom lens (MX-MACROZ VI) was mounted horizontally and focused on the coated substrate from outside of the box. After the required relative humidity was reached, salt solution or water was poured into the beaker and imaging began. The relative position of liquid front in the porous coating was recorded at 15 s intervals. The effect of relative humidity and salt solution concentration on the liquid front movement was characterized. Steady state was achieved in one hour or less.

Whisker growth visualization. The growth of whiskers was captured using an optical microscope (Olympus BX60) outfitted with a CCD camera. A growth set-up was designed for the geometry of this standard microscope. A coated glass slide coated was placed on the microscope stage and the coating surface was covered with 250 μl of KCl solution (2.9 wt%). The solution wicked to the edge of the slide, which was also coated with silica nanoparticles and whisker growth occurred outward from the coated edge. Images of whiskers emerging from the edge were gathered sequentially. This experiment was carried out under ambient conditions with the relative humidity in the range of 65 to 70%. Experiments carried out on days with lower relative humidity did not yield straight whiskers.

Characterization. After growth was complete, whiskers were characterized by several methods. Coated substrates with whiskers attached were imaged with a digital

optical microscope (Hirox MX series). Substrates were carefully fractured into smaller pieces for examination with field emission scanning electron microscopy (FESEM). Specimens were coated with 5 nm of platinum before imaging in a Hitachi S-4700 FESEM. Microdiffraction (Bruker-AXS Microdiffractometer) was used to verify the portions of coatings that were exposed to salt solution. Single whiskers and sheets grown under standard conditions were detached from the substrate and examined by microdiffraction. One whisker and one sheet were additionally characterized by using a Bruker-AXS X-ray platform diffractometer.

2.2.2 Results

The dip coated porous coating was measured by SEM and was shown in as shown in Figure 2.2. Coating thickness was ~0.35 μm. Because each 150nm silica particle was agglomerate of 20nm silica particles, the coating was not close packed and the pore sizes of the coating were varied.

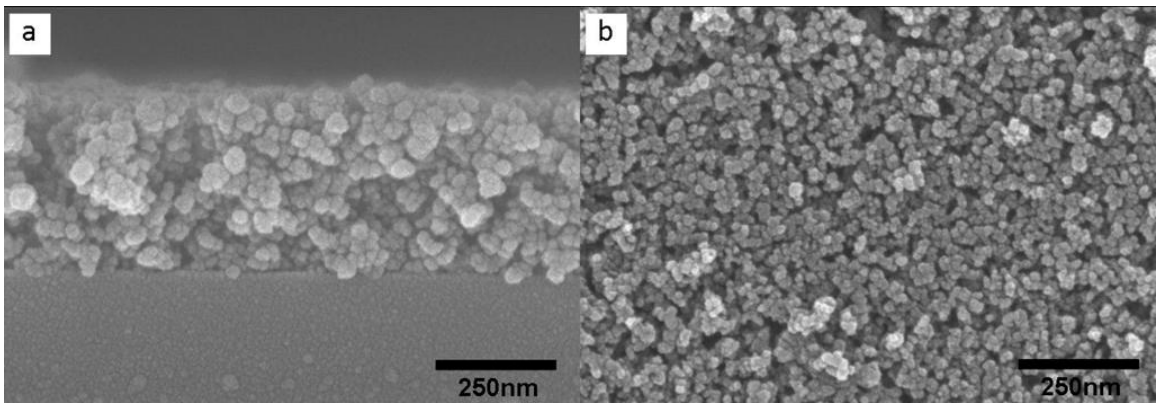

Figure 2.2 SEM images of the silica nanoparticle porous coating used as a platform for whisker growth: (a) cross section and (b) top surface.

Whisker growth under standard conditions. The standard conditions, chosen after considerable preliminary research, represent conditions that produced mostly solitary and straight whiskers. The standard solution concentration, 2.9 wt%, is about 10% of the saturation concentration for KCl in water. Variations from the standard conditions were made to explore the effects of experimental conditions on growth and will be discussed in detail later. The optical microscope image of whiskers grown for two days on porous coating under standard growth conditions was shown in Figure 2.3. A visible zone of whisker growth is found on the coating well above the original liquid level. Whiskers were first visible to the naked eye after approximately seven hours. More whiskers appeared as the liquid level in the graduated cylinder dropped slowly. These whiskers were identified as KCl by X-ray diffraction, as described later.

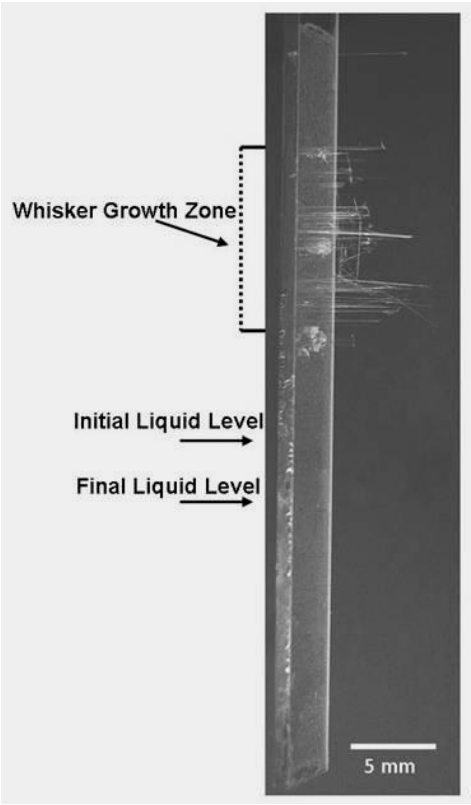

Figure 2.3 Digital image of a specimen after standard whisker growth on a porous coating. Growth occurred for two days at 80% RH using a 2.9 wt% KCl solution.

Figure 2.4a shows an SEM image of the whisker growth zone after the two-day growth period. Most whiskers are straight with rectangular cross-sections and lateral dimensions on the range of 2 to 50 μm and lengths up to ~5 mm. Based on measurements of 225 whiskers, the average lateral dimension was 11 μm with standard deviation of 7.5 μm. Some crystals with sheet-like morphologies and fallen whiskers are also present, as described more in section of sheet growth mechanism.

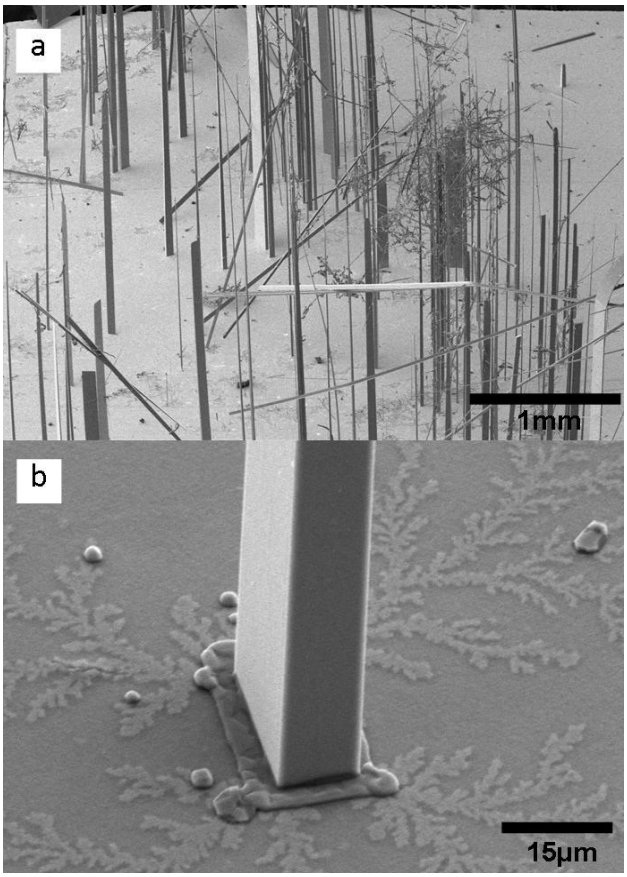

Figure 2.4 SEM micrographs of whisker growth zone after standard growth conditions: (a) overview and (b) high magnification of a whisker base.

Figure 2.4b shows higher magnification image of a whisker base. Here, the surface of the porous coating is visible along with a dendritic pattern. The dendritic pattern appears to be the consequence of crystallization of the pore liquid after the specimen is removed from the growth chamber; the glass substrate turned from transparent to whitish immediately after being pulled out of the solution reservoir, indicating crystallization. Interestingly, this crystallization appears to take place within or below the porous coating. A layer of equiaxed crystals is around the whisker base, its

rectangular shape matches the shape of the whisker base. Such crystals were frequently found at whisker base.

The morphology at an early stage of growth is shown in Figure 2.5a. A scattering of small equiaxed crystals and tiny whisker-like structures are apparent on the coating surface along with a dendritic pattern. Some tiny whiskers are tilted, and small crystals appear on the tip of other larger whisker-like structures. These small crystals could be seeds for whisker growth, as discussed later. Occasionally silica particles from the porous coating could be observed on top of the whisker, as shown in Figure 2.5b.

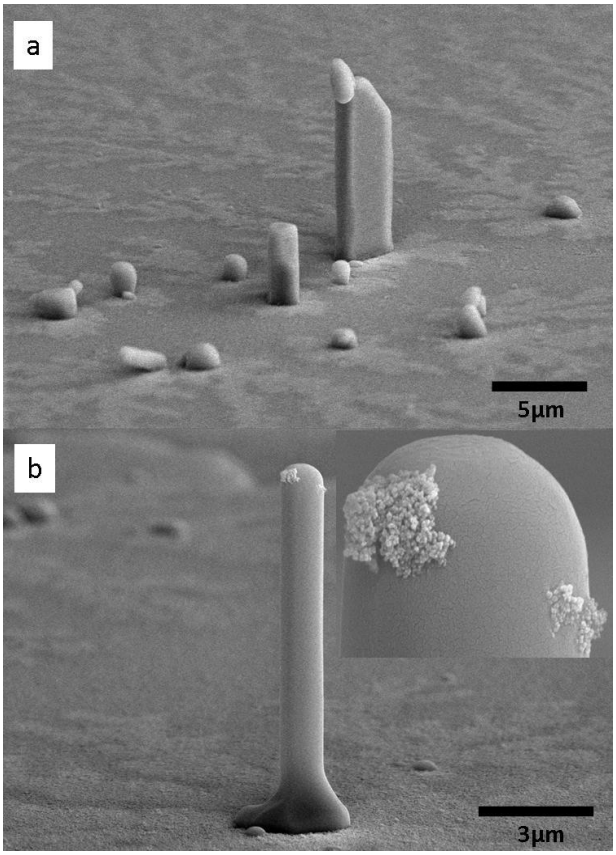

Figure 2.5 SEM micrographs of an early growth stage (1 day under standard conditions): (a) typical morphologies and (b) silica particles from porous coating on the top of a whisker.

Whiskers removed from the coating after the two days of standard growth were examined by X-ray diffraction. Ten long and straight whiskers were chosen and examined by X-ray microdiffraction. The schematic drawing of the experimental setup was shown in Figure 2.6 and the integrated 2 theta plot was shown in Figure 2.7. The results showed that the whiskers are single crystals of KCl with bounding surfaces belonging to the {100} or {110} family of planes; these two sets of planes were indistinguishable by the microdiffraction method. One whisker was further investigated with a single crystal X-ray diffractometer and the crystal faces were unambiguously identified as the {100} family.

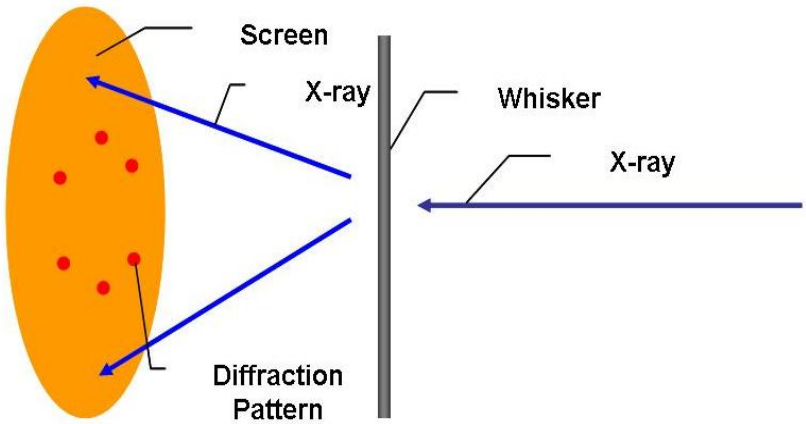

Figure 2.6 Schematic drawing of the experimental setup for X-ray microdiffraction.

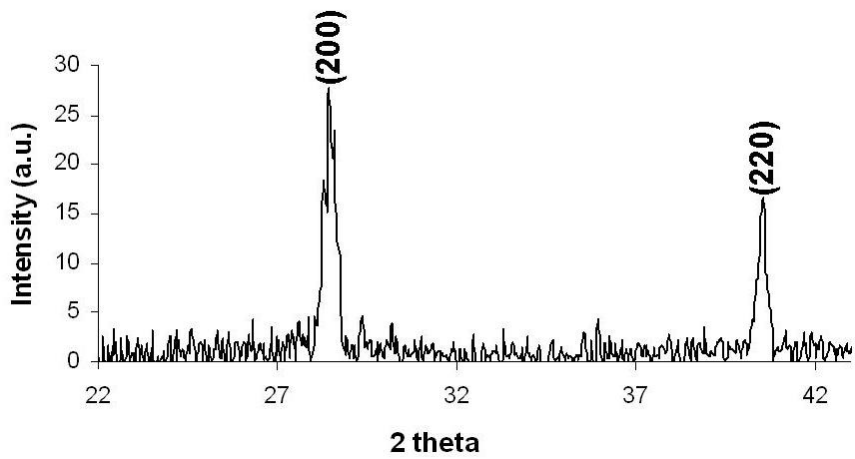

Figure 2.7 X-ray microdiffraction data gathered from a single crystal whisker. The whisker was mounted with its long axis vertical and rotated 360° around its axis during data collection. The plot was created by integrating the signal points gathered on an area detector.

Fallen whiskers, detached from the substrate, were also observed. See Figure 2.4. These whiskers were sometimes propped up by neighboring whiskers. Figure 2.8a shows an example of such whiskers; this pair of whiskers fell onto nearby whiskers and got supported and maintained contact with the porous coating, which allowed further growth. In other cases, an entire whisker fell flat onto the porous coating and then continued to grow as a sheet. Figure 2.8b shows a fallen whisker in contact with the porous coating and was beginning to be pushed up by base growth. In Figure 2.8c, a single fallen whisker led to the growth of two sheets, which are connected on the top by the whisker. The right sheet appears to have grown faster or started growth sooner than the left sheet. Because of lack of contact with the coating or a local deficiency in the salt solution supply, the midsection appears to have prevented a sheet from forming in that region. Figure 2.8d shows another example of sheets grown from the same fallen whisker as a

starting point, however, due to high growth rate difference, one sheet was lifted up by the other one and the inset shows the continuity between the whisker and the sheet. Sheets were also examined by X-ray methods and the faces of the sheets were in the {100} family of planes.

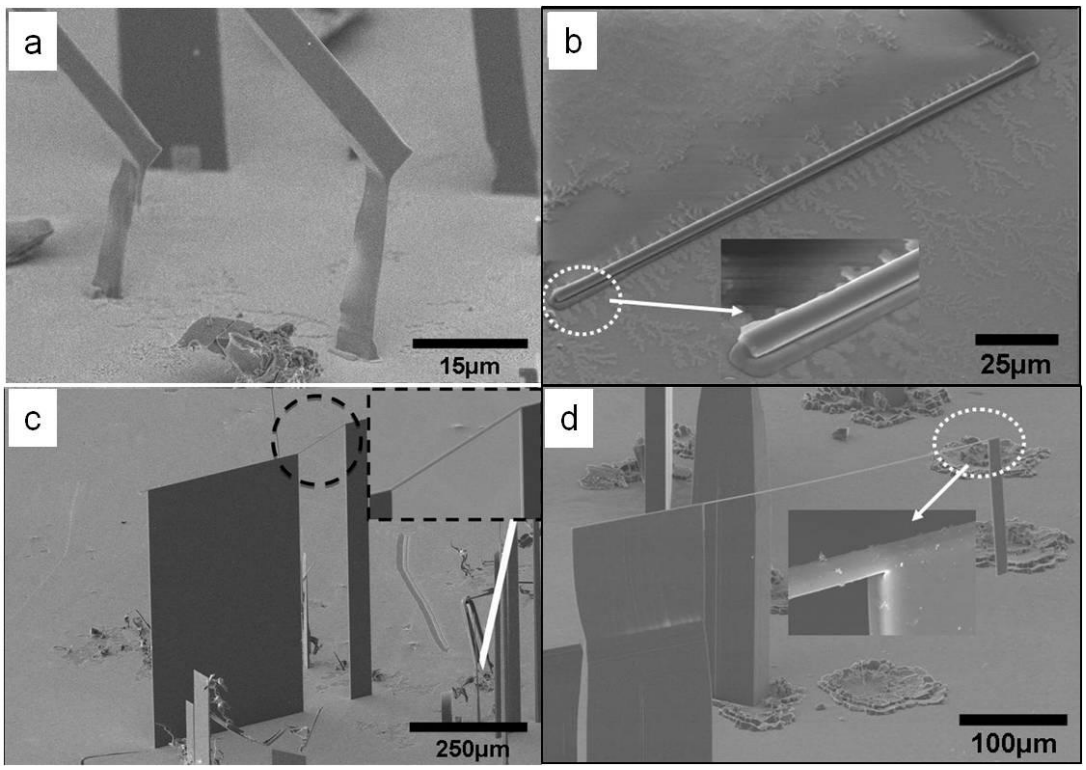

Figure 2.8 SEM micrographs of (a) fallen whiskers that are propped up and remain in contact with the porous coating such that an extension grows. (b) the initial stage of sheet formation. Here the fallen whisker is beginning to be pushed up by base growth. (c) fallen whisker in contact with substrate that continues growth into two sheets connected by the original fallen whisker in the middle (inset figure). (d) two sheets grown from the same fallen whisker as a starting point, one sheet is lifted up by the other. The inset shows the continuity between the whisker and the sheet.

Visualization studies. The first visualization study characterized the movement of water or salt solution into the porous coatings under different conditions. A glass substrate with porous coating was placed vertically in water or salt solution and a digital

optical microscope was used to track the upward motion of a liquid front into the porous coating. Figure 2.9a shows an example of the progression of the liquid front under standard conditions. By one hour, the front reaches the end of the coating.

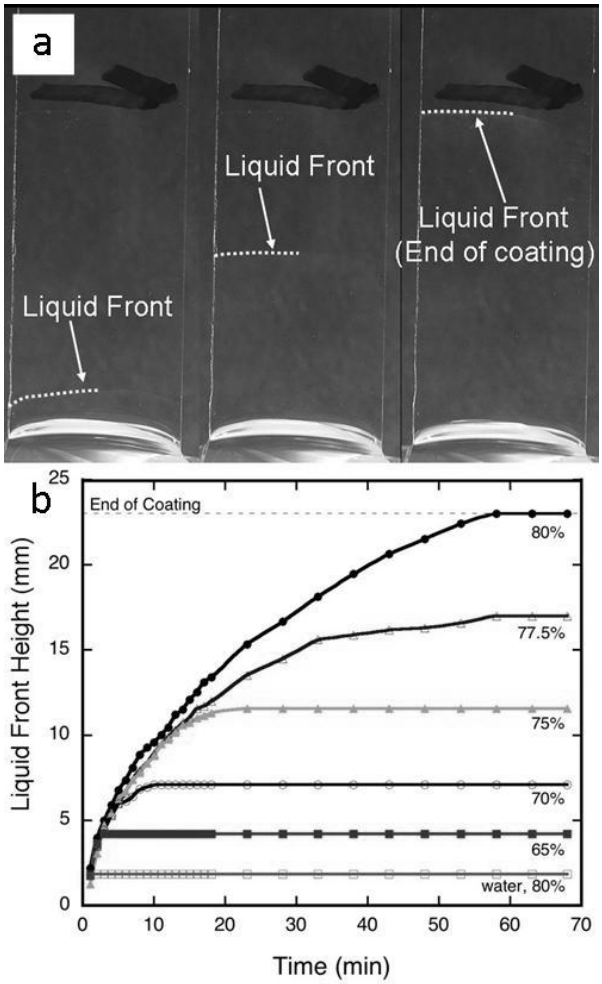

Figure 2.9(a) Digital images of the liquid front in the porous coating; left to right 1 min; 20 min; 1 hour after immersion into the KCl solution at 80% RH. (b) Effect of relative humidity on liquid front position for KCl solution (2.9 wt% KCl) in porous coatings, and liquid front position for water in porous coating at 80% RH.

Figure 2.9b is a summary of liquid front movement for all the conditions tested. When water was used, the liquid front rises quickly to about 1 mm above the contact line

under the standard humidity condition (80% RH). However, when a salt solution is used under the same conditions, the liquid front rises up over 2 cm to the end of the porous coating itself. The visualization also revealed a hazy zone near the wetting front for salt solutions. This hazy zone moved up the coating as the liquid penetrated further and disappeared gradually after the liquid front reached the upper end of the coating. When the relative humidity was lowered, the liquid front height for a given salt solution decreased. X-ray microdiffraction was used to demonstrate the validity of liquid front tracking. The specimen used to track the liquid front position for a KCl solution at 75% RH was examined above and below the liquid front line. KCl crystals were found below but not above the line, confirming that salt solution had not reached above the front.

The second visualization experiment captured whisker growth under near standard conditions. Figure 2.9 shows sequential images of whiskers growing on the edge of a glass slide, as imaged with an optical microscope. As described, the experimental set-up for the visualization was different than that used in the growth experiments; however, the important features are the same. Salt solution imbibes the porous coating, and evaporation ensues followed by salt crystallization and whisker formation.

In Figure 2.10, the central whisker in the images increases in length with time at a rate of about 0.02 mm/sec. As growth occurred, some whiskers were observed to sway, change orientation and sometimes fall over or leave the field of view. The small crystal at the tip of this whisker is pushed further away in the process. This result indicates that the whisker grows from the bottom or base upward. Another example of sequential

whisker growth was shown in Figure 2.11. Each whisker was labeled with a number for easy tracking. Whisker 1 is a pair of separate whiskers at early growth stage, from $time_3$, a crystal formed between them and connected the two whiskers to each other near the substrate. The whisker pair seemed to be unbalanced and tilted at t_4, however, the tilt angle was reduced in t_6 indicating the whisker pair tried to restore their balance. Whisker 4 has a small crystal attached to the tip during growth and the tip did not change shape during growth. Whiskers 3, 4 also changed their angles, demonstrating that the whiskers were not stable during growth. Fallen whiskers are a starting point for the formation of sheets.

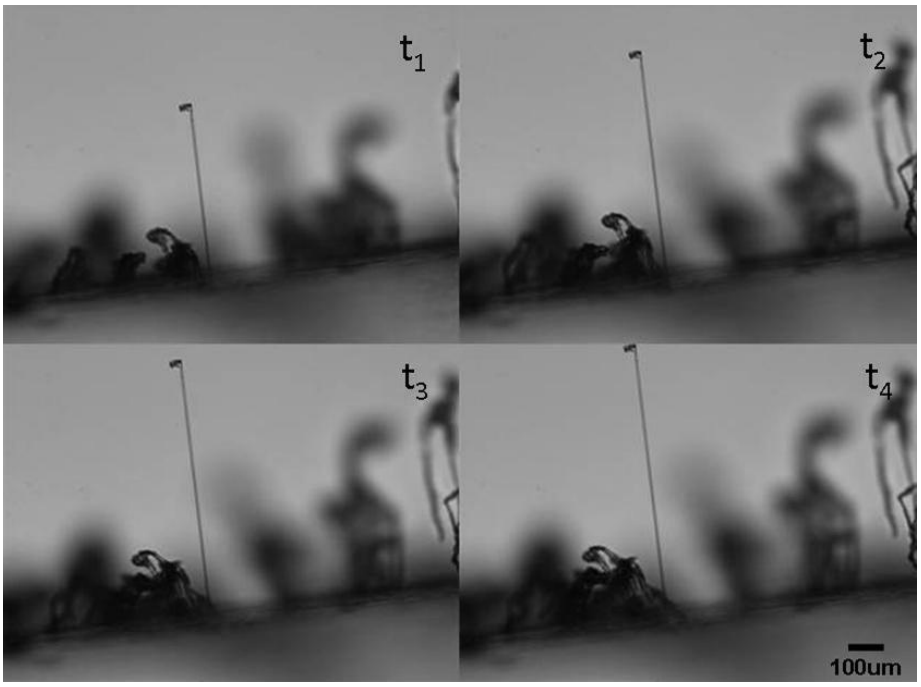

Figure 2.10 Optical micrographs of the growth of whiskers on a porous silica coating with increasing growth time ($t_1 < t_2 < t_3 < t_4$ with time interval 5 s). The central whisker has a small crystal attached to its tip, making apparent the growth by extension from the base.

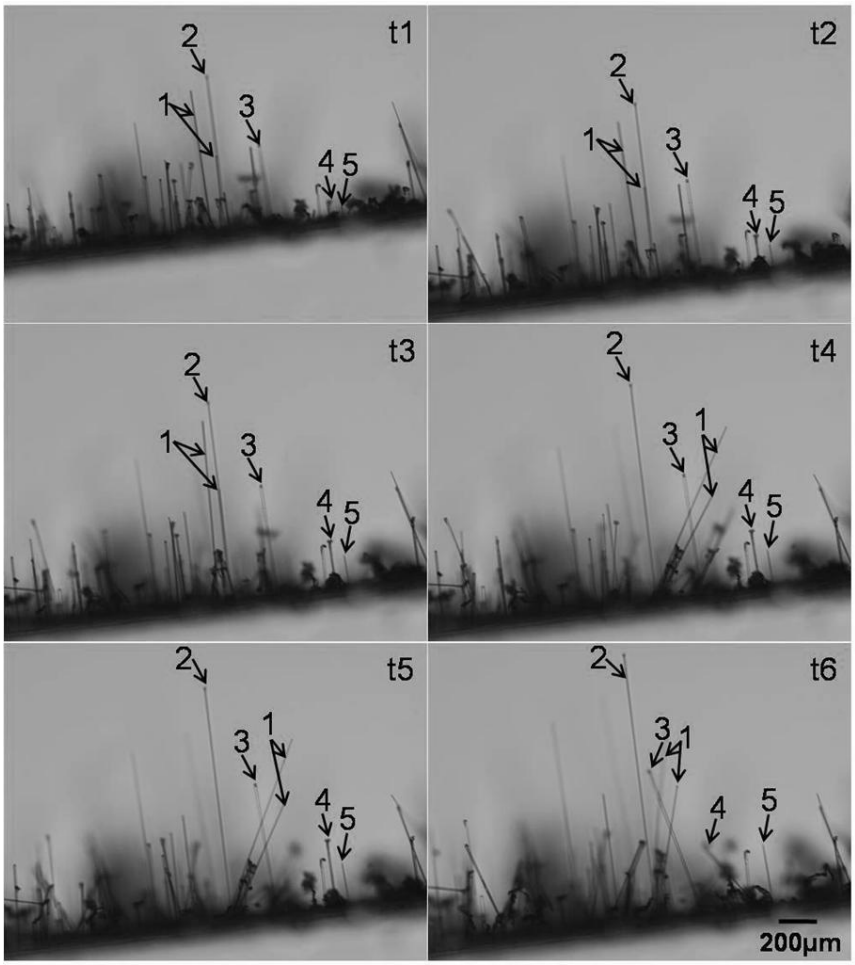

Figure 2.11 Optical micrographs of whiskers on a porous silica coating with increasing growth time ($t_1 < t_2 < t_3 < t_4 < t_5 < t_6$; total growth time = 108 s). Whiskers are labeled with numbers for easy tracking.

Effect of Relative Humidity. The effect of relative humidity on whisker growth was studied by varying the relative humidity from the standard conditions. Whiskers were observed over a range of humidities, 60 - 83% as shown in Figure 2.12; however, whiskers grown at the lower end of this range were severally stunted by a non-whisker salt crust. As relative humidity increased, the position of the whisker growth zone shifted from nearer to the liquid level to further away, consistent with the visualization of liquid penetration.

Figure 2.12 Digital images of specimens grown from solutions of varying KCl concentrations, as indicated, with all other conditions the same as the standard condition. The right end was the one immersed in the salt solution.

The whisker morphology also changed with relative humidity as shown in Table 2.1. As the relative humidity dropped from 80% (standard) to 75%, whiskers became more curved and irregular. Curved whiskers may be related to the uniformity of supply of salt solution to the whiskers, as suggested by previous researchers[52], Or it could be induced by various outside disturbances. The quantity of whiskers appeared to be greater at 75% RH as compared with 80%, but whisker dimensions were similar. Lowering the humidity further to 65% led to a change in morphology as shown in Figure 2.13a. Fine, short whiskers and a continuous layer of non-whisker crystals covered the "whisker growth zone". Figure 2.13b show this morphology for whiskers grown at even lower relative humidity (60%). Here, it appears that the crust of equiaxed KCl crystals choked the salt solution supply to the whiskers, stunting their growth.

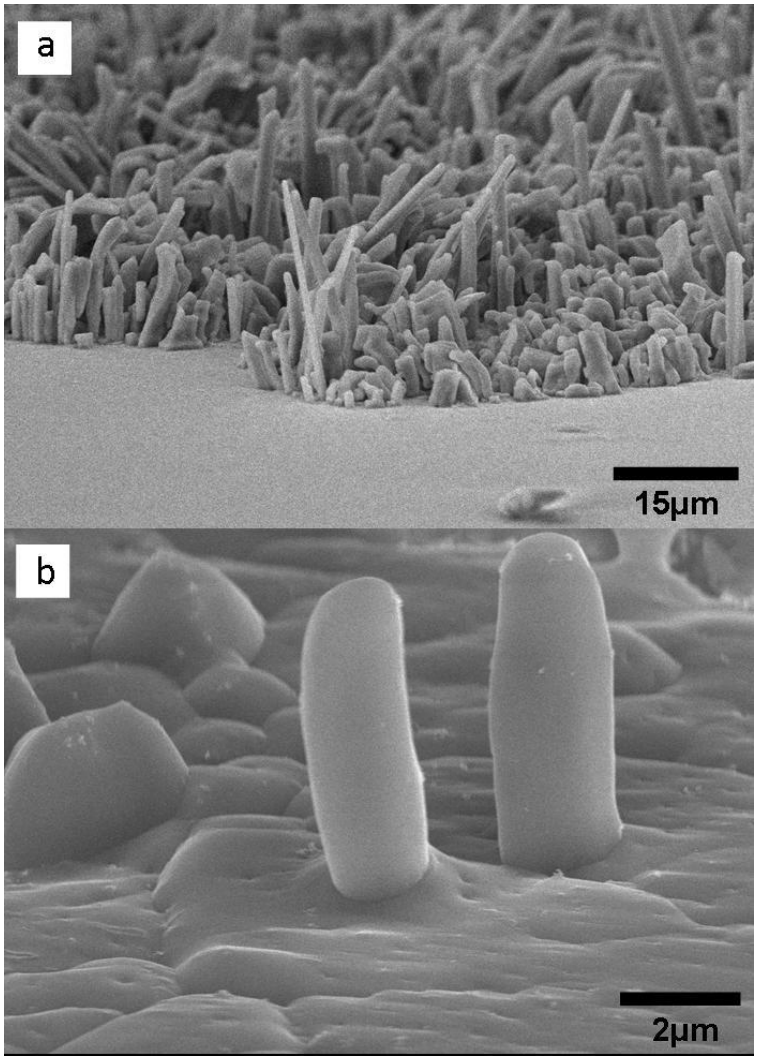

Figure 2.13 SEM micrographs of the whisker growth zone under conditions of (a) 65% relative humidity with all other conditions the same as the standard condition and (b) 60% relative humidity with all other conditions the same as the standard condition.

Figure 2.14 shows specimens grown from KCl solutions with varying concentration at 80% RH. As concentration increased, whiskers appeared earlier in the two-day growth period, the quantity of whiskers increased, and the growth zone moved closer to the original liquid level. Regardless of concentration, whiskers were straight

and had about the same lateral dimensions. At the highest concentration, equiaxed crystals were incorporated in the growth zone.

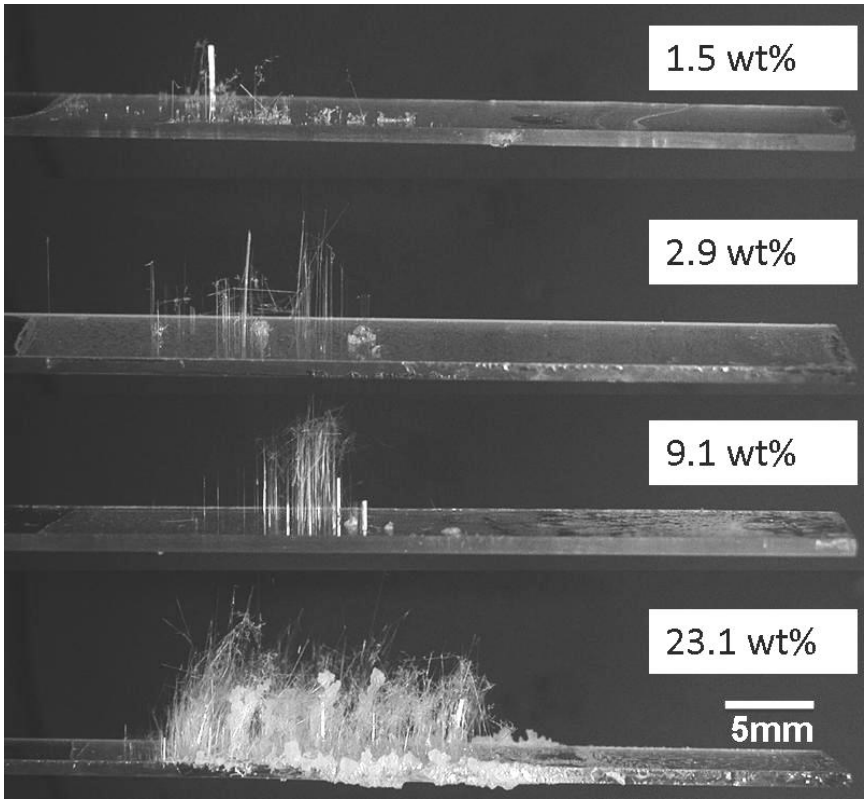

Figure 2.14 Digital images of specimens grown from solutions of varying KCl concentrations, as indicated, with all other conditions the same as the standard condition. The right end was the one immersed in the salt solution.

2.2.3 Discussion

In this section, the transport phenomena that create the conditions for crystallization are discussed and a whisker formation mechanism is proposed. Models developed for wicking and salt degradation of concrete[50, 52, 55, 56] and convective assembly[57, 57] are used to explain the transport issues that combine to produce a whisker

growth zone. A whisker formation mechanism is then proposed and compared with mechanisms set forth previously in the literature.[24,35,58] In each of the two subsections, the focus is on the standard growth conditions, with results from the effects of relative humidity and concentration used to support the hypotheses.

2.2.3.1 Transport Phenomena.

Three phenomena are important to establishing the conditions for crystallization on the porous coating: capillary driven flow of the salt solution into the porous coating, evaporation of water from the coating surface, and diffusion of ions in the solution-filled pore space. See Figure 2.1.

At the start of the experiment, the salt solution wets the porous coating and is pulled into the coating by the capillary pressure created by curved liquid-vapor menisci. As soon as liquid enters the coating; however, evaporation begins from the coating surface. Therefore, a balance of the two gives the position of the liquid front. The capillary driven mass flux is given by Darcy's Law:

$$J_C = \frac{\kappa \rho \Delta P}{\mu L} \qquad 2.1$$

where L is the length over which ΔP, the pressure drop in the liquid due to capillarity, drives flow; μ is the viscosity of the liquid; ρ is the density of the pore liquid; and κ is the permeability of the porous material. This situation is similar to that analyzed by Brewer and coworkers[57] for flow of water in colloidal crystal coating in which evaporation occurs from the free surface of the coating and water is drawn in by capillary

pressure driven flow. They showed that the pressure gradient that drives flow through the assembled crystal coating is largely one dimensional, increasing up the length of the water-filled thin coating. Therefore when evaporation matches convection, L in Eq. (2.1) represents the final liquid front position, as monitored by visualization experiments (Figure 2.9).

To estimate L, the mass per unit time entering the coating by convection is equated with the mass per unit time exiting the coating by evaporation. For the convection term, the liquid enters via the coating cross-section (HW, where H is the thickness and W is the width of the coating). For the evaporation term the water exits the coating via the coating surface (LW), where evaporation from the edges of the coating is presumed to be small by comparison. Balancing the two gives:

$$J_C(HW) = J_E(LW) \qquad 2.2$$

where J_E is the evaporation mass flux and J_C is given by Eq (2.1). The liquid front position is therefore:

$$L = \sqrt{\frac{\kappa H \rho \Delta P}{\mu J_E}} \qquad 2.3$$

In their work on simultaneous wicking and evaporation from metal weaves, Fries and coworkers[59,60] arrive at a similar result using a more complex approach.

The parameters in Eq (2.3) can be approximated for the standard condition of 80% RH and assuming pure water as the liquid. The pressure drop, $\Delta P = 2\gamma\cos\theta/r$, is ~3

MPa, using surface tension, γ, of 72 mN/m, contact angle, θ, of 0 ° and pore radius, r, of 50 nm. The density and viscosity of the water are 1000 kg/m^3 and 1 mPa•s, respectively, and the coating thickness is ~0.35 μm. The permeability of the porous coating is estimated using the Karmen Cozeny equation[61] $\kappa = \phi^3/[5(1-\phi)^2S^2] = 1.7 \times 10^{-18}$ m^2, using measured values for the pore fraction (ϕ = 0.6) and surface area of (184 m^2/g, corresponding to S = 4 x 10^8 m^2 surface per m^3 volume). The evaporation flux of water at 80% relative humidity in the growth chamber is 8 x 10^{-5} kg•m^{-2}•s^{-1}. Using these approximations, the final liquid front position is ~0.15 mm, which is in the same range as the observed height (~1 mm). The front position for salt solutions is much greater (see Figure 2.9) than water, an effect that cannot be explained by changes liquid properties such as the small (~10%) increases in surface tension[62] and viscosity[40], on the parameters in Eq. 2.3 or by the effect of the salt on the mass balance. The difference may be related the effect of the salt on the evaporation rate.

The evaporation rate depends on the relative humidity (RH) in the surrounding atmosphere, as well as the gas flow conditions:

$$J_E = k(P^* - P^\infty) \qquad 2.4$$

In Eq. (2.4), k is the mass transfer coefficient, P* is the vapor pressure of water in the gas just above the evaporating liquid, and P^∞ is the vapor pressure of water far from the evaporating surface. For pure water, P* is the saturation vapor pressure of water, P_{sat}. and P^∞ depends on the percent relative humidity, RH, and P_{sat} [P^∞ = (RH/100)P_{sat}]. For evaporation from liquid filled pores with tiny menisci, the curvature lowers P* relative to

a flat liquid surface. A calculation with the Kelvin equation[59] reveals that this effect is only significant for evaporation from nanosized pores; for example, the saturated vapor pressure over water with a 50 nm radius of curvature is ~98% of that over a flat surface; therefore, this effect may lower P* and hence the evaporation rate somewhat. In addition, dissolved salt also lowers P*. The equilibrium vapor pressure over a saturated KCl solution at 25 ℃, for example, is 84.34% of that over pure water.[63] The decrease in P* results in a decrease in the vapor pressure difference ($P^* - P^{\infty}$) and hence a lower J_E for a given relative humidity. The depression on p* is one factor that lowers J_E and hence raises L for salt solutions. The other factor is local salt crystallization.

The visualization data of Figure 2.9 can be explained by considering the effect of relative humidity and salt solution composition on J_E and hence L. The higher final liquid front position, L, for salt solutions relative to water (at constant RH) is consistent with the lowering P*, and hence J_E, by the presence of the dissolved salt. As noted below, local salt crystallization may also play a role. The higher L under higher RH conditions (at constant salt concentration) is due to the decrease in the evaporation rate under higher RH conditions.

As simultaneous capillary driven flow and evaporation establish a region of liquid filled pore space in the coating, the concentration of ions within the pore liquid increases. Capillary driven flow brings ions in the water to the evaporating surface, which creates a higher local concentration, and the potential for diffusion to equalize this gradient. Puyate *et al* [55, 56] define a Peclet number (Pe) to represent the competition between capillary driven flow and diffusion:

$$Pe = \frac{v_{p,ave}\ell}{D} \qquad 2.5$$

where $v_{p,ave}$ is the average velocity in a pore, ℓ is the length over which capillary driven flow and diffusion take place and D is the diffusion coefficient. The pore velocity is related to J_C and the volume fraction of pores (ϕ):

$$v_{p,ave} = \frac{J_C / \rho}{\phi} = \frac{\kappa \Delta P}{\phi \mu L} \qquad 2.6$$

Based on the analysis of Brewer and coworkers[57], $\ell = L$,

$$Pe = \frac{\kappa \Delta P}{\phi \mu D} \qquad 2.7$$

Using approximations, Pe is estimated to be on the order of 25. Hence, capillary-driven flow dominates; the salt concentration will rise at the liquid-vapor interface, eventually becoming supersaturated and launching crystallization.

The haziness that developed in the coating near the wetting line is evidence for local crystallization where a supersaturated condition is reached. The hazy zone moved together with the liquid front, indicating that the crystals form and then dissolve as the liquid front moves upward. This local crystallization clogs pores, which along with the depressed p*, decreases the evaporation rate and leads to a higher L for salt solutions as compared wtih water. It is possible that some form of creeping crystallization [64] occurs in which the surface is sealed with a salt layer and the liquid climbs in the coating

beneath it. If such a layer forms it does not persist, because the haziness is transient and whiskers eventually form in a zone beneath the liquid front position. The lower L for salt solutions imbibed at lower RH appears to be a consequence of increased J_E; however, pore clogging may also play a role if the advancing liquid is arrested by more significant local crystallization.

The haziness that develops in the coating near the wetting line is evidence for local crystallization when a supersaturated condition is reached. The hazy zone moved together with the liquid front, indicating that the crystals form in the hazy zone and then dissolve as the liquid front moves upward. The importance of this local crystallization on the rise of the salt solution into the porous coating is not clear. It is possible that some form of creeping crystallization, reported by Washburn [64], is taking place; however, the time scale for the capillary rise in our experiments is much shorter than that typically observed for this creeping process.

The origin and location of the whisker zone is a result of capillary driven flow, evaporation and diffusion. Qualitatively, this combination of effects can be understood as follows. The solution entering the coating has the same concentration as the salt solution in the graduated cylinder, but as this liquid travels up the porous coating under influence of the pressure gradient, which is in the lateral direction up the length of the coating, evaporation takes place and the salt concentration rises. Thus, the salt concentration in the pore liquid increases with distance away from the liquid pool. At some position up the length of the coating, the supersaturation is high enough, and crystal nucleation and growth proceed. This location is the whisker growth zone. Salt is consumed in this zone

and so solution that might proceeds on to the further reaches of the coating is depleted in salt and less likely to drive further growth. So above and below the zone, crystallization is less likely.

This explanation for the growth zone squares with the observations of the effects of solution concentration and relative humidity. As the initial concentration of the salt solution increases, the position of the growth zone shifts to lower levels, nearer to the liquid level. In this case, less evaporation is needed to raise the concentration of the solution as it travels up the coating and hence the zone is closer to the liquid level. Decreasing the relative humidity from the standard case has the same effect: a lower whisker growth zone. In this case, the lower humidity leads to more rapid evaporation and a faster increase in the concentration as the liquid travels up the coating.

2.2.3.2 Whisker Growth Mechanism

KCl forms in the rock salt crystal structure, which is cubic (space group Fm3m). Ordinarily cube-shaped crystals form[20]. The whisker morphology is not expected based on crystallography. In this work, visualization studies and features of the whisker zone microstructures provide evidence for whisker growth by ion addition to bottom face of the crystal, which is in contact with the porous coating. We will call this a 'base growth mechanism', using the term used by Shichiri.[35]

As described above, the pore fluid becomes supersaturated and crystals form. The location of the first crystals is difficult to confirm because once specimens are removed

from the growth chamber the residual salt solution in their pores dries and crystals inevitably form. SEM images taken at the early stages show some crystals on the surface of the coating. See Figure 2.5. These crystals are believed to be the initial stage of whiskers. Silica particles were found occasionally on the tops of some crystals and whiskers (Figure 2.5b), indicating that some crystals originated beneath the surface. It seems more likely that crystals form on the surface, because growth inside the pore space is confined.[65] In addition, Shahidzadeh-Bonn and coworkers[66] also reported the lowering of the interfacial tension during crystallization could enhance the spreading of liquid out of the pores to the surface of the coating. This spreading would facilitate surface crystallization.

A crystal on the surface can grow uniformly so long as salt solution wets the exterior surfaces of the crystal. This uniform growth, however, can only be sustained if the salt solution contacts all the surfaces and is uniformly saturated everywhere. At some point, this condition breaks down and the liquid may only contact the base of the crystal from beneath and the edges of the crystal. The crystal layer at the whisker base (Figure 2.4b) is consistent with the existence of liquid layer wetting the crystal (whisker) surface during growth. The wetting liquid layer provides stability to the whisker. When sample is removed from the solution, the liquid layer at the crystal (whisker) base dries, crystallizing in a ring.

At some point in the process, growth from the underside or base of the crystal occurs at a faster rate than elsewhere and a whisker emerges perpendicular to the substrate. Two key pieces of experimental evidences point to the base growth

mechanism. First, visualization of whisker growth (Figure 2.10) shows that a straight whisker extends without disrupting a small crystal attached near the tip of the whisker. The whisker appears to be pushed upward from beneath. The upward movement of the whiskers was observed repeatedly. Shichiri[35, 67] documented a similar effect.

Second, morphologies arising from fallen whiskers can only conceivably arise from a base growth mechanism. Fallen but propped up whiskers touching the porous coating are pushed up further at their contact points by continued crystal growth supplied from beneath (Figure 2.8). More dramatic are sheet morphologies that arise when a fallen whisker makes extensive contact with the porous coating and growth continues on the face of the whisker in contact with the coating, forming a sheet. These features were commonly observed. Figure 2.15 is a schematic drawing of a time sequence of whisker and sheet growth by the mechanism proposed above. Taller and narrower sheets were also observed to fall onto the coating and grow from their contacting face into 3D objects.

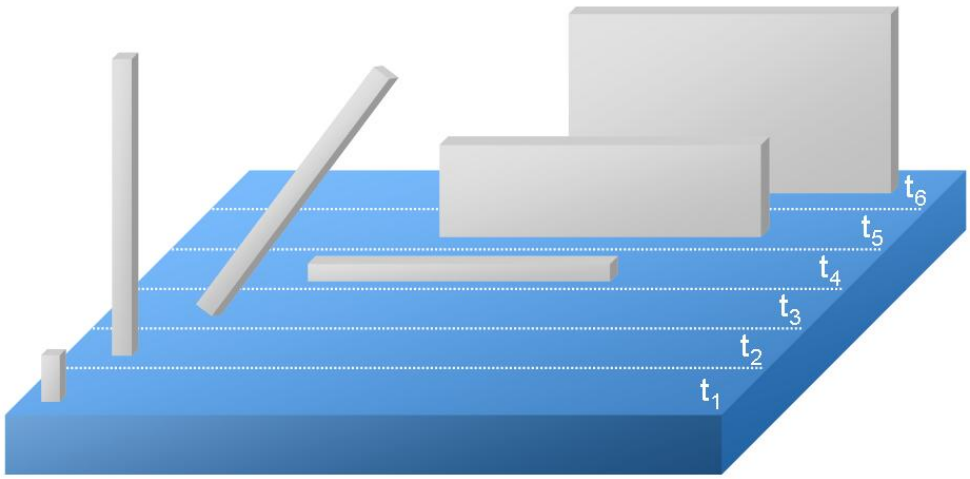

Figure 2.15 Schematic drawing of whisker and sheet growth mechanism in time sequence. ($t_1 < t_2 < t_3 < t_4 < t_5 < t_6$). t_1 whisker starts growing; t_2 whisker continues to grow; t_3 whisker tilts; t_4 whisker falls; t_5 sheet starts to grow, fed from liquid in porous coating beneath; t_6 salt sheet is formed.

There are several possible reasons for the preference for growth on the face in contact with the porous coating. The most likely is that the supply of salt solution is abundant there as compared with the layer of adhering salt solution on the other faces.[68, 69] The ready supply of solution drives growth. Another possibility is that a dislocation or other defect mechanism is at play. The rough surface afforded by the porous coating leads to the possibility that the surface in contact with the coating is defective and growth rate is enhanced.[23] The literature is mixed on the role of defects and dislocations on whisker growth from solution. Shichiri[35, 67, 70, 71] studied dissolution behavior of whiskers and noted that they appear to be defect-free, while Amelinckx[72] documented dislocations in whiskers by a decoration method. We made multiple attempts to locate dislocations in our whiskers, but none were found. Some research on tabular shaped alkali halides[73] suggests that stacking faults may also play lead to rapid and preferred directions of crystal growth. More work is needed to conclusively establish the role of defects in whiskers grown by the method described here.

2.3 Conclusion

Salt crystal whiskers and sheets were formed using nanoporous coatings as a platform for growth. The steps in the growth process were established by characterizing the effects of solution concentration and relative humidity on growth. The solution is pulled into the porous coating by capillarity; concurrent evaporation leads to building of concentration in the pore liquid and a whisker growth zone where the concentration reaches a critical level for formation of salt crystals. Growth occurs by ion addition to the crystal surface that is in contact with the porous coating.

Chapter 3 Other Factors Influencing Whisker Growth

In chapter 2, the effect of relative humidity and solution concentration on whisker growth has been studied and the adjustments of these experimental variables helped us to understand the transport phenomenon and whisker growth mechanism. In this chapter, other experimental parameters, such as nanoporous coating thickness, porous coating particle size and whisker growth angle will be investigated. Furthermore, a new whisker growth mode: growth during convective assembly or free particle growth will also be discussed.

3.1 Effect of Coating Thickness on Whisker Growth

3.1.1 Experimental

In this section, the colloidal silica particle used was Cabot PG 022. The porous coating thickness was increased by repeating the step of dip coating. Between each dip coating step, the coating was dried in the oven at 70°C for 30 minutes. The repetition times were varied from one to four times.

Whisker growth was carried out under standard whisker growth condition (80% Relative Humidity, KCl 2.9wt%, 2 days). See Chapter 2 for details.

3.1.2 Results

The coating thicknesses were measured with cross section SEM and the coating thickness for porous coating coated repeated for 1 to 4 times were ~350nm, 800nm, 1100nm and 1500 nm respectively.

Figure 3.1 shows optical images of whiskers grown on porous coating with different thicknesses. Slightly more whiskers were gained on thicker coatings. Also, whiskers grew at higher locations relative to the initial liquid level for samples with thicker coating. However, the morphology and the lateral dimension of the whiskers did not show noticeable differences as the coating thickness changed.

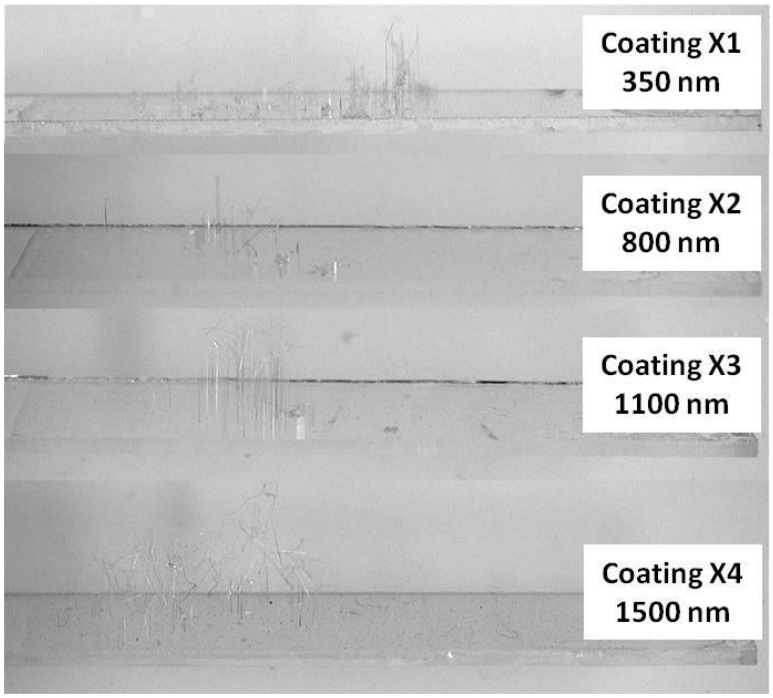

Figure 3.1 Digital images of specimens grown on different coatings with varied thicknesses. All other conditions remained the same as the standard condition described in chapter 2. The right end was the one immersed in the salt solution.

3.1.3 Discussion

The discussion of transportation phenomenon in Chapter 2 shows that the equilibrium height of the liquid front in the porous coating is determined by the balance between capillary driven flow and water evaporation. Equation 2.3 shows the liquid front equilibrium height L is proportional to the coating thickness H and is inversely proportional to water evaporation. Because the porous coating on the edge of the glass substrate is removed after dip coating, for fixed length of substrate, the total coating surface area exposed to the surrounding atmosphere does not change with the coating thickness increase. Hence the water evaporation does not change. However, the coating thickness increases 2 to 4 times compared to the standard coating. Therefore for thicker coating, the solution could reach higher in the porous coating and thus the initial whisker growth position is higher relative to the initial liquid level.

Because the equilibrium liquid front height is larger, the total water evaporation is also larger, and hence the capillary driven flow is larger. More salt ions are transported into the porous coating in same time period and hence the whisker quantity increases with coating thickness.

With more coating repetitions, the coating surface also becomes rougher and it provides poorer support for the whisker. (details for this phenomenon will be discussed in section 3.3) Therefore, more titled or fallen down whiskers could be observed on thicker coating.

In conclusion, porous coating thickness affected the whisker quantity but did not change the morphology and lateral size of the whisker.

3.2 Effect of Porous Coating Particle Size on Whisker Growth

3.2.1 Experimental

A colloidal dispersion of silica particles (22 nm) (Ludox TMA) was purchased from Sigma Aldrich. The stock dispersion was diluted with distilled water to a solids loading of 10 wt% for dip coating.

A colloidal dispersion of silica aggregates of 150 nanometer (PG0-22 150 nm aggregates of 20 nm individual particles) was a gift from Cabot Cooperation. The stock dispersion was diluted with distilled water to a solids loading of 10 wt% for dip coating.

Silica particles of 200 nanometer were synthesized in the lab according to Zhang's paper. [74]. 46 ml of ethanol was mixed with 10 ml of ammonia in a plastic beaker as solution I. 1ml tetraethyl orthosilicate (TEOS) and 4 ml ethanol was mixed in another beaker as solution II. While solution I was under vigorous stirring at 300rpm, solution II was quickly added into solution I at room temperature and the mixture was kept stirring for 10 hours. The synthesized colloidal solution was then centrifuged and ultrasonic bath re-dispersed with ethanol for 3 times and then with distilled water until the pH reached 7. The final weight percentage of silica particle loading in the distilled water is 10 wt%. One drop of as prepared solution was dried on a glass slide and was coated with 5nm platinum for performing particle size checking by scanning electron microscopy on a Hitachi SEM model 4700.

One micrometer silica particle powder was purchased from Sigma Aldrich. The powder was dispersed in distilled water by ultrasonic bath. The solid loading is 10wt% for dip coating.

Coatings were prepared by dip coating of aqueous silica dispersions onto 1” x 3” glass slides. Glass slides were cleaned with detergent in an ultrasonic bath, then rinsed with ethanol and distilled water, and dried in an oven at 120 ℃ for one hour. Porous coatings with particles size ranging from 22nm to 150nm were prepared by dip coating at a rate of 0.2 mm/s. For 200nm and 1 micrometer particle dispersions, the dip coating speeds were increased to 1mm/s and 5mm/s, respectively. Immediately after deposition, the back and side edges of the substrate were wiped clean and then the glass slide with coating on front side was dried at 70 ℃ for one hour.

The experimental set-up for whisker growth was the same as standard whisker growth. Salt solution concentration (KCl) was 2.9 wt% and relative humidity was kept as 80%. For 22 nm particle coating, the relative humidity was lowered to 75%RH because of smaller meniscus formed at the liquid-air interface. While for 150 nm aggregates and 200 nm particle coating, 83% relative humidity was used for whisker growth due to larger meniscus. The growth time was 2 days for all specimens with different particle size porous coating.

Before growth, the coated porous coating substrate was cut and the coating thickness was checked by field emission scanning electron microscopy (Hitachi S-4700 FESEM). After growth, whiskers were imaged with a digital optical microscope (Hirox

MX series) and FESEM (Hitachi S-4700). Specimens were coated with 5 nm of platinum before FESEM imaging.

3.2.2 Results

The thicknesses of porous coatings with different silica particle size were determined by cross-section SEM and the results are listed in Table 3.1. Coating thicknesses for 200 nm and 1 μm particle coating are about 3.5 μm and 20 μm respectively, while coatings made of 22 nm particle and 150 nm aggregates are much thinner. The coating thickness for 22 nm particle coating is about 250nm, and it is slightly thinner than that of 150 nm agglomerate particle coating which has thickness of 350nm.

Table 3.1 Thicknesses of coating composed of different particle size.

Particle Size(nm)	Coating Thickness (nm)
22	**250**
150	**350**
200	**3500**
1000	**20000**

Figure 3.2 shows the digital images of whiskers grown on porous coating with different particle sizes. Compared to standard 150 nm agglomerate particle coating, whiskers grown on 1 μm particle coating were shorter, denser and more curved. A high percentage of equiaxed salt crust could be observed. Whiskers started to grow at the

upper end of the coating. At the end of growth, most of the whiskers are located at the edges of substrate.

Whiskers grown on 200 nm particle coating were longer, thicker and more curved compared to whiskers grown on 150 nm aggregates coating. The whisker quantity is also larger for coating with 200 nm particle. During growth, whiskers started to emerge near the upper end of the porous coating and moved downwards to the liquid level.

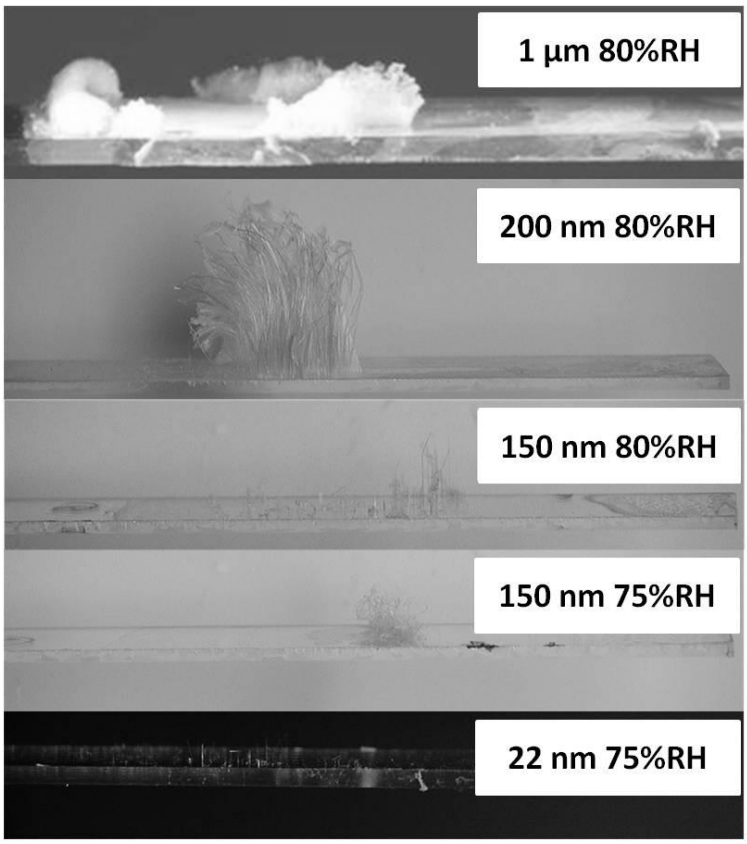

Figure 3.2 Digital images of specimens grown from KCl solutions on porous coating with different particle sizes as labeled on the image. The relative humidity is also labeled and the growth time is two days for all the samples.

Besides whisker quantity and morphology, the average whisker lateral dimension also differed for porous coating with different particle sizes. Generally speaking, the average lateral dimension is positively related to the particle size. For 1 μm particle coating, higher percentage of equiaxed crystal made measuring the whisker lateral dimension difficult. The average whisker lateral sizes for 200 nm, 150 nm aggregates, and 22 nm particle coating were ~20 μm, ~10 μm, and ~10 μm. For 200 nm particle, the whiskers tended to fuse together as shown in Figure 3.3 and the lateral dimensions was referred to the width of an individual whisker. For 22 nm particle coating, the average whisker width was similar to that of 150 nm aggregates coating. However, some fine whiskers with lateral dimension about 2 μm could also be observed on 22 nm particle coating and these whiskers were not included when calculating the whisker average lateral size. See Figure 3.4b.

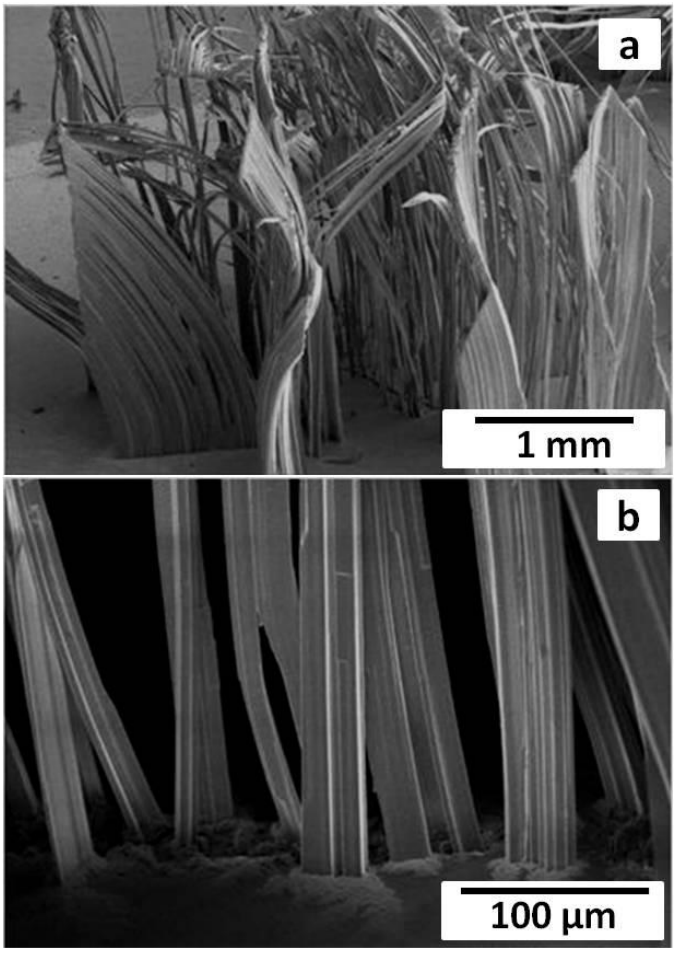

Figure 3.3 SEM images of specimens grown from KCl solutions on 200nm silica particle porous coating under standard growth condition. (KCl 2.9wt%, 80% RH)

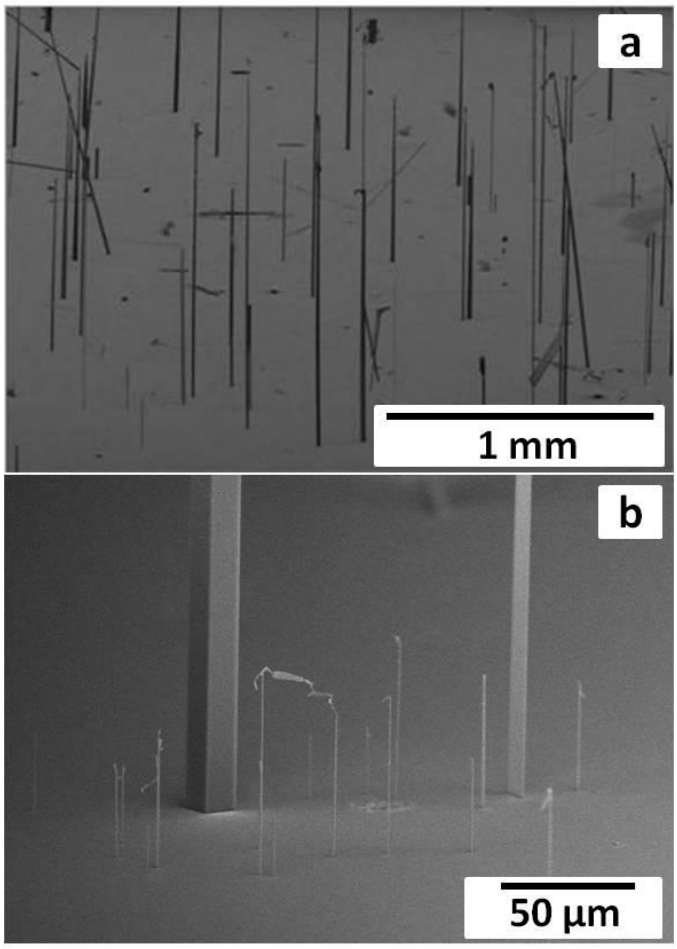

Figure 3.4 SEM images of specimens grown from 2.9wt% KCl solutions on 22nm silica particle porous coating at 75% RH.

Whiskers were also grown on 150 nm aggregates and 200 nm particle coating at 83%RH. At this relative humidity, there was no observable whisker growth occurred on 150nm aggregates coating, but long and curved whiskers were grown on 200 nm particle coating as shown in Figure 3.5. The whisker density was much lower than that of standard whisker growth condition (80%RH) but whisker lateral dimension remained similar.

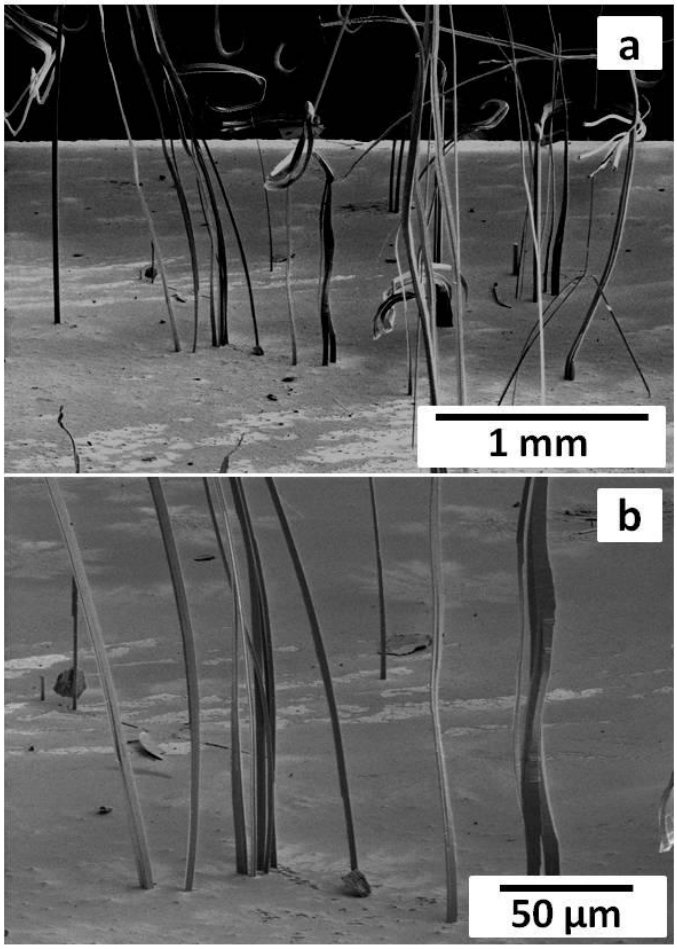

Figure 3.5 SEM images of specimens grown from KCl solutions on 200nm silica particle porous coating at 83%RH.

For 22 nm particle coating, there was no observable whisker growth at 80%RH. To enhance whisker growth, the relative humidity was decreased to 75%RH to raise driving force for water evaporation. For easy comparison, whiskers were also grown on a 150 nm aggregates coating at 75%RH as shown in Figure 3.2. Compared to 150 nm aggregates coating, whiskers grown on 22 nm particle coating had lower density and less quantity, and the whiskers were shorter and straighter. The whisker growth zone for 22 nm particle coating located higher than that for 150 nm aggregates coating.

3.2.3 Discussion

The coating thicknesses differ a lot for coatings made of different particle sizes. The large thickness differences between small (22 & 150 nm) and large particle (200 & 1000 nm) coatings were caused by the different dip coating withdrawal speeds. For particles with large diameter, sedimentation of silica particles occurred during dip coating process. Same withdrawal speed usually resulted in monolayer or discontinuous coating. Therefore, to ensure continuous coating with decent particle layers, a higher withdrawal speed was used.

The coating thicknesses for 22nm and 150nm agglomerate particle were slightly different. Although the withdrawal speed and the particle concentration were the same, the 150 nm agglomerate particles were packed more loosely than 22nm particles and this caused a thicker coating for 150nm aggregates.

The morphology of the whiskers grown on large particle coatings (1 μm and 200 nm) was quite different from small particle coating (150 nm aggregates and 22 nm). Coating thickness difference might not be the reason for the morphology difference, because coating thickness difference only affected the quantity of the whiskers as discussed earlier in coating thickness effect section. Therefore the coating particle size might cause the difference. There are two factors connecting whisker growth with coating particle size. The 1st factor is meniscus curvature and the 2nd factor is whisker supporting. As discussed in transport phenomenon (See Section 2.2.3.1), based on Kelvin equation, the evaporation flux is inversely related to the radius of the liquid meniscus formed in the porous coating. Assuming the meniscus radius is equal to the radius of the

particle, for meniscus radius of 1 μm, the equilibrium saturated water pressure over the meniscus is almost the same as that for flat surface. While for meniscus radius of 22 nm, the value is ~95% of the flat surface. Although the decrease of equilibrium pressure is only 5%, it actually results in a large change in driving force for water evaporation. For example, under standard whisker growth condition, the relative humidity is maintained at 80%RH and the equilibrium vapor pressure over a saturated KCl solution at 25 ℃ is 84.34% of that over pure water. As discussed in section 2.2.3.1, the water evaporation flux J_E is proportional to ($P^* - P^\infty$). Therefore the driving force for water evaporation over 1 μm particle coating is 4.34%P_{sat}. While for 22nm particle coating, the driving force is only 0.12% and it is calculated as

$$Driving\ Force = 84.34 \times 95\% - 80\% = 0.12\% \qquad 3.1$$

The calculation shows that the water evaporation driving force is 35 times larger for coating with 1 μm particle than that of 22 nm particle. Because the capillary driven flow is balanced with the water evaporation, rapid water evaporation increases the capillary driven flow and hence more salt ions are transported to the growth zone within fixed growth time. Therefore, larger amount of whisker or bulk salt crystal could be observed on coating made of larger particle size (200 nm &1 μm). For coating with 1 μm particle, the rapid water evaporation over the meniscus built up the salt concentration fast enough to reach high supersaturation ratio and initiate equiaxed crystal growth. A high percentage of equiaxed crystal was thus formed.

Based on same reasoning, rapid water evaporation occurred on 200 nm particle coating because of flatter meniscus, and hence the whisker quantity was much higher at 80%RH compared with that of 150 nm aggregates coating. However, if the relative humidity increased to 83%RH, the density of whisker is much lower as shown in Figure 3.5. This is because the driving force for water evaporation was reduced substantially at 83%RH compared with 80%RH.

The varied meniscus radius formed on coatings with different particle size caused the differences of whisker quantity. However, the lateral dimension difference could not be explained by the same logic. The 2nd factor, whisker supporting, influenced the whisker lateral size.

Figure 3.6 shows the schematic drawing of whisker supported on the porous coating with different particle sizes. The whisker needs a minimum number of particles to maintain balance on its base and gain liquid supply from the pores below its root for continuous growth. Although the critical particle number may be different, the whisker width tends to be larger on bigger particle coating in order to cover a sufficient number of coating particles. Therefore the whisker lateral size on 200 nm particle coating is larger than that of 150 nm and 22 nm particle coating.

As mentioned before, 150 nm aggregates is actually an aggregates of 20 nm particles. Because its individual particle size is about the same as 22 nm particle, the average whisker lateral dimension is also similar. However, compared with 22 nm particle coating, the surface roughness for coating with 150 nm aggregates is higher than that of 22 nm particle. Because the surface of 22 nm particle coating is smoother, it

provides better support for the thin whiskers (~2 μm), which were more frequently observed on 22 nm particle coating.

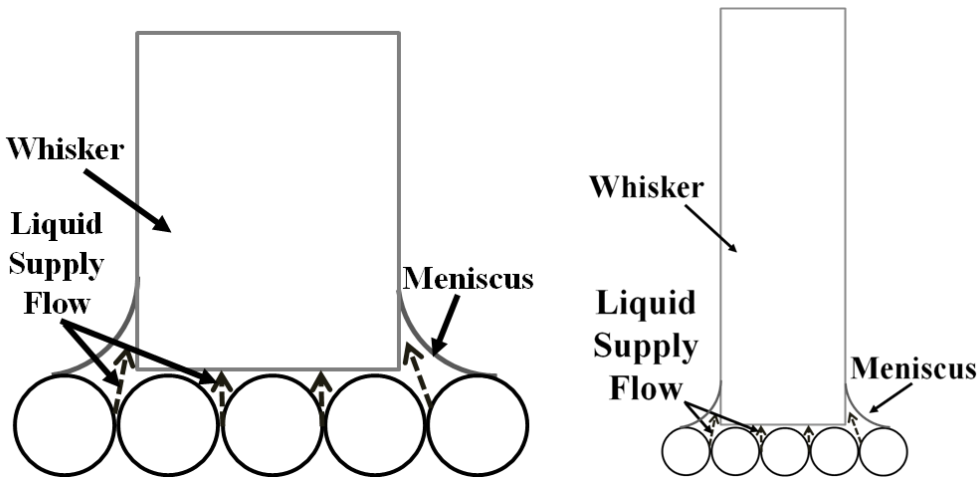

Figure 3.6 Schematic drawing of whisker sits on porous coating with large and small particle size.

3.3 Effect of Growth Angle on Whisker Growth

3.3.1 Experiment

The whisker growth angle is defined as the angle between the backside (uncoated side) of the glass substrate and the liquid surface (horizontal level) as shown in the Figure 3.7. The whisker growth angle was varied from 30° to 180° to investigate whether growth angle affects the whisker growth. To achieve 180° whisker growth angle, two coated glass slides were glued to each other in right angle. When one glass substrate was inserted into the salt solution, the other glass substrate was positioned at horizontal level and the nanoparticle coated side faced downward. The whisker growth condition remained the same as the standard growth condition. (150 nm aggregates porous coating, KCl: 2.9 wt%; relative humidity: 80%; growth time: 2 days)

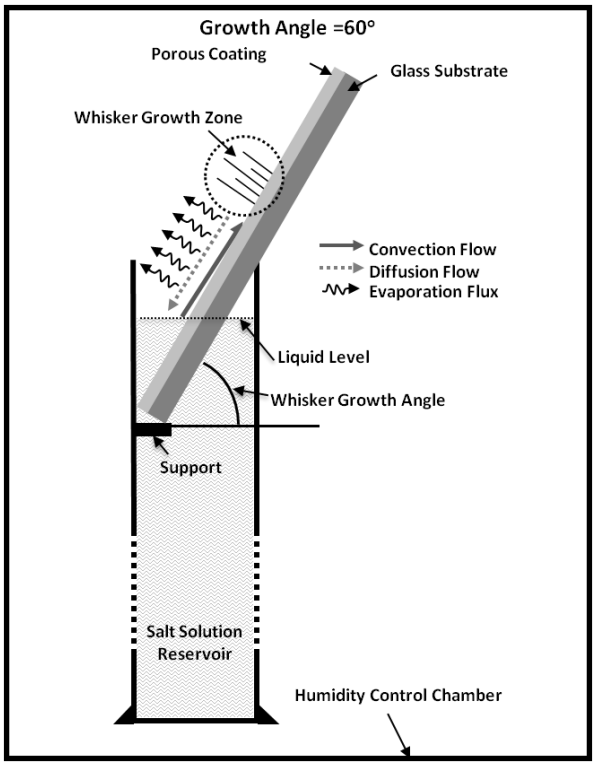

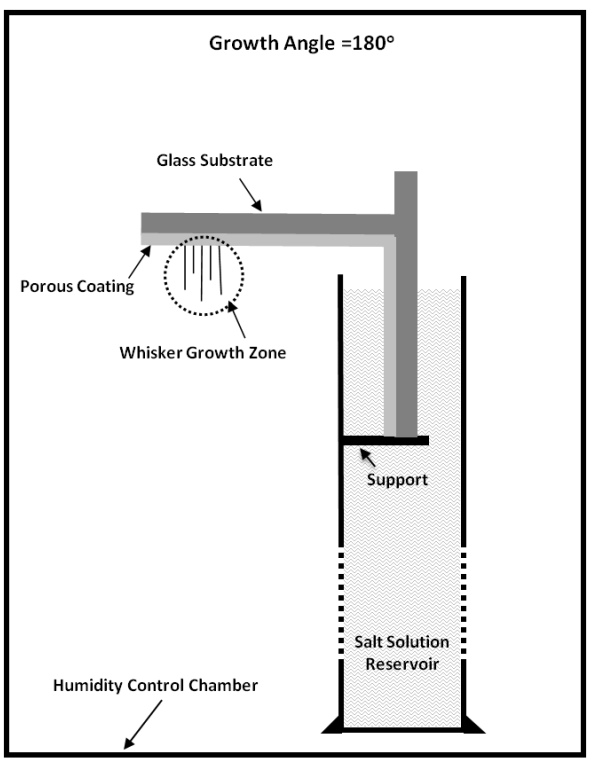

Figure 3.7 Experimental setup for whisker growth at varying growth angle. above: growth angle is 60° and below: growth angle is 180°.

3.3.2 Results

The results showed that whiskers could grow at any growth angle from 30° to 180° and almost all whiskers stood perpendicular to the glass substrate. The whiskers grown with some growth angles were shown in Figure 3.8. Whiskers were straight and with similar lateral dimension. However, the quantity of both standing and falling whiskers grown at 90° seemed to be larger than that of other growth angles.

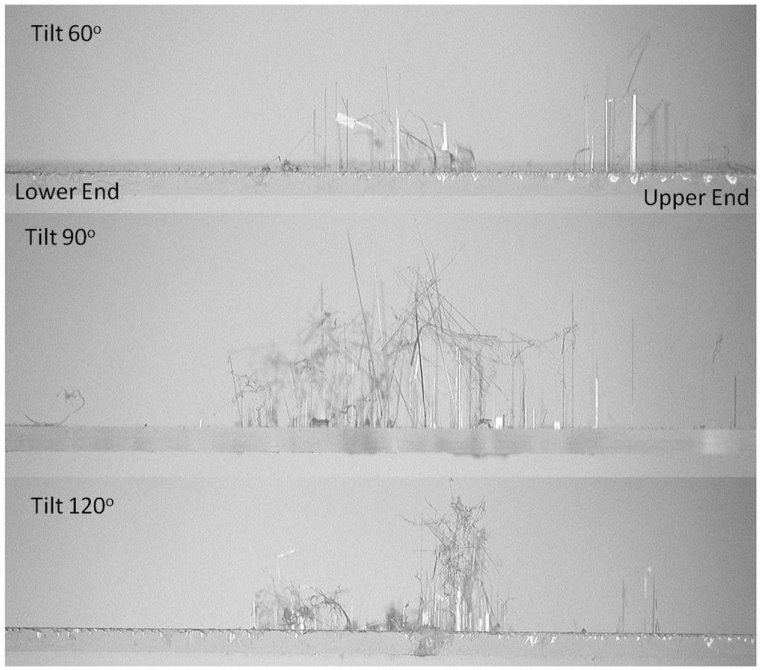

Figure 3.8 Whisker growth on porous coating with different growth angle under standard whisker growth condition.

Figure 3.9 shows the SEM image of salt crystal formed at the root of the whisker after drying a specimen grown under standard condition. A thin salt crystal was frequently observed around the base of the whisker (a, c) and on the side wall of the

whisker near the base (b). Sometimes, instead of a thin crystal layer, relatively larger equiaxed salt crystal grew round the whisker base to form a ring (b).

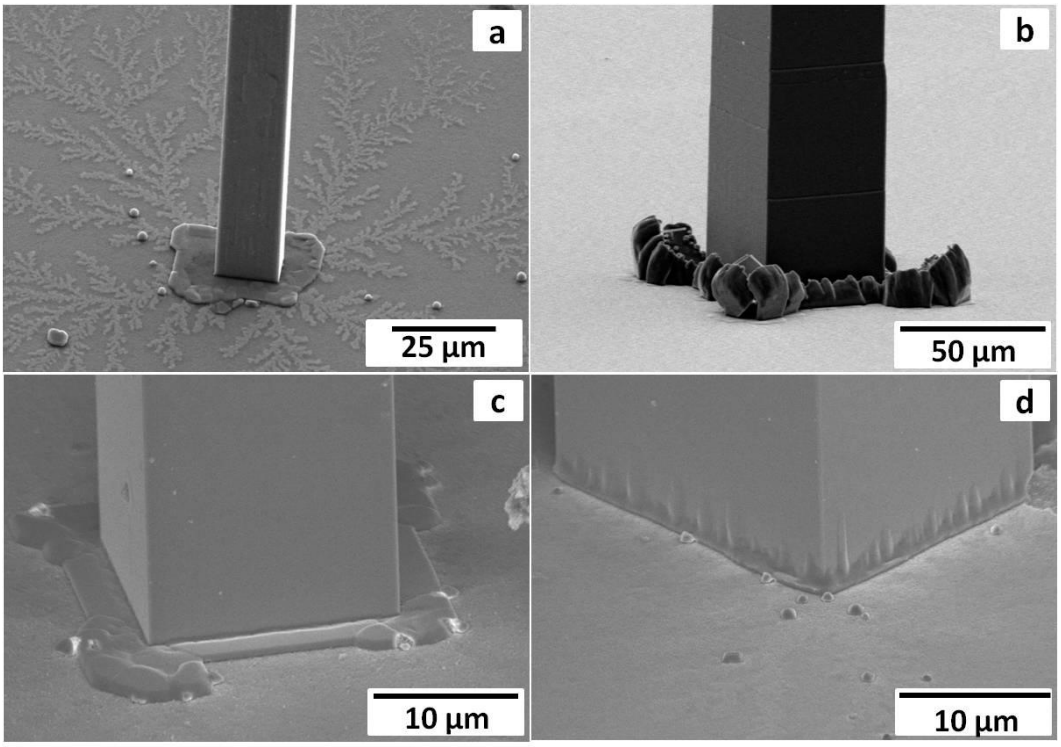

Figure 3.9 SEM image of salt crystal at the base of the whisker with growth angle at 60° (a,b) and 90° (c,d).

3.3.3 Discussion

It is quite amazing that no matter what the growth angle is, the whiskers could maintain their balance and stand perpendicular to the porous coating. It is important to understand what actually keeps the whisker standing.

Based on the discussion of whisker growth mechanism (section 2.2.3.2), the whisker grows by liquid supply from its base. Although it is difficult to experimentally

observe the liquid layer directly, possible liquid layer residues were frequently observed to form around the whisker base after sample dries, as shown in Figure 3.9. Therefore it is reasonable to assume there was a liquid layer around the whisker base during growth. The liquid layer acts both as a source of salt ions and as a stability force to keep the whisker standing in balance. Quere et showed in their paper [75] that when a fiber was inserted into a liquid reservoir, the liquid would climb up the fiber wall due to wetting and if the lateral dimension of the fiber is much less than the capillary length and assuming complete wetting, the equilibrium height h could be approximately calculated as

$$h \cong \frac{w}{2} \ln \left(\frac{4\sqrt{\frac{\gamma}{\rho g}}}{w}\right) \qquad 3.2$$

where γ is the surface tension of the liquid, ρ is the density of the liquid, and w is the width of the fiber.

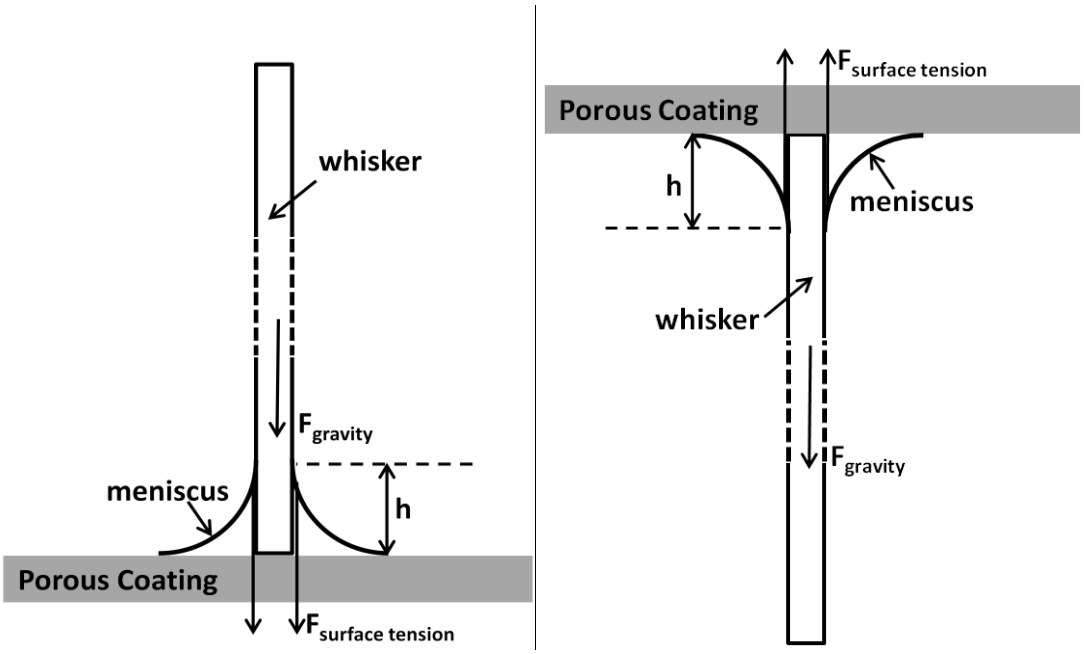

Figure 3.10 Schematic drawing of meniscus at the root of the whisker. (Left) growth angle is 0° and (right) growth angle is 180°

If we assume that equation 3.2 could be applied in our case and salt solution at the whisker base wets the whisker wall perfectly and thus forms a contact angle equaling to zero. When the glass substrate is positioned horizontally with the porous coating facing upward as shown in Figure 3.10 (whisker growth angle = 0°), based on equation 3.2, the meniscus height is about 2.5 times of the lateral dimension of the whisker. For a 10 μm whisker, the liquid height h would be ~25 μm.

Because the contact angle between the salt solution and the whisker wall is zero, when the whisker stands perpendicular to the porous coating during growth (growth angle=0°), the meniscus formed around the side wall of the whisker base would exert a downward force on whisker due to surface tension. This downward force together with the force of gravity is balanced by the force pushing upwards on the whisker base from

porous coating. As all the forces are perpendicular to the porous coating and there is no horizontal partial force, the whisker would remain in balance and stand normal to the porous coating.

While for whiskers with growth angle of 180° as shown in Figure 3.10, the force of gravity and the force of surface tension are in opposite direction. The gravity force is the weight of the whisker and the force of surface tension is calculated as

$$F_{surface\ Tension} = \gamma c \qquad 3.3$$

where γ is the surface tension of the solution and c is the perimeter of the whisker's rectangular cross section. Assuming the aspect ratio (length/width) of whisker is 100 and the solution surface tension equals to that of pure water, the ratio of surface tension force to gravity force (whisker weight) is shown in Table 3.2. The results indicate that the surface tension force is large enough to pull the whisker toward the porous coating against the gravity unless the whisker is extreme long and thick.

Table 3.2 Ratio of surface tension force to gravity force (whisker weight). Assuming whisker aspect ratio is 100.

Whisker Width	$F_{surface\ tension}/F_{gravity}$
100nm	1.48E+07
1µm	1.48E+05
10µm	1.48E+03
100µm	1.48E+01

However, during growth, disturbances such as circulating air flow in the humidity control chamber and vibration from various sources always exist. These disturbances would temporary break the force balance and cause the whisker to tilt as shown in Figure 3.11. This schematic drawing shows that a whisker temporary tilts towards its right side due to disturbance. Under this unbalanced state, gravity would drag the whisker further right to fall down onto the porous coating, while the force from the left side meniscus tends to pull the whisker back towards the left and restore the balance.

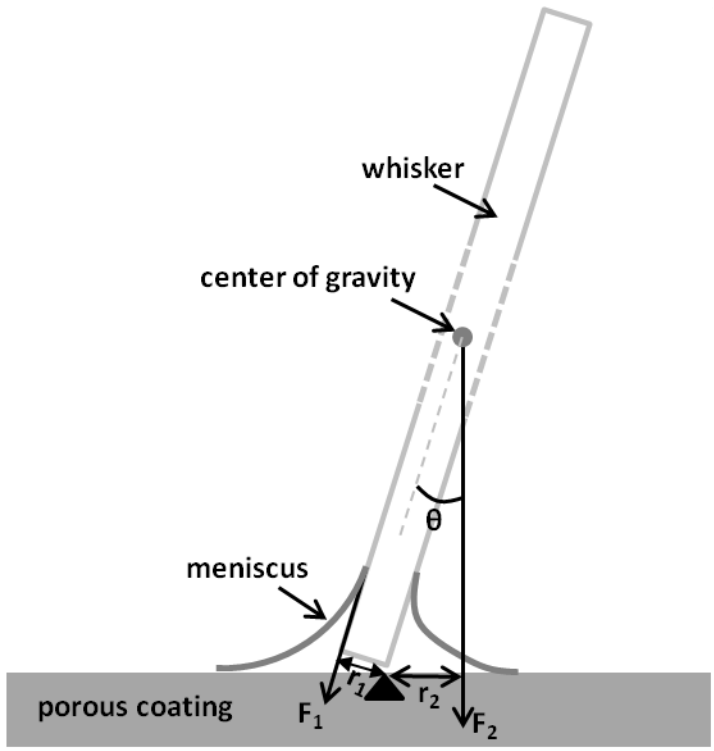

Figure 3.11 Schematic drawing of torque balance when whisker tilts.

Instead of force balance, torque balance needs to be calculated in this case. Because the force of gravity drives the whisker to fall, it is called τ_{fall} and it is calculated as

$$\tau_{fall} = F_2 \times r_2 \quad 3.4$$

where F_2 is the gravity force of the whisker (whisker weight) and r_2 is the length of the lever arm.

The support torque comes from the meniscus formed on the left, front and back sides of the whisker walls. Because the support torque from the front and back sides was a function of the tilt angle, to simplify the analysis, only the supporting torque from the left side was calculated to demonstrate the magnitude of the supporting torque compared to the fall torque and it is calculated as

$$\tau_{support} = F_1 \times r_1 = \gamma w \times r_1 \quad 3.5$$

where F_1 is the surface tension force exerted on whisker side walls and is calculated by timing surface tension γ and whisker width w; r_1 is the length of its lever arm. When whisker tilts, the dynamic contact angle between salt solution and whisker wall may not be zero, and it should depend on how fast the whisker falls. However, as the dynamic contact angle should not deviate too much from zero, it is still assumed to be zero in the calculation.

As the surface tension force vector from the meniscus on the right side of the whisker goes through the pivot point, its torque equals to zero and will not be included in the torque calculation.

When the whisker starts to tilt a little because of disturbance, the τ_{fall} would make the whisker to tilt more while the $\tau_{support}$ tends to pull the whisker back to its

perpendicular balanced state. If the $\tau_{support}$ is larger, the whisker would restore to its balance and continues to grow. However, if the τ_{fall} is larger, the whisker would fall down to the porous coating and stop growing; however, in some cases, the fallen whisker may acts as seed to initiate sheet growth as discussed before.

If the aspect ratio (length/width) of KCl whisker is assumed to be 100, the ratios of $\tau_{support}$ / τ_{fall} for whiskers with different widths and different tilt angles θ were shown in Table 3.3. The dependence of torque ratio on tilt angle for a 10 μm whisker with aspect ratio of 100 was plotted in Figure 3.12. The results show that for whisker with diameter of less than 10 μm, the $\tau_{support}$ is much larger than τ_{fall} at any tilt angle. However, if whisker width is larger than 100 μm, the τ_{fall} dominates. The results indicate that whiskers with small lateral dimension gain better resistance to temporary disturbances and are more stable during growth than whisker with large width. It also explains that most of the whiskers observed are thinner than 100μm.

Table 3.3 Ratio of $\tau_{support}$ / τ_{fall} at different tilt angle θ for tilted whisker if whisker aspect ratio is 100.

Whisker Width/Tilt Angle	0°	15°	30°	45°	60°	75°	90°
100nm	1.18E+09	1.43E+05	7.41E+04	5.24E+04	4.28E+04	3.70E+04	3.70E+04
1μm	1.18E+07	1.43E+03	7.41E+02	5.24E+02	4.28E+02	3.70E+02	3.70E+02
10μm	1.18E+05	1.43E+01	7.41E+00	5.24E+00	4.28E+00	3.70E+00	3.70E+00
100μm	1.18E+03	1.43E-01	7.41E-02	5.24E-02	4.28E-02	3.70E-02	3.70E-02

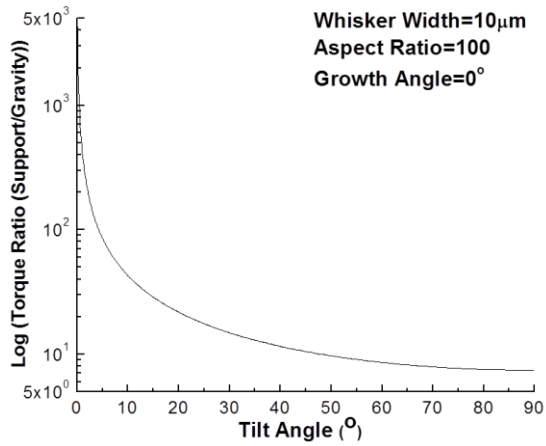

Figure 3.12 Plot of dependence of ratio of $\tau_{support}$ / τ_{fall} on tilt angles for a 10 μm whisker with aspect ratio of 100.

If the whisker aspect ratio increases to 1000, the calculated ratio of $\tau_{support}$ to τ_{fall} is shown in Table 3.4. All the ratios decrease by 100 times and it agrees with the intuitive conclusion that long whisker will fall more easily.

Table 3.4 Ratio of $\tau_{support}$ to τ_{fall} at different tilt angle θ for tilted whisker if whisker aspect ratio is 1000.

Whisker Width/Tilt Angle	0°	15°	30°	45°	60°	75°	90°
100nm	1.18E+07	1.43E+03	7.41E+02	5.24E+02	4.28E+02	3.70E+02	3.70E+02
1μm	1.18E+05	1.43E+01	7.41E+00	5.24E+00	4.28E+00	3.70E+00	3.70E+00
10μm	1.18E+03	1.43E-01	7.41E-02	5.24E-02	4.28E-02	3.70E-02	3.70E-02
100μm	1.18E+01	1.43E-03	7.41E-04	5.24E-04	4.28E-04	3.70E-04	3.70E-04

The $\tau_{support}/\tau_{fall}$ ratio is also calculated for whisker with growth angle of 90° (the porous coating surface is perpendicular to floor and the whisker is parallel to the floor). The result is shown in Table 3.5. It proves that the torque from the liquid layer at whisker

base is sufficient to support the whisker to stand vertically on the porous coating during growth even through the substrate surface is in perpendicular position.

Table 3.5 Ratio of $\tau_{support}$ to τ_{fall} at different tilt angle θ for tilted whisker if whisker aspect ratio is 100 and whisker growth angle is 90°.

Whisker Width/Tilt Angle	0°	15°	30°	45°	60°	75°	90°
100nm	3.74E+04	3.83E+04	4.28E+04	5.23E+04	7.40E+04	1.43E+05	4.65E+07
1µm	3.74E+02	3.83E+02	4.28E+02	5.23E+02	7.40E+02	1.43E+03	4.65E+05
10µm	3.74E+00	3.83E+00	4.28E+00	5.23E+00	7.40E+00	1.43E+01	4.65E+03
100µm	3.74E-02	3.83E-02	4.28E-02	5.23E-02	7.40E-02	1.43E-01	4.65E+01

In conclusion, the whisker could grow on porous coating at any growth angle, and a liquid layer is proposed to adhere around whisker base during its growth to provide both salt supply and stability support.

3.4 Cryo SEM study of liquid supporting layer

3.4.1 Experimental

Silicon wafer (5 mm x 15 mm) was used as substrate for dip coating. The dip coating process remained the same and the porous coating was made of 150 nm aggregates particles. The porous coating on the edges of the silicon wafer was not removed as in standard whisker growth procedure. One drop of seed solution was applied onto the surface of the porous coating on the edge face of the silicon wafer. (detail about seeding technique will be covered in Chapter 4)

The coated silicon sample was mounted on a specially designed sample carrier with top surface of porous coating facing up. The sample carrier was screwed onto a cryo-transfer rod (Emitech, Kent, UK). 30 µl of KCl solution (2.9 wt%) was then dropped onto the top surface of the coated silicon sample. A schematic drawing of coated silicon wafer with liquid drop on the top surface is shown in Figure 3.13. The salt solution was then wicked through the porous coating to the edge surfaces of silicon wafer to initiate whisker growth there. The sample was then left untouched to allow whisker growth. The growth time varied from 1 to 30 minutes for different samples. The relative humidity was not controlled and the surrounding relative humidity in the room was about 50%. In one sample, pure distilled water was used to replace salt solution for comparison.

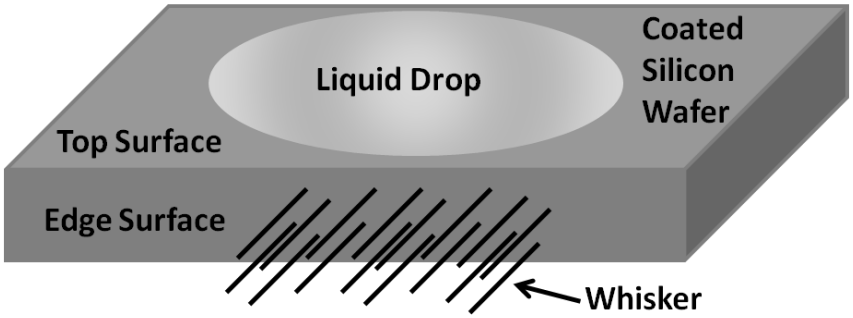

Figure 3.13 Schematic drawing of coated silicon wafer with liquid drop dispensed on top surface porous coating and the whiskers grown on the edge surface.

After growth, the sample was held above a liquid nitrogen bath with sample carrier barely touching surface of the liquid nitrogen. After about 1 minute, the salt solution drop on the coating surface turned from transparent to opaque, which indicated solution was frozen and cracks also formed inside the ice. The Cryo transfer unit was immediately inserted into an Emitech K-1250 preparation chamber (Emitech, Kent, UK) for conductive metal coating. The sample was maintained below 130°C and a thin platinum layer about 5 nm thick was sputter coated onto the sample surface.

The platinum coated sample was then transferred to a Hitachi S-4700 scanning electron microscope (Hitachi, Pleasanton, CA) for examination. The sample was kept around -150°C by a liquid nitrogen cooled stage during imaging.

3.4.2 Results

The Cryo-SEM images of morphology of pure water and salt solution after freezing with the liquid nitrogen vapor method were shown in Figure 3.14. The ice from

pure water showed a relatively smooth surface. Pure ice seemed to crystallize during freezing, and the crystal grains and grain boundaries could be observed on the surface. Some fiber like structures were also present on the surface of the ice and it might be impurities in the water that was segregated to the boundaries during ice crystallization and formed these one dimensional structures. While for KCl salt solution, after frozen, layered structures with empty space in between were formed as shown in Figure 3.14b.

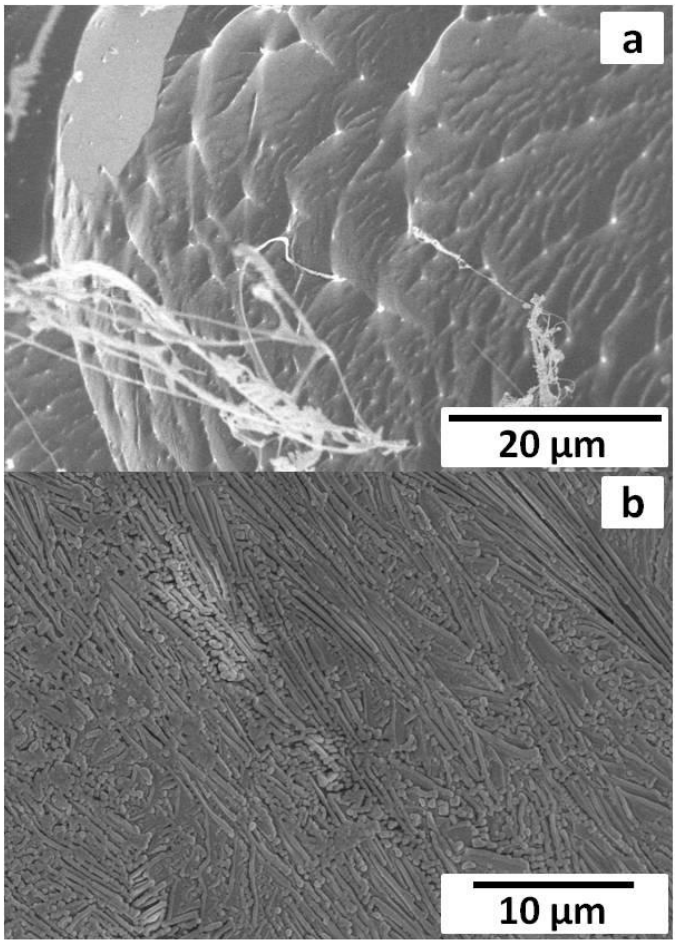

Figure 3.14 Cryo-SEM images of surface morphology of pure water (a) and KCl salt solution 2.9wt% (b) after freezing with liquid nitrogen.

Figure 3.15 showed cryo SEM images of both the top and edge surfaces of the silicon wafer. A thick ice layer could be observed on the top surface, while on the edge surface, no similar ice structure was present. Whisker-like salt crystals were grown on the edge surface and these salt crystals extended from the near end to the far end of the edge face. A convex stripe structure seemed to connect the near end of the edge face to the base of the closest whisker like crystal is shown in Figure 3.15a and a similar convex stripe is shown in Figure 3.15b. In Figure 3.15b, the whisker-like structure is titled and only a small portion of the crystal base is attached to this convex structure. (detail of the tilted structure has been discussed in Chapter 2.) A high magnification image of crystal base and the convex structure is shown in Figure 3.15c.

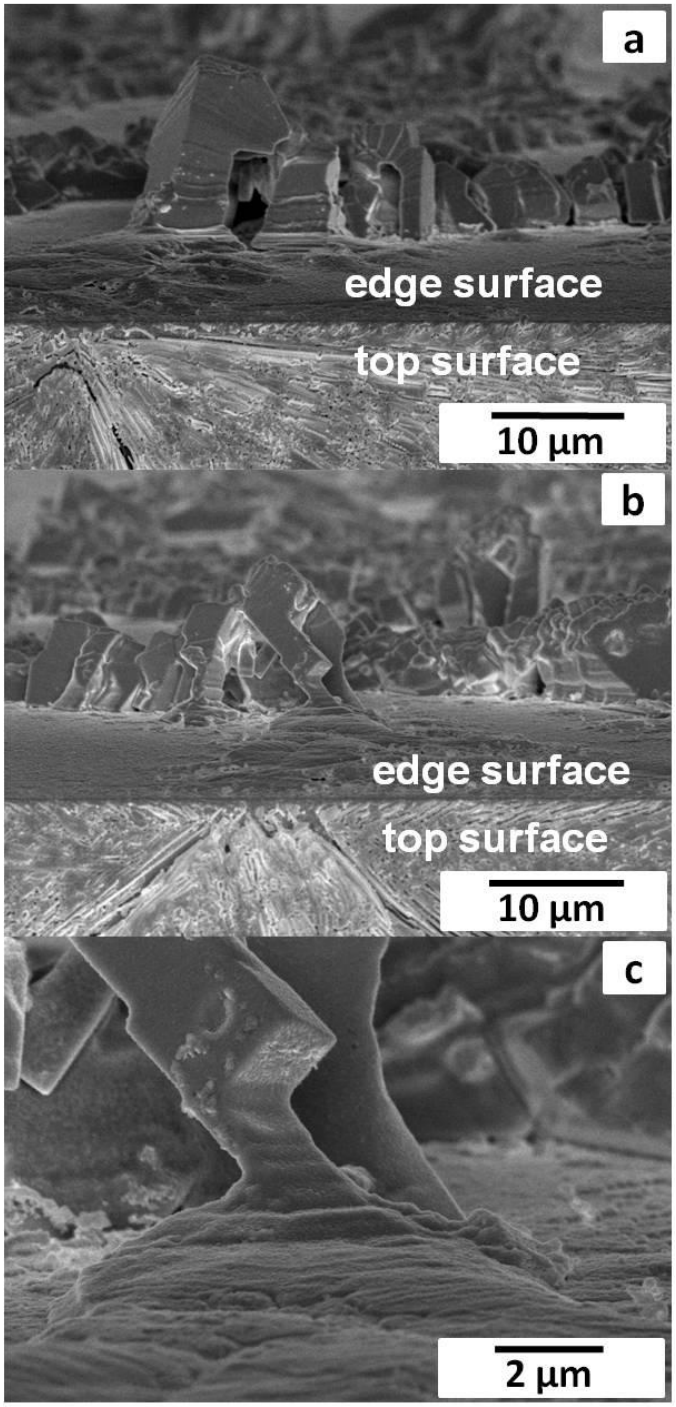

Figure 3.15 Cryo-SEM images of whisker-like salt crystal growth on the porous coating of edge surface of the silicon wafer (a,b). High magnification image of a tilted whisker-like crystal base. (150 nm aggregates particle, KCl 2.9wt%, growth time: 20 mins, ~50%RH)

With proper growth time (10 minutes), salt crystal whiskers could be observed in the middle area of the edge surface as shown in Figure 3.16a. A corrugated solid layer usually covered the porous coating surface around the whisker growth zone. A hunched solid structure was frequently observed around the whisker base and the high magnification images of such structures are shown in Figure 3.16b-d. Another feature worth noticing was that a layer of evenly distributed dots covered the whole surface of whisker side wall and these dots also existed on the surface of the corrugated layer. However, these layers of dots had never been observed in SEM images taken at room temperature.

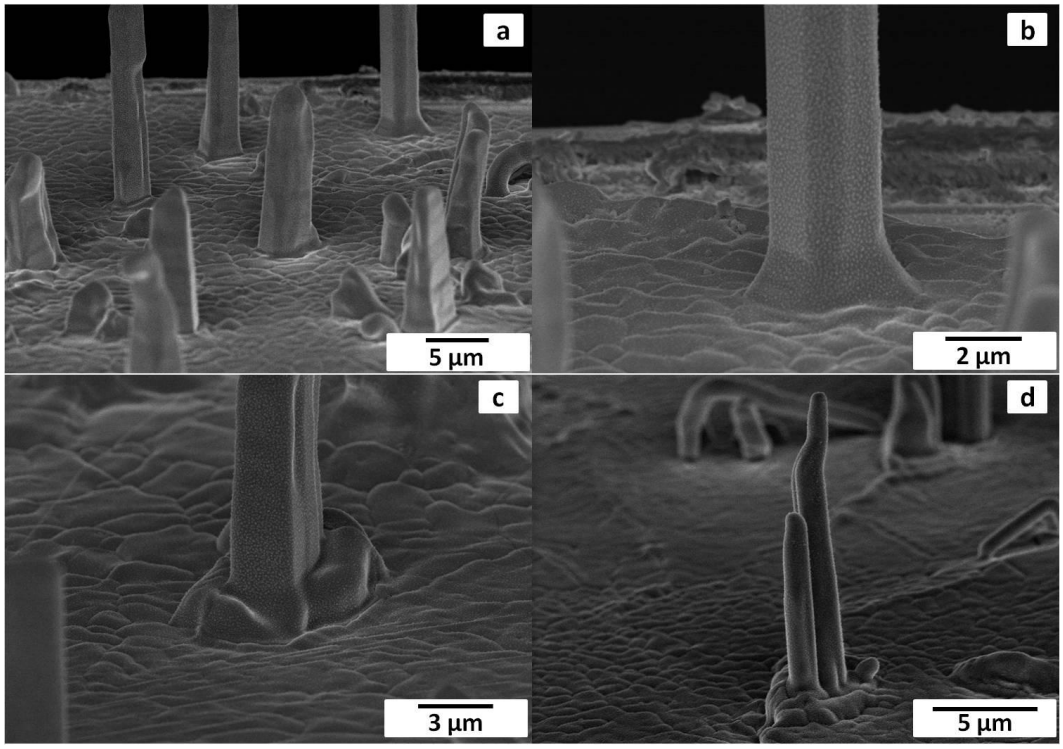

Figure 3.16 Cryo-SEM images of salt whisker growth on the porous coating of edge surface of the silicon wafer. (150 nm aggregates particle, KCl 2.9wt%, growth time: 10 mins, ~50%RH)

With relatively longer growth time, whisker and whisker-like crystals were present in some areas on the edge surface. However, there was no corrugated layer covering the porous coating in this case and the porous coating surface was smoother. The dots layer could still be observed to cover the whole sample surface.

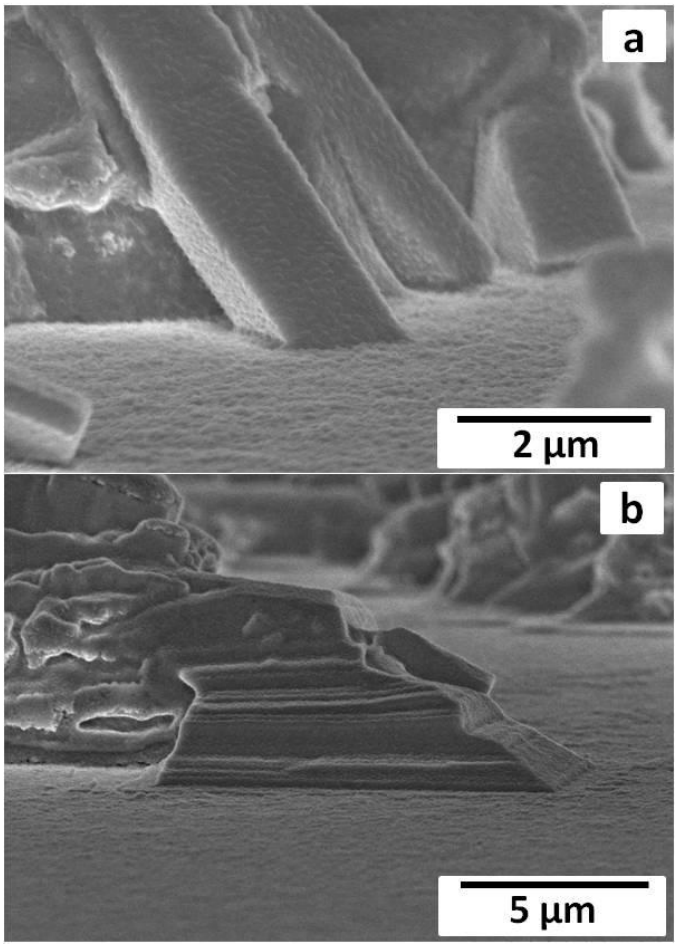

Figure 3.17 Cryo-SEM images of salt whisker growth on the porous coating of edge surface of the silicon wafer. (150 nm aggregates particle, KCl 2.9wt%, growth time: 20 mins, ~50%RH)

3.4.3 Discussion

In section 3.3, a liquid support layer at the whisker base was proposed to keep the stability of whisker during growth. Theoretical calculation suggested that the support torque was large enough for this liquid layer to keep whisker standing. However, besides the salt crystal residues around the whisker base, there is no direct evidence to prove the existence of this supporting liquid layer.

Cryo scanning electron microscope is a technique that freezes the wet sample rapidly to preserve the hydrated vulnerable structures, such as cells. The cooling processes generally used include plunging the specimen into nitrogen slush, or liquid nitrogen cooled ethane bath, or by high pressure liquid nitrogen freezing to achieve large enough cooling rate to prevent crystallization of ice and obtain ice in amorphous state. This technique in principle should be able to be applied to our sample so that the growing whisker could be frozen rapidly and thus whether the supporting liquid layer existed at the whisker base could be revealed. However, unlike conventional cryo SEM specimen, our experiment faces two difficulties because of the special requirements. Firstly, traditional cryo SEM cooling method might not work for our sample as the growing whiskers could not survive the plunging. As discussed in Chapter 2, vibration causes the whisker to tilt or fall. The alternate freezing method we used was to freeze the sample by liquid nitrogen vapor, which might be able to preserve the delicate whisker during growth. However, vapor freezing significantly reduce the cooling rate and thus crystallization of ice was unavoidable as shown in Figure 3.14a. Actually salt solution

made the situation more complicated. During cooling process, salt segregated from water and a layered structure was formed. See Figure 3.14b.

Secondly, our sample needed imaging of the outer surface of the whisker instead of the cross section of the specimen and this meant that surrounding water vapor might condense onto the whole sample surface and thus made it difficult to determine whether the liquid layer was from sample or from environment.

High magnification images in Figure 3.16and Figure 3.17show that a layer of evenly distributed dots covered the side walls of all the whiskers. These dots had never been observed in room temperature SEM images and it indicated that these dots might be the ice particles formed by condensation of environmental water vapor during freezing process. If observed carefully, these dots structures actually existed everywhere on the surface of the specimen including the rough corrugated layer in Figure 3.16 and the relative smooth porous coating surface in Figure 3.17. If we assumed that, during freezing, the rates of water vapor condensation onto sample surface were similar over the whole sample, it could be concluded that the convex stripe in Figure 3.15 and the corrugated structure in Figure 3.16 was not formed by water vapor condensation from environment during sample freezing.

For the convex stripes that bridged between salt solution drop on the top surface and the whisker on the edge surface, a reasonable explanation was that the salt solution was drawn specifically to the whisker base due to high water evaporation rate and relatively lower pressure at whisker base. (detail about liquid drawn to the whisker base

will be discussed in Chapter 4) Therefore, the convex stripe might be the frozen salt solution.

For the corrugated structure covering the porous coating surface and the hunched structure around the whisker base in Figure 3.16, these structures were frequently observed on specimen with short growth time but not on specimen with relatively long growth time as shown in Figure 3.17. This indicated that these structures might be the frozen liquid layer that existed around the whisker base during growth and covered the nearby porous coating.

However, a question raised immediately was why the morphology of the stripe and corrugated structure was so different from the frozen salt solution shown in Figure 3.14b. The different look might result from the thickness differences. For salt solution on the top surface, the thickness of the liquid should be at least hundred micrometers before freezing, while the thicknesses of stripe and corrugated structure on the edge face were much smaller. The smaller thickness might result in much higher cooling rate for the salt solution layer on the edge surface and hence caused different morphologies.

Another possibility was that these structures were KCl salt crystal. During freezing process, water might dry out and leave behind only salt crystals. If this was the case, the salt solution concentration of the liquid layer must be much higher than the initial salt concentration (2.9 wt%) or the liquid layer would be thick enough to cover the whole whisker to leave such a salt crystal layer.

However, at this point, it is difficult to conclude what exactly these structures were and further experiments are needed to solve this problem.

In conclusion, growing whiskers were frozen by liquid nitrogen vapor method and Cryo-SEM images provided some evidences of the existence of supporting liquid layer around the whisker base. However, because of the limitation on experiment design, some key parameters about the support liquid layer such as its interface with whisker side wall and its thickness still could not be determined and require further investigation.

3.5 Whisker Growth by Free Particle Method

3.5.1 Experimental

Whiskers were also grown on bare glass substrates from salt solutions that contained silica nanoparticles. A 2.9 wt% KCl solution was modified by the addition of Cabot PG022 dispersion such that the quantity of silica was approximately 0.00025 wt%. The growth was carried out in the same way as described for the coated substrate in Chapter 2. The relative humidity was 70% and the growth time was two days.

3.5.2 Results

This method involved placing a bare glass substrate into KCl solution that contained free silica particles and then waiting for two days. Approximately two hours after the glass slide is immersed, the leading edge, the contact line, turned white first and then whiskers appeared in this region quickly. Unlike growth on porous coatings, whiskers appear right beneath the original liquid level and form a substantial mass, as shown in Figure 3.18.

Section 3.5 is adapted from paper "Formation of Salt Crystal Whiskers on Porous Nanoparticle Coatings" published in Langmuir 26, 2847, 2010. by Heng Zhang H, Zhen Wu and Lorraine F. Francis.

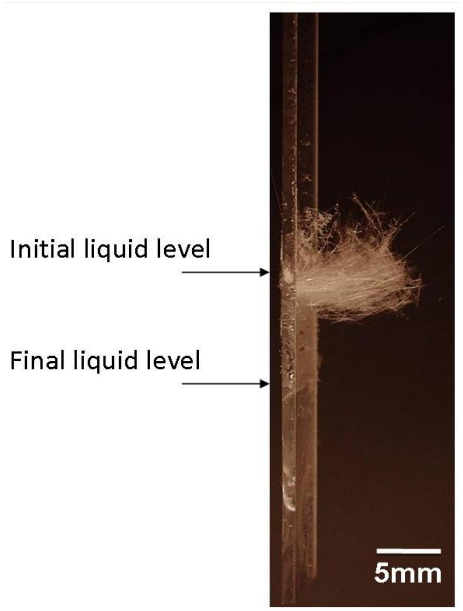

Figure 3.18 Digital image of specimen after free particle whisker growth. Growth occurred for two days at 70% relative humidity using a 0.03 g/ml KCl solution that contained 0.00025 wt% silica particles (150 nm aggregates).

This growth mode required the relative humidity to be below 75%. No whiskers appeared at higher relative humidity. The small concentration of silica particles in the growth solution was essential to the formation of whiskers. Without the silica particles, a non-whisker crust formed on the glass slide in the course of two days.

Figure 3.19 shows SEM images of the whisker growth zone of a specimen formed using free particle growth conditions. The whiskers have a similar morphology to those grown on porous coatings. However, more whiskers form by this growth mode at same relative humidity and salt concentration. Some curved whiskers and sheet morphologies are also found. A coating of silica particles is formed coincident with the formation of whiskers and the coating thickness is ~2 μm. After drying, this coating is cracked and peeling, as shown in Figure 3.19b.

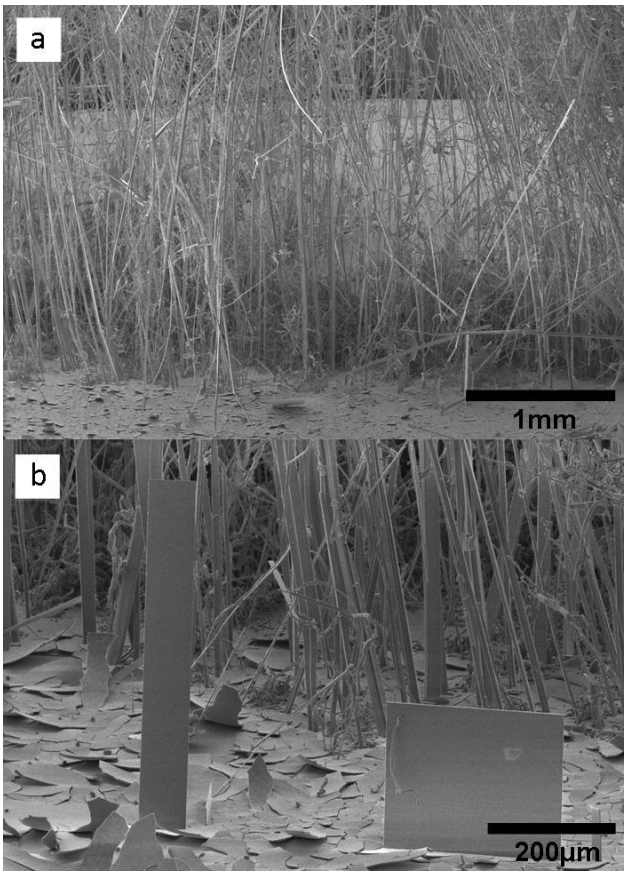

Figure 3.19 SEM of whiskers grown on bare substrates by the free particle method. Growth occurred for two days at 70% relative humidity using a 2.9 wt% KCl solution that contained 0.00025 wt% silica particles (150 nm aggregates).

3.5.3 Discussion

The whisker growth zone for the free particle case is also a consequence of capillary driven flow, evaporation, and diffusion. The results show that when a small quantity of silica particles was added to the salt solution, whiskers grew on bare glass substrates. This situation is more complex than the standard whisker growth; one hypothesis is presented here. In a manner similar to convective assembly of colloidal crystals[57], free particles are pulled up to the contact line where the liquid wets the

substrate, and they deposit there to form a coating as evaporation proceeds and the liquid level drops. The thickness of the self assembly coating is ~2 μm, which is much larger than that of the dip coated specimen. Because the coating thickness is above the critical thickness, after drying, cracks and peeling off occurred to release the stored stress. Evaporation also increases the salt concentration in the pore fluid, and it apparently does so very effectively, perhaps due to the adjacent supply in the bulk liquid, because whiskers begin to form quickly at the initial point of contact. Whiskers continue to grow as the liquid level drops and more particles assemble into a coating.

Chapter 4 Whisker Size Control

4.1 Introduction

After studying the effect of experimental variables on whisker growth and understanding the whisker growth mechanism, the next step to achieve the objective of the research is to investigate whether the size of the whisker could be reduced to nanometer scale.

Law and coworkers[76] summarized strategies for synthesizing one dimensional nanostructure in this review paper. The mechanisms for promoting crystallization along one dimension include: (1) the crystal has an intrinsically anisotropic crystal structure; (2) template with one dimensional structure is used to limit the crystal growth in one dimensional channel; (3) in vapor phase synthesis, catalyst particles are utilized to create liquid/solid interface to reduce the symmetry of a seed; (4) In solution synthesis, capping agent is used to adsorb preferentially to certain facet of the seed to change crystal growth rates on different crystallographic planes. (5) Self assembly of nano-particles.

In our case, none of the above mechanisms could be used to explain clearly how one dimensional whisker could be formed on the nanoporous coating. However, the general idea remains the same: to enhance the growth rate in the long axis of the nanowire and at the same time to reduce or stop the crystal growth in the short axis.

As confirmed by X-ray platform diffractometer, the bounding surfaces of the whisker belong to the same {100} family of planes, and this eliminates the possibility of forming one dimensional structure by intrinsically anisotropic crystal. However, the

presence of asymmetry growth rate on whisker base face and side wall is still necessary to satisfy the growth condition for one dimensional crystal structure.

As discussed earlier, there are several possible reasons for the preferential crystal growth on the whisker face in contact with the porous coating. The most likely one is that the supply of salt solution is abundant at the base as compared with whisker side walls. Although there is liquid layer adhering to the side wall around the whisker base, the rising height of the liquid meniscus on whisker side wall should be on the same order of the whisker width. During whisker growth, the whisker is pushed up continuously and the time that each portion of the side wall in contact with the liquid layer is very short so that crystal growth on side wall is limited. Furthermore, the rough surface of the porous coating leads to the possibility that the whisker base surface in contact with the coating is defective, and the presence of more steps and kinks at the base face would further enhance its growth rate.

Another possibility is that a dislocation or other defect mechanism is at play. The literature is mixed on the role of defects and dislocations on whisker growth from solution. Shichiri[34,71,77] studied dissolution behavior of whiskers and noted that they appear to be defect-free, while Amelinckx[78] documented dislocations in whiskers by a decoration method. Multiple attempts including decoration method and saturation solution re-growth method has been tried to locate dislocations in our whiskers, but none were found. Some research on tabular shaped alkali halides[73] suggests that stacking faults may also lead to rapid and preferred directions of crystal growth. (The above paragraph is adapted from paper “Formation of Salt Crystal Whiskers on Porous

Nanoparticle Coatings" published in Langmuir 26, 2847, 2010. by Heng Zhang H, Zhen Wu and Lorraine F. Francis.)

In this chapter, strategies to reduce the lateral dimensional of whisker to the nanometer scale will be discussed and these strategies include whisker growth on patterned porous coating, porous coating with small particle size and seeding whisker growth.

4.2 Experimental

4.2.1 Whisker Growth on Patterned Porous Coating

Patterned substrate preparation. A 4 inches silicon wafer with repeated hydrophilic and hydrophobic stripes was prepared based on the following procedures.[79]

a. Commercial available silicon substrate is cleaned by standard wafer cleaning procedure. Silicon wafer is immersed in Pirhana(5:1H_2SO_4 with H_2O_2) solution for 15 minutes at 120 ^oC, and the wafer is then rinsed with DI water and dried.

b. The wafer is prebaked at 115 ^oC for 1 minute.

c. Photoresist (Futrrex NRF-1500P) is spin coated (3000 RPM) on the silicon wafer for 30 seconds.

d. Softbake is carried out at 150 ^oC for 1.5 minute to drive off solvents and to improve adhesion.

e. A pre-designed mask is placed above the photoresist coated silicon substrate, and is exposed to UV light for 14 sec in ultraviolet exposing system (maba6).

f. The as exposed silicon substrate is post baked at 100 ^oC for 1.5 minute.

g. The silicon wafer is immersed in the developer solution (Futurex RD6) for 1 minute and is rinsed with DI water and dried.

h. The silicon wafer is sealed in a dessicater with 1ml OTS solution. The reaction of silicon with OTS vapor lasts for 12 hours.

i. The silicon wafer is washed in acetone and ethanol to remove the cured photoresist and is rinsed with DI water.

Dip coating. The as prepared patterned substrate was dip coated with colloidal suspension to create a patterned porous coating. (The hydrophilic stripes are coated while the hydrophobic stripes are not) Coating solution is Cabot PG002 (150 nm aggregates partilce) with 10 wt% solid contents and the withdrawal speed was 10 mm/sec.

Whisker growth. The patterned porous coating was used as substrate for whisker growth. The patterned strips were oriented perpendicular to the liquid level. The whisker growth procedure remained the same as the standard whisker growth. (KCl 2.9 wt%, 80%RH, 2 days)

4.2.2 Whisker Growth by Seeding.

Manually Ground Seed. One gram of potassium chloride (99.6%, Mallinckrodt) was manually crushed and ground in mortar with pestle for about 15 minutes. The ground KCl powder was then dispersed in isopropyl alcohol and was treated with ultrasonic bath for 20 minutes. One drop of dispersion was dried on a glass substrate for SEM measurement.

Attritor Ground Seed. 20 wt% Potassium chloride (99.6%, Mallinckrodt) and 80wt% grinding media (zirconium oxide balls) were mixed and placed into the attritor. Isopropyl alcohol was then poured into the attritor until the liquid covered the solid

content completely. The rotation speed was 300 RPM and the grinding time is 24 hours. One drop of as prepared mixture was dried on a glass substrate for SEM measurement.

Separation of Small Seed. The attritor ground seed dispersion was loaded into a syringe and was filtered with a 200nm filter (Acrodisc GHP).

Whisker Growth by Seeding. The manually or attritor ground seed dispersion was treated with ultrasonic bath for 20 minutes before seeding. The seed dispersion was then drop cast onto the porous coating and was dried in oven at $70^{o}C$ for 10 minutes. The whisker growth procedure remained the same as standard whisker growth procedure.

4.3 Results and Discussion

4.3.1 Liquid supply at the whisker base

Figure 4.1 shows the top view SEM image for whisker growing for 10 hours under standard condition. Radial patterned equiaxed salt crystal was observed near the base of some whiskers. It indicates that the whisker drew liquid towards its base from the neighborhood for extra-liquid supply during growth, and the salt ions accumulating along the liquid path formed equiaxed crystal after drying. The driving force of the liquid flow towards the whisker base should come from the rapid water evaporation near the whisker base. During whisker growth, the liquid layer adhering to the side wall of whisker had large surface area exposed directly to the atmosphere, therefore the fast water evaporation there drove the liquid towards the whisker. The flatter meniscus on the side wall of the whisker compared with the meniscus in the porous coating also enhanced the water evaporation. This liquid-drawing effect could explain the independence of whisker size on salt concentration. As discussed in the section of whisker growth mechanism, before whiskers grow, small salt crystals form on the porous coating, and these small crystals initiate the whisker growth. During growth, a whisker tends to draw the liquid supply towards its base and deplete the liquid supply around it and thus limit the new whisker growth nearby. Therefore it is difficult for a new whisker to emerge if there are growing whiskers nearby. For a solution of lower salt concentration, the number of small crystals on porous coating at early growth stage is reduced. After whisker growth is initiated by these small crystals, the liquid supply is directed to the growing whisker and thus

suppresses the formation of new whiskers nearby. Therefore the final density of whiskers is lower. Figure 4.2 shows the cross-section SEM images took at initial growth stage. Small salt crystal started to form on the surface of the porous coating. If the salt crystal was passed by the cutting surface as shown in Figure 4.2a,b, the porous coating directly beneath the salt crystal was also filled with salt. However, if the cutting surface did not pass the crystal, no obvious salt residue could be observed in the porous coating after drying even though the salt crystal was nearby. See Figure 4.2c,d. It proves that during growth, liquid supply was drawn towards the whisker and the salt ions accumulated at the whisker base and hence depleted the salt supply nearby.

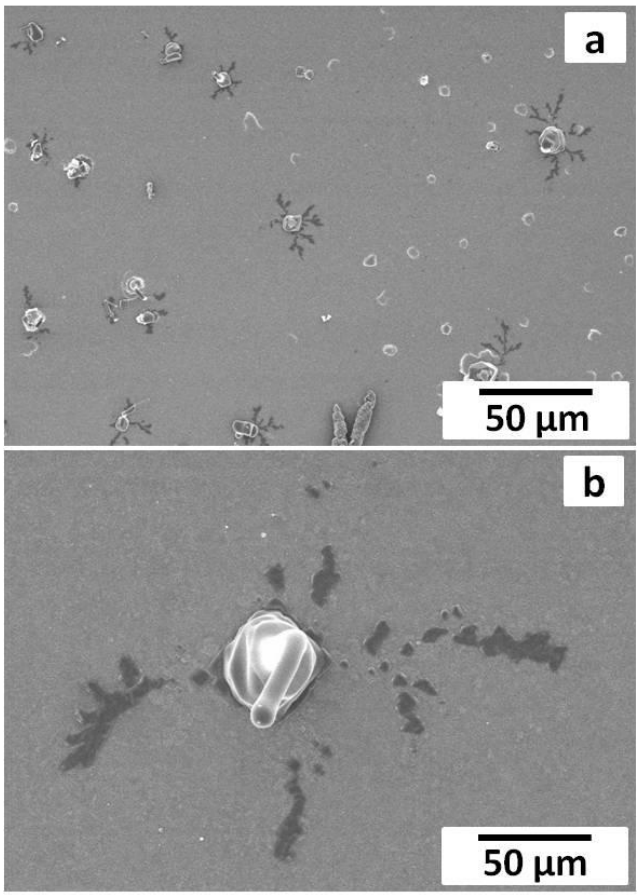

Figure 4.1 SEM image of whisker growth on porous coating under standard growth condition for 10 hours. (KCl 2.9wt% 80%RH)

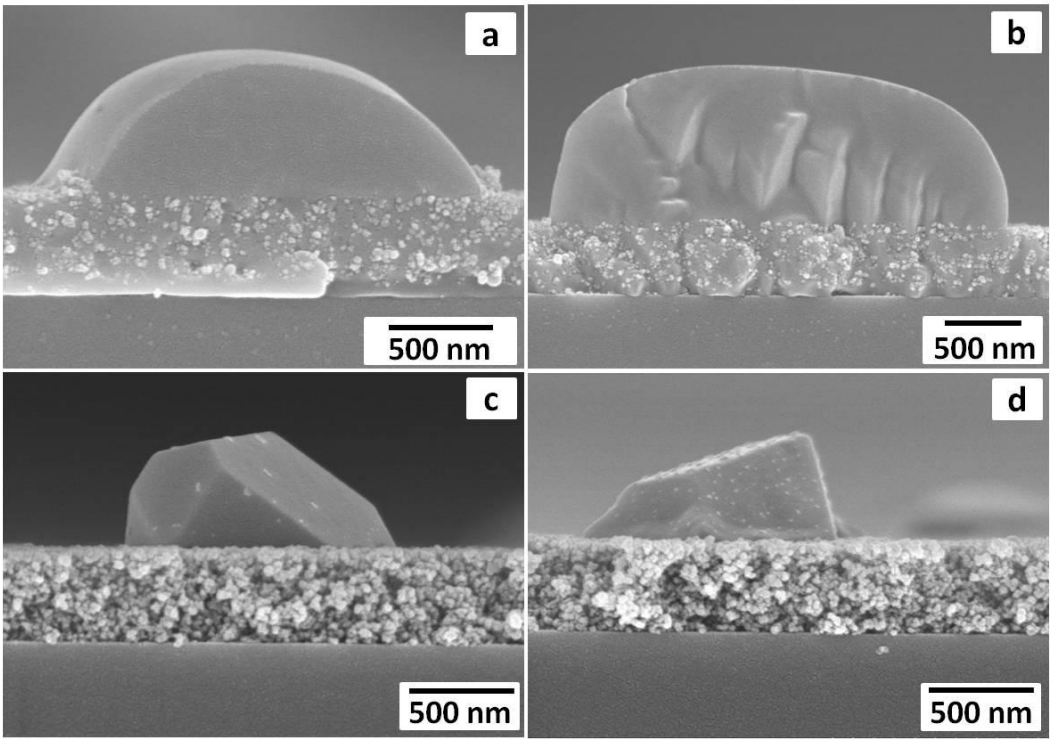

Figure 4.2 Cross-section SEM image of small salt crystal formed on the surface of porous coating at initial whisker growth stage. (KCl 2.9wt%, 80%RH, 2 hours)

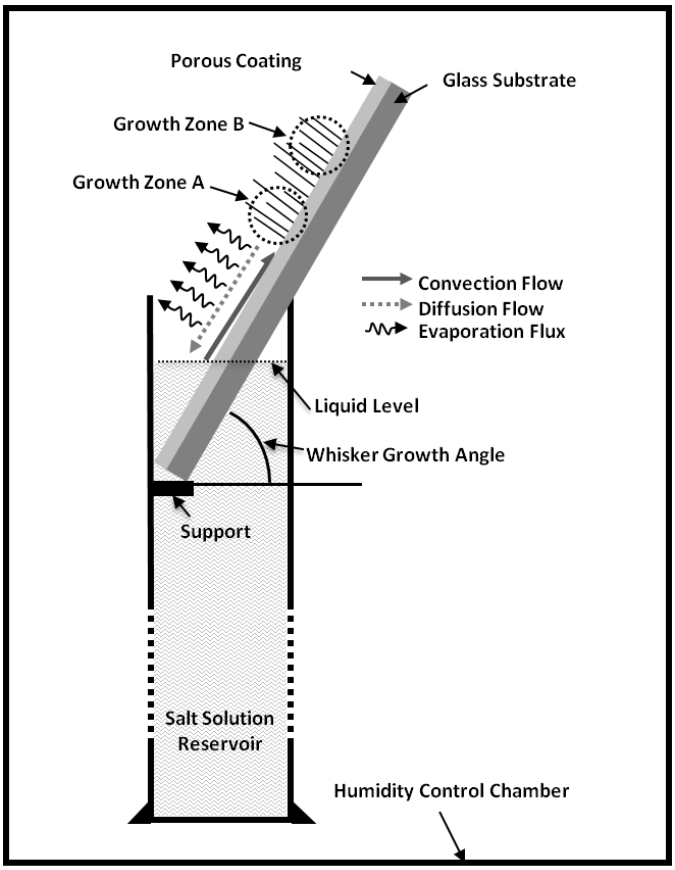

Figure 4.3 Experimental setup for whisker growth on porous coating.

Besides competition between nearby whiskers for liquid supply, competition for liquid also exists for whiskers on different growth areas of porous coating. Figure 4.3 shows the schematic drawing of two whisker growth zones: A and B. Figure 4.4 is the SEM images of whiskers grown at growth zone A (Figure 4.4a,b) and growth zone B (Figure 4.4c,d,e,f) under standard growth condition for 5 days.

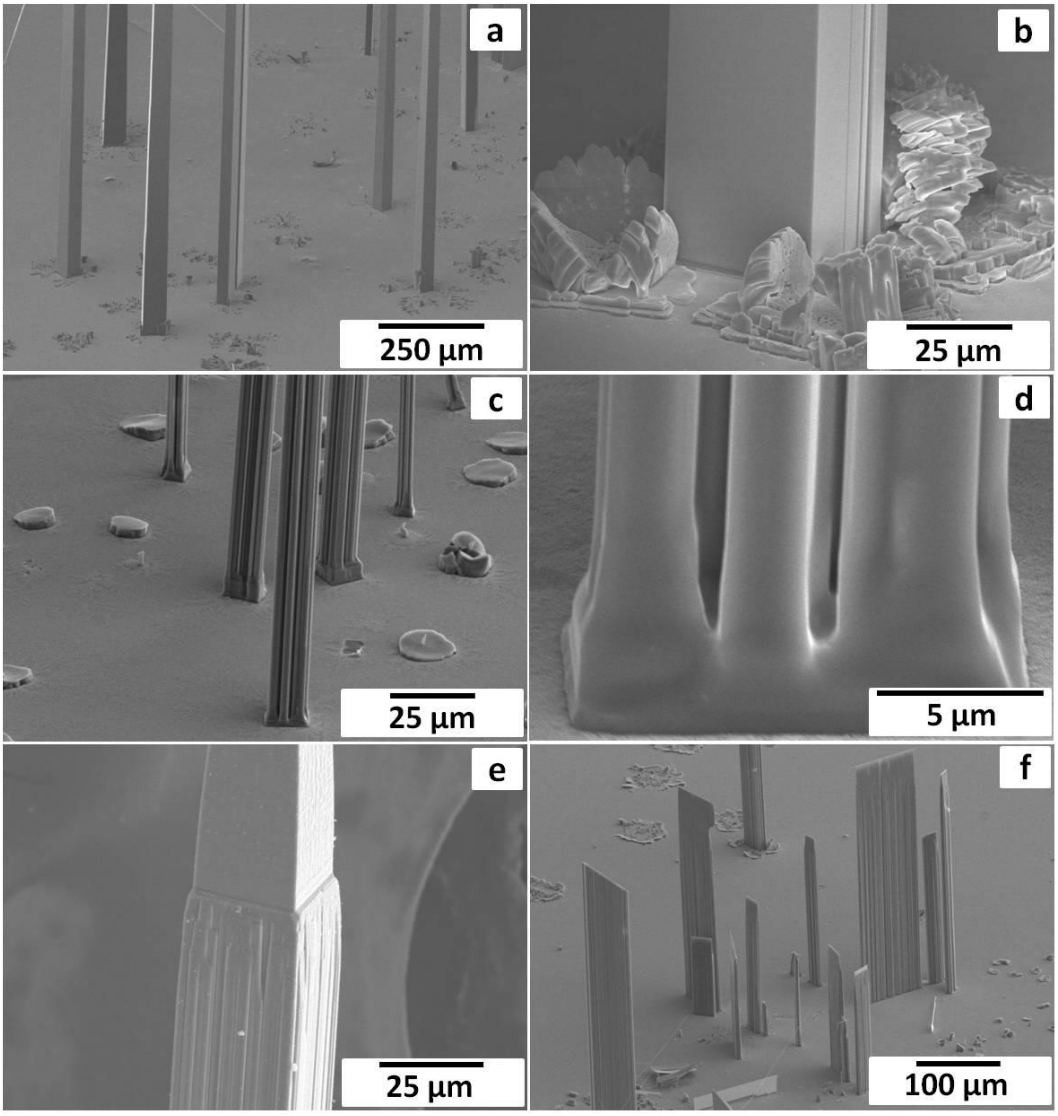

Figure 4.4 SEM image of whiskers grown on porous coating in growth zones A (a,b) and growth zone B (c,d,e,f). (please refer to Figure 4.3)

The whisker width in growth zone A is larger than that of whisker in zone B. The surface of whisker in zone A is smooth compared to the corrugated whisker in zone B. As discussed in chapter 2, whisker first grew in zone B on porous coating, when liquid level dropped due to water evaporation, the whisker growth zone would move downwards and whisker started to grow in zone A. Because zone A was located closer to the solution

reservoir, the liquid supply reached zone A first and large percentage of the liquid flow was consumed by the growing whiskers in zone A. Only a small amount of liquid could reach to zone B. Due to lack of liquid supply and possibly unstable meniscus on the side wall, whisker in zone B had smaller lateral size and corrugated surface. A whisker located between zone A and zone B is shown in Figure 4.4e and the transition from smooth to corrugated surface could be observed on one whisker. This indicated a time point that new whiskers in growth zone A started to emerge and this whisker experienced a sudden drop in liquid supply. An interesting fact is that not only the whisker but also the sheet in growth zone B had corrugated surface as shown in Figure 4.4f.

4.3.2 Whisker growth on patterned porous coating

The liquid supply competition phenomenon indicates that if the liquid supply to the whisker base could be constrained, the width of the whisker might be reduced. Patterned substrate with stripes of coated and uncoated area is one choice to limit the liquid supply to the area with porous coating. A schematic drawing of patterned substrate with hydrophilic coated strips and hydrophobic bare strips is shown in Figure 4.5. The width of porous coating is 50μm and is separated by 50μm uncoated area. The average coating thickness is ~300nm as measured by profilometer.

Figure 4.6 shows the whisker grown on patterned substrate under standard growth condition. It proved that the liquid transport through the porous coating is the key factor for whisker growth and whisker only grew on strips with porous coating. The average whisker width is reduced to ~5μm compared with 10μm on standard porous coating. It indicates that the limit of the liquid supply helped to reduce the whisker width. Using a

coated stripe with smaller width might further limit the liquid supply and reduce the lateral dimension of whisker; however, continuous porous coating with width less than 10 μm was difficult to obtain. Cracks and incomplete coatings were frequently obtained. One interesting observation is that sheet growth initiated by a fallen whisker as shown in Figure 4.6d. Sheets only grew at sections of whisker that were in contact with the porous coating and the growth mechanism of salt sheet suggests another method that has the potential to reduce the whisker width into nanometer scale.

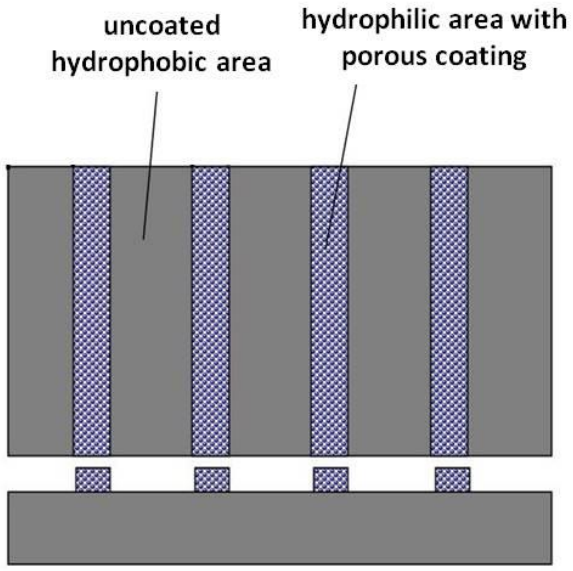

Figure 4.5 Schematic drawing of porous film on patterned substrate.

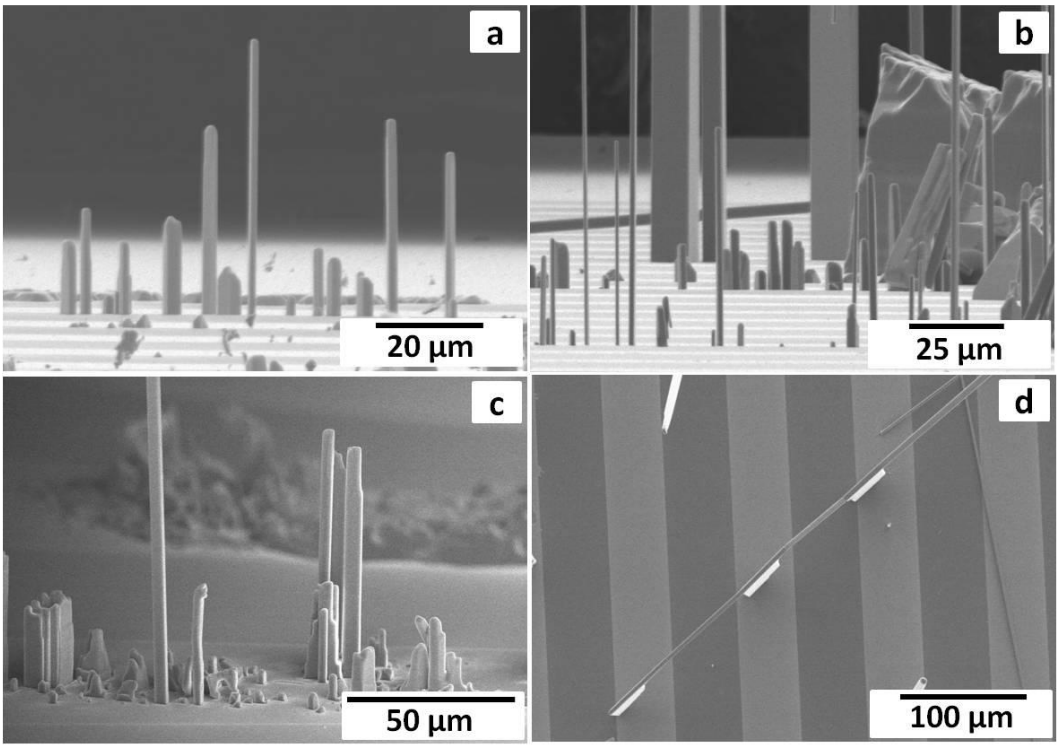

Figure 4.6 SEM images of whisker growth on patterned substrate under standard growth condition.

4.3.3 Whisker growth by seeding

Whisker growth mechanism indicates that a small crystal present on the surface of the porous coating should be able to initiate the growth of a whisker and it inspired us with a new strategy that might reduce the whisker width: Introduce lots of small KCl crystals onto the porous coating as seeds to start large amount of whisker growth simultaneously, and thus purposely initiating liquid supply competition between whiskers for fixed liquid supply and hence limit the whisker width. Actually, the general idea behind this approach is similar to coprecipitation strategy for nanoparticle synthesis[80]: A rapid nucleation step followed by a controlled growth step.

To prepare small KCl crystal as seeds, potassium chloride powder were manually ground in the mortar. The manually ground seeds are shown in Figure 4.7. The sizes of the seeds were in the range of 2 μm to 50 μm and the shapes of the seeds were quite irregular.

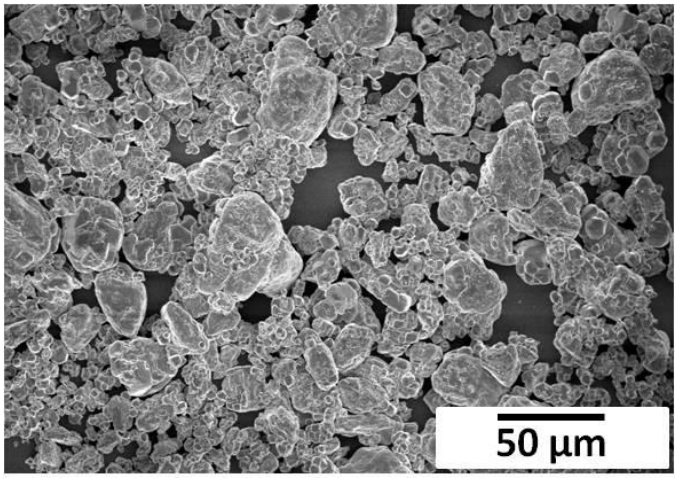

Figure 4.7 SEM image of manually ground KCl seeds.

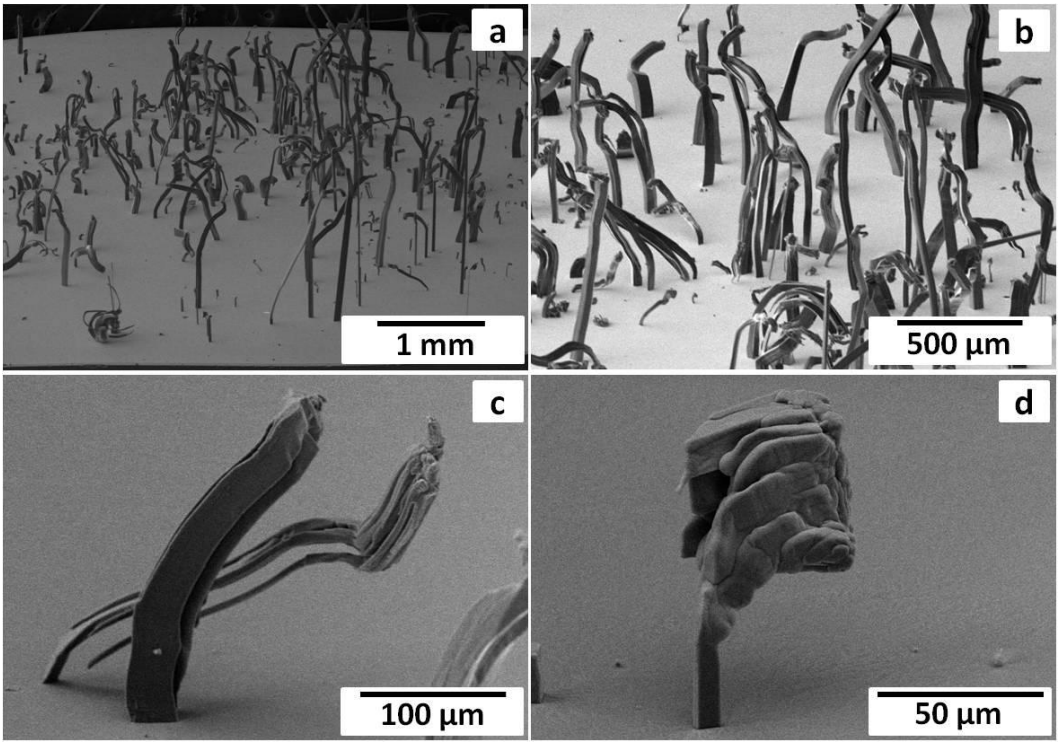

Figure 4.8 SEM image of whiskers grown on porous coating by manually ground KCl seeds under standard growth condition.

The whiskers grown with manually ground seeds are shown in Figure 4.8. The whisker quantity increases compared with sample without seeding. Most of the whiskers were extreme curved and had unexpected larger lateral size than unseeded whiskers. Although seeding with manually ground seed did not reduce the whisker width, it proves the seeding technique is effective to initiate whisker growth. There are several possible reasons to explain why whiskers grown by seeding method have larger width and curved shape. (a) Average size of the manually ground seeds might be larger than the spontaneous formed small salt crystals on the porous coating during standard unseeded whisker growth. Because the whisker tends to have similar lateral dimension as the seed or the spontaneously formed salt crystal, the seeded whisker tends to be larger in width. (b) The existence of connection between liquid supply and the seed is necessary to

initiate whisker growth. Larger seeds have larger areas in contact with the porous coating and thus have high possibility to connect to liquid supply. Therefore most of the whisker has the width similar to the size of the largest seed. (c) The shapes of the manually ground seeds are irregular, and the center of the mass is usually not located at the geometry center of the seed. The large unbalanced "head" makes whisker easier to tilt, and then the balance will be restored because of liquid layer support at the whisker base as discussed in Chapter 3. The repeated tilt-rebalance processes should contribute to the extremely curved whisker shape. (d) the seed density is not high enough, therefore liquid supply competition effect was not sufficient to reduce the whisker width. However, it still suppressed the growth of spontaneous formed whiskers as there is few straight whiskers could be observed in Figure 4.8.

One interesting fact is that sometimes one large seed could initiate the growth of several whiskers bundled together as shown in Figure 4.8c. The whisker grew at such an angle without falling was quite astonishing, and it is another evidence for the support liquid layer at the base. In some cases, a large seed may initiate a much thinner whisker compared to its own size. See Figure 4.8d.

To improve quality of the seed, an attritor mill was used to prepare smaller seeds with narrow size distribution. The attritor ground seeds are shown in Figure 4.9 and it shows the seed size was reduced significantly and most seeds were in the range between 200nm to 1 μm.The variance of the seeds size also decreased and most of the seeds were cubic shaped crystals.

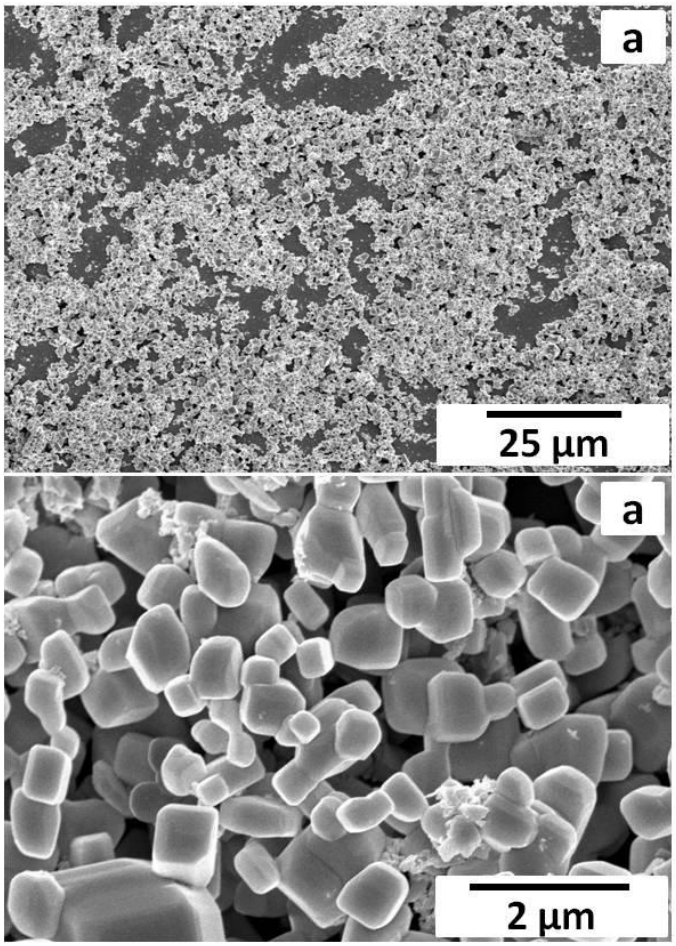

Figure 4.9 SEM image of attritor ground KCl seeds.

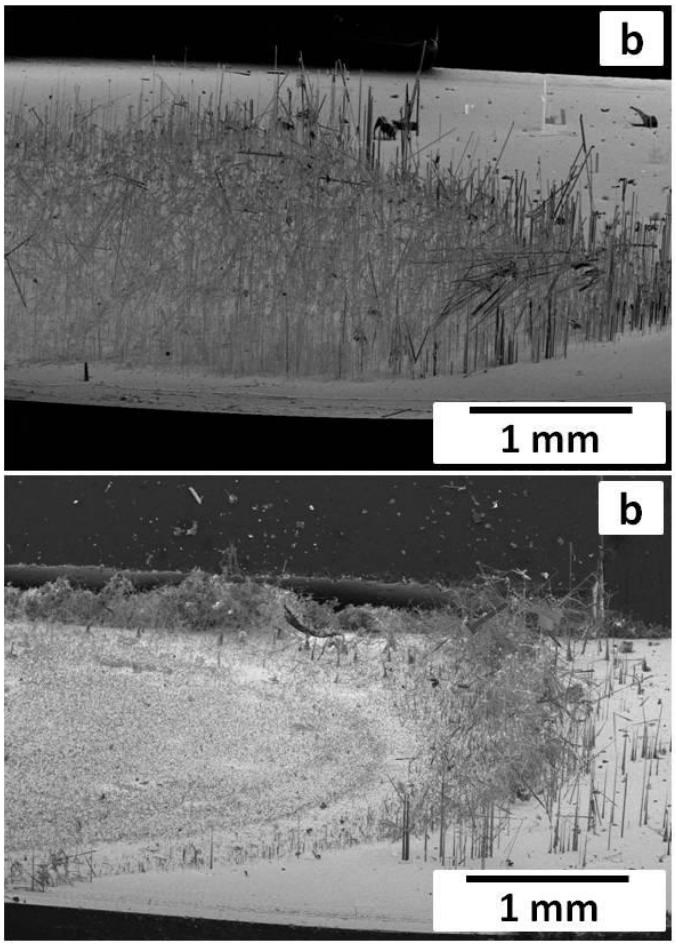

Figure 4.10 SEM image of whiskers grown on (a) 150nm aggregates 80%RH and (b) 22 nm particle porous coating 70% RH by seeding with attritor ground seeds. (KCl 2.9 wt% , 2 days.)

The attritor ground seeds were dispersed in proper amount of isopropyl alcohol to adjust seed concentration. The mixture was drop cast onto the porous coating before whisker growth to serve as seed. The whiskers seeded by attritor ground seeds are shown in Figure 4.10. All whiskers were located within the area covered by the seeding drop. This result indicates that the seeds assisted whisker growth and whisker grew only in the area with seeds. Outside the seeding circle, there was almost no whisker growth and it suggested that the liquid flow was drawn towards the seeded area and suppressed the

spontaneous whisker growth elsewhere. For Figure 4.10a, the lateral dimensions of the whiskers grown in the circle were quite homogeneous and most whiskers had width about 1 μm to 5 μm. However the whiskers located at the right edge of the seeding circle seemed to have larger width. Because the right side was the lower end of the substrate, the whiskers located at the right side of the circle gained liquid supply first. Especially for those whiskers located at the edge, as there were fewer whiskers nearby to compete for liquid supply compared with the whiskers in the center of the circle, the whisker lateral size was obviously larger. Similar phenomenon occurred for seeded growth on 22 nm particle porous coating as shown in Figure 4.10b. However, in this case, whisker only grew at the outer lower side of the seeding circle. Almost no whisker grew in the center of the circle and the liquid competition phenomenon seemed to be more obvious in this case.

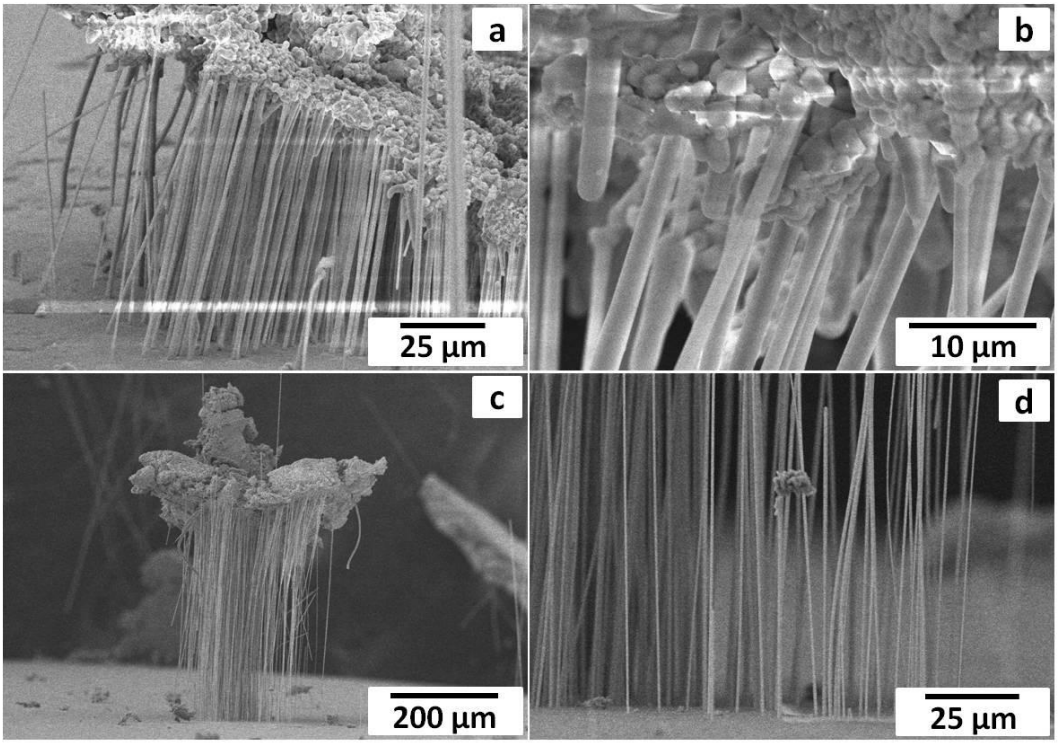

Figure 4.11 SEM image of whiskers grown on 150nm aggregates porous coating by seeding with agglormerate of attritor ground seeds under standard condition.

To maximize the liquid supply competition between whiskers, a high concentration seed dispersion was used for seeding. After drying, the seeds agglomerated into a large chunk as shown in Figure 4.11. The images show that numerous whiskers grew under one seed chunk and pushed the whole chunk upwards. Some whiskers that grew slower or were short of liquid supply were brought up by other fast growing whiskers and thus hung in the air without touching the porous coating. The lateral dimension of the whiskers was about 1 µm to 2 µm, and the width was reduced because of enhanced liquid supply competition. However, the cross section of some whiskers changed from the usual rectangular shape to circle shape. Sarig[81]mentioned in his paper that the rounding of the sharp edge of the potassium chloride might be due to dissolution,

special mode of growth or mechanical attrition. In our case, mechanical attrition is not possible as no physical contact is expected between whiskers during growth. Special mode of growth might be a reasonable explanation. Because the whiskers shared the same seed chunk, the up growing whisker with higher growth speed would lift other whiskers with it and limit the lateral growth of the other whiskers. The constrained lateral growth might change the crystal habit and made the outer-surface of the whisker deviate from its cubic shape. Dissolution is also possible. The ultra-high density of whiskers growing at the same time might deplete the salt ions in the vicinity and decreased the salt concentration at the whisker base. The dissolution would occur preferentially at the sharp edge of the whisker and thus formed a round whisker.

The study of porous coating particles and growth angle effect on whisker growth shows that porous coating with smaller particle size has a smoother surface to provide better support for whisker with smaller width. Therefore, porous coating made of 22 nm particle was used for the seeding method to see whether the whisker width could be further reduced. The seeded growth of whiskers on 22 nm particle porous coating is shown in Figure 4.12. The whisker width was similar to that of the whisker grown on 150 nm aggregates coating. However, the seed concentration seemed to be too high and the extra seeds were attached to the side wall of the whisker during growth

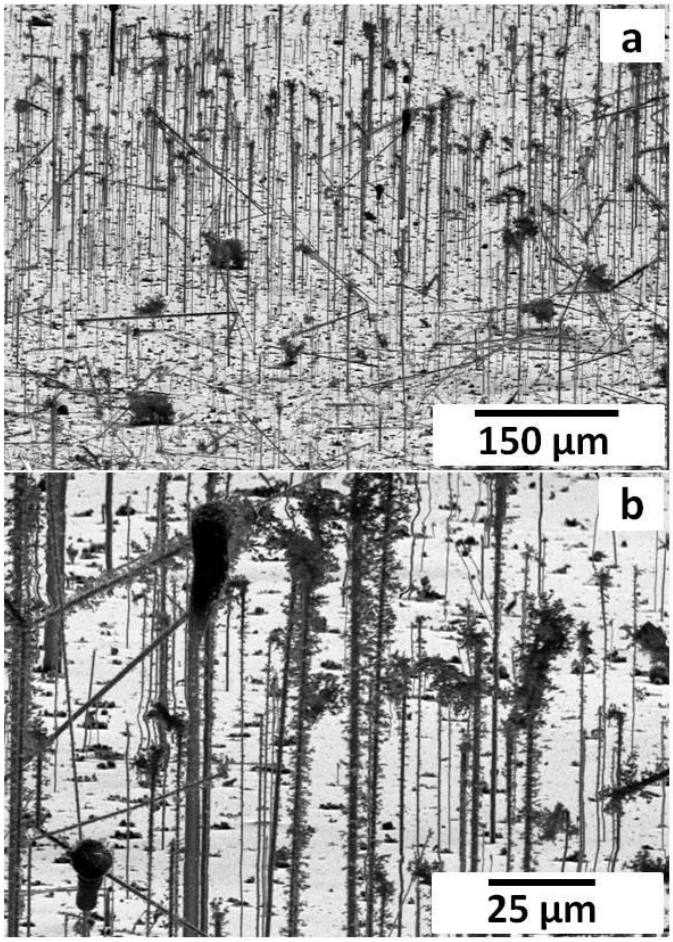

Figure 4.12 SEM image of whiskers grown on 22nm particle porous coating by seeding with too many attritor ground seeds. (KCl 2.9wt%, 70% RH, 2 days.)

By proper seed concentration, whiskers with almost identical width could be grown on porous coating and the lateral size of whisker was reduced to ~500 nm to 1 µm as shown in Figure 4.13. The result indicates that the coating particle size might not be the most important factor to reduce the whisker size. Although particle size needs to be smaller than the width of the whisker to provide stability support, the particle itself could not reduce the whisker width. The key factor to influence the whisker width should be the

size of the seed. The seed size determines the tip size of the whisker and it in turn defines the initial whisker width. Because most of the attritor ground seeds are in the range of ~1 μm to 2 μm, the whisker width is also fall in this size range. Sometime, because the saturated water vapor pressure is lower near the nanopores between the seeds and porous coating, capillary condensation of water would dissolve part of the seed and thus reduced the seed size. Therefore 500nm whisker could be observed. Capillary condensed water might also serve as a bridge to help connect the seed to the liquid supply in the porous coating.

The whisker width would increase if growth occurs on the side wall and hence tapered whisker would form as shown in Figure 4.14a. A close look at the tapered whisker revealed each step of the whisker width increase. See Figure 4.14b. However, if the liquid is deficient, the whisker width might decrease or form corrugated side wall as discussed in section 4.3.1.

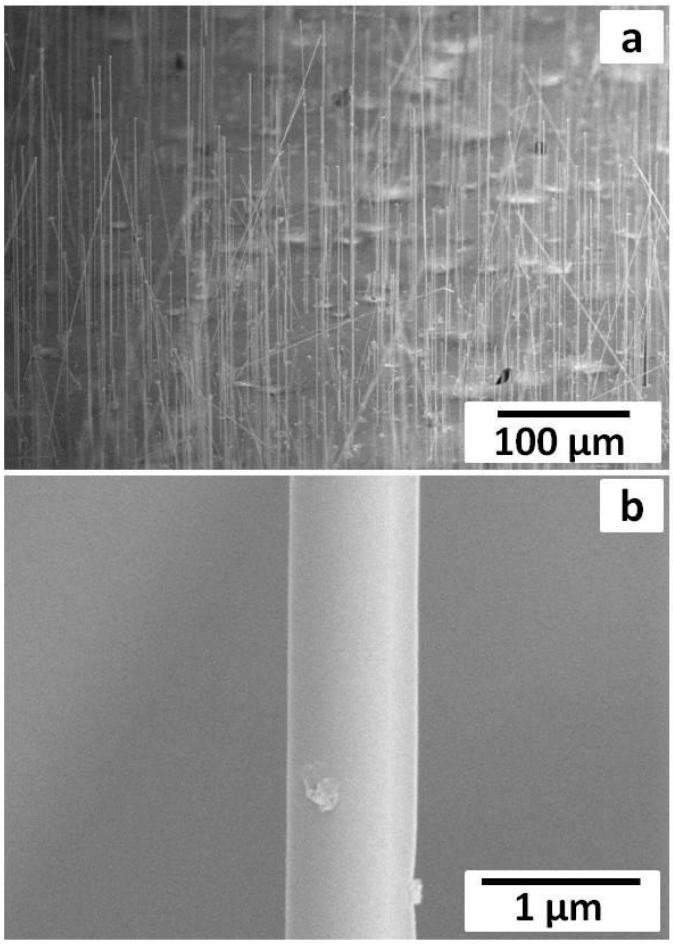

Figure 4.13 SEM image of whiskers grown on 22nm particle porous coating by seeding with proper amount of attritor ground seeds. The growth condition are KCl 2.9wt%, 75%RH, 2 days.

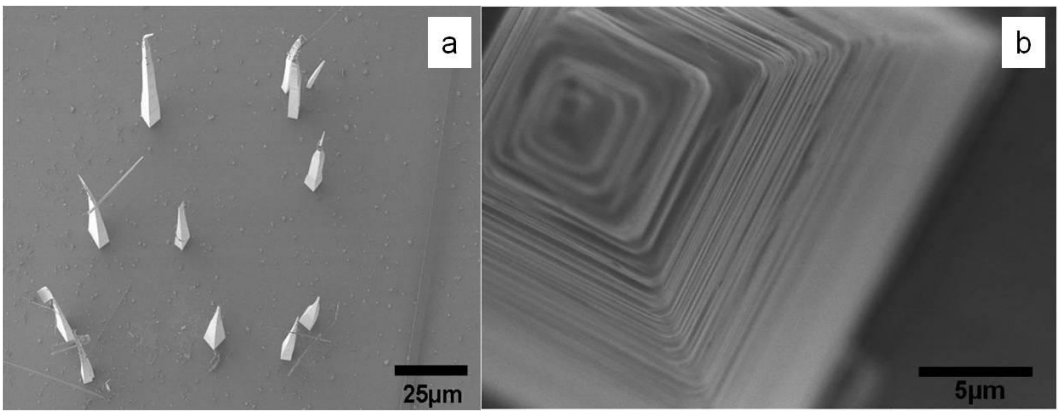

Figure 4.14 SEM image of tapered whisker grown on porous coating under standard growth condition.

Based on the results obtained, further reducing seed size might be the solution to reduce whisker width to nanometer scale, however, attritor has a limitation on breaking down particles and average particle size less than 1 μm is usually very difficult to get no matter how long the attrition time is. However, small percentage of the attritor ground seeds are actually nanoparticles and could be used as nanosized seeds. Therefore a 200nm filter is used to separate the nanoparticles. More than 99 wt% of KCl particle were removed and only seeds less than 200nm remained in the dispersion. The seed after drying is shown in Figure 4.15. However, unlike large seeds, most of the particle less than 200nm had irregular shape. These extreme tiny crystals might be the debris produced by the collision between large salt crystals and grinding media and thus has asymmetrical shape.

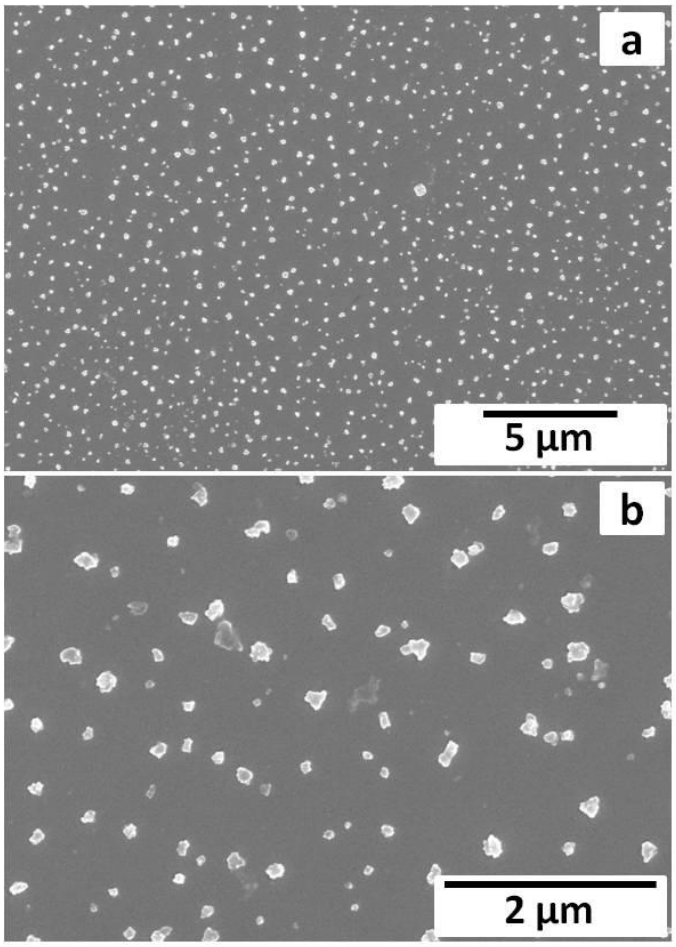

Figure 4.15 SEM image of filtered attritor ground KCl seeds with 200nm filter.

Because the concentration of the 200nm seed dispersion is very low, the seeding process was repeated for 20 times and the whiskers grown by seeding were shown in Figure 4.16. The lateral dimension of the whisker was reduced significantly to less than 200nm. Some whiskers had width of ~50nm was shown in Figure 4.16e,f. With reduced whisker width, the whisker length also decreased significantly and this may be due to the increased whisker aspect ratio. As high aspect ratio tends to trigger instability and make whisker easier to tilt or fall. Most of the whiskers with nanosized width were tilted as shown in Figure 4.16c,d.

In conclusion, seeding could initiate whisker growth. The whisker width could be controlled by the size of the seeds. Whisker with lateral dimension as small as 50nm has been successfully synthesized and further reducing whisker width is possible if smaller seed is used.

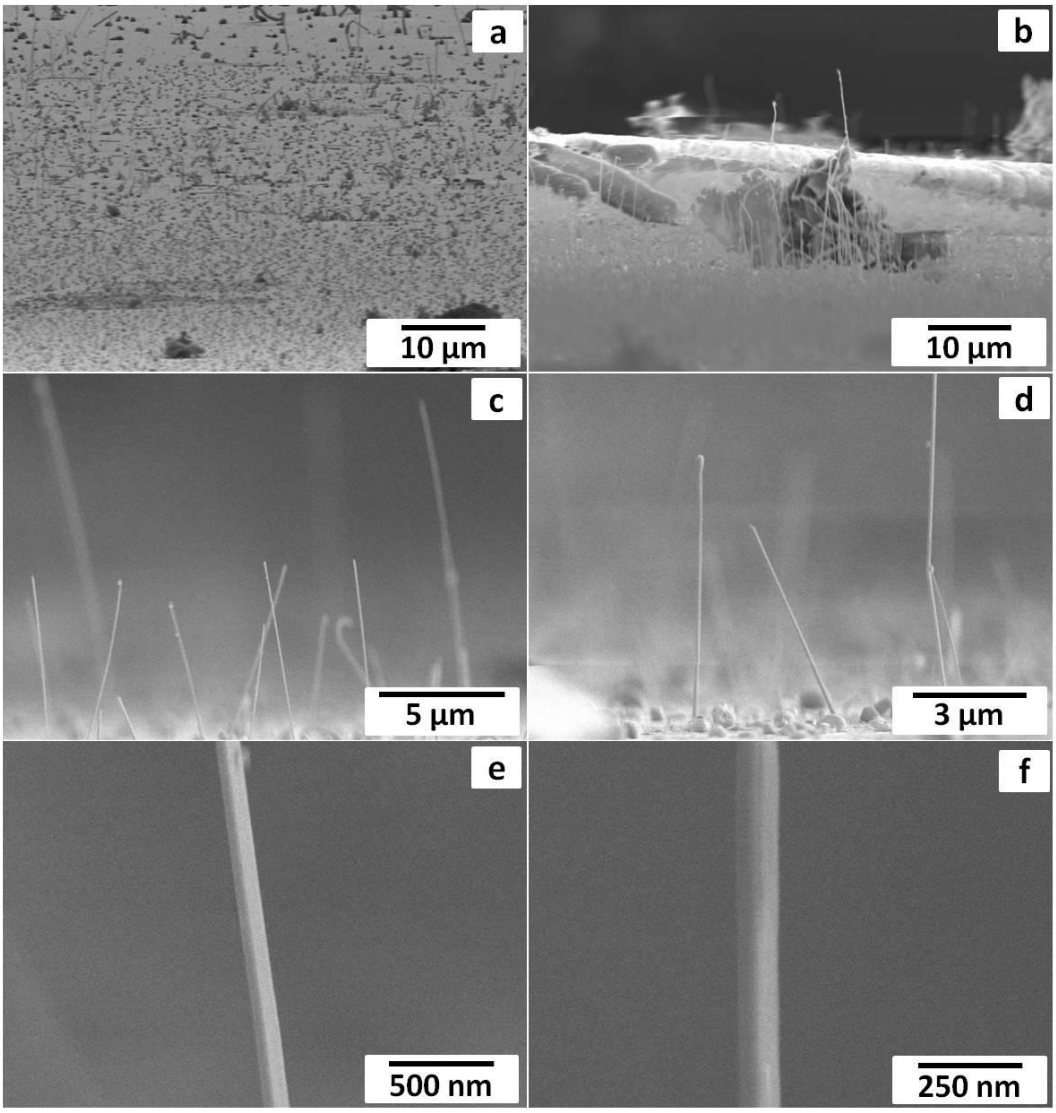

Figure 4.16 SEM image of whiskers grown on 22nm particle porous coating by seeding with 200nm filtered seeds. The growth condition are KCl 2.9wt%, 75%RH, 2 days.

4.4 Future Work

4.4.1 Whisker Size Control

Based on the study of whisker growth by seeding, in order to further reduce the whisker width, the seed size must be reduced. There are several methods that could possibly further reduce seed size and they are listed as below;

(a) In our research, the seed size is limited by the filter pore size. If a finer filter such as nanoporous alumina or silicon membrane with smaller pore size could be used to separate the attritor ground seeds, it maybe possible to obtain seeds less than 50 nm.

(b) Inspired by the factor that during seeded whisker growth, seed size was reduced because part of the seed was dissolved by the capillary condensed water, if the relative humidity could be raised at the initial growth stage to enhance the seed dissolving, whisker with smaller width could be obtained. However, the proper adjustment of the relative humidity level and the timing is the key to success.

(c) Instead of the top down method, we can use bottom up strategy to synthesize salt nanoparticles seeds. Annen [82] developed a chemical synthesis method to make dispersible sodium chloride nanoparticles. Harmon[83] reported that with an electrospray particle generator, NaCl nanoparticle less than 20nm could be gained.

4.4.2 Examination of Dislocation

Although several methods that were tried to locate dislocation in whisker failed, it is still possible that dislocations existe in the whiskers and assiste the whisker growth. The possible reasons are (a) the dislocation locating techniques used in the research were developed decades ago and some procedures were not documented in detail or might not be easy to repeat. This might cause the failure of finding dislocation in the whisker.

Recently Bierman[84]and Morin[85] developed a TEM method and successfully located the dislocation in PbS nanowire and ZnO nanotube. For seeded growth whiskers, because the attrition process could generate dislocation in the seed due to mechanical collision, it might be the source to assist whisker growth. This TEM technique could be used to apply to salt whisker less than 100 nm to check whether dislocation assists the whisker growth.

4.4.3 Growth of Whisker of Other Materials

Compared to vapor phase and solution phase nanowire synthesis techniques, our technique for whisker growth from solution saturated porous coating is relatively simple and cost effective. Figure 4.17 shows the preliminary results of sodium chloride and potassium bromide whiskers grown on porous coating. It proved that this technique could also be applied to grow whiskers of other water dissolvable salts. Furthermore, this whisker growth method might also work for materials dissolvable in non-polar solvents as long as the vapor pressure of the solvent could be controlled.

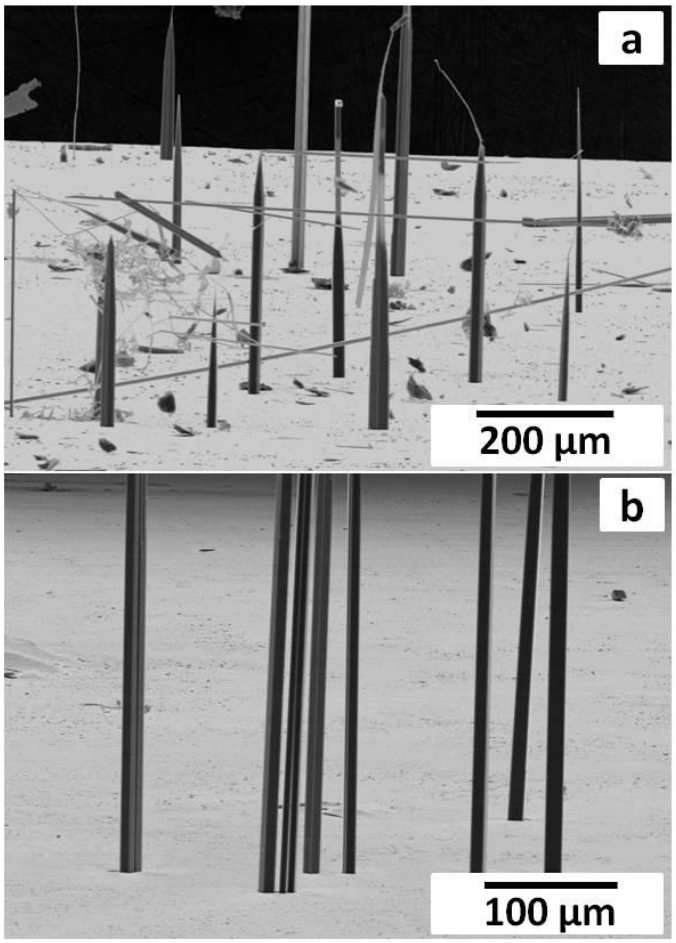

Figure 4.17 SEM images of NaCl (a) and KBr (b) whiskers grown on porous coating. (NaCl: NaCl 2.9wt%, 70%RH, 2 days. KBr: KBr 2.9wt%, 67%RH, 2 days)

4.4.4 Applications of Whisker

There are many possible applications for the whiskers grown from porous substrate. Superior mechanical property of whisker has been discovered for a long time.[2, 3, 10, 12] This results from few imperfections existed in the whisker. Recently, Moore[86] discovered superplastic NaCl nanowire pulled from the surface of common salt and the superplastic might also exist for the whiskers growth from porous coating and it is worth testing.

Nowadays, nanowire and nanotube attract a lot of interest because of its unique properties.[87-92] Compared with carbon nanotubes or other popular nanotube or nanowire grown by vapor phase deposition, the whisker grown from solution is dissolvable, so that it can be used as a sacrifice material. Hou[93] investigated the composite by mixing polymer and water soluble salt particles. By dissolving the salt, soft porous polymer was obtained. This could also be applied to the whisker. First, the whisker can be mixed with some kind of polymer to increase mechanical strength of the composite. Then, the whisker could be removed by simply dissolving it in aqueous solution to release the soft polymer.

KCl is also widely used as a window material for infrared application because of its superior optical transmission in the infrared range. KCl whisker might be used in some photonic devices due to its IR transparency.

Besides KCl, the same growth method can be applied to a lot of other materials. With unique mechanical, magnetic and electronic property of different material, specific application can be achieved by certain kind of whisker. For example ferroelectric whisker (KH_2PO_4) shows unique ferroelectric property compared to its bulk crystal.[38]

Chapter 5 Coating onto Open Celled Foam

5.1 Introduction

Solid foams, manufactured from metal, ceramic, polymer or carbon have a variety of applications due to their high surface area, low relative density and complex interfacial geometries. Solid foams have been used as heat exchangers, energy absorbers, high temperature filters, electron emitters, fuel cell electrodes and catalytic supports.[94-100] There are two types of solid foams: closed celled foam, in which the cells are isolated, and open celled foam, in which the cells are open and interconnected.[101,102] The properties of open cell foams can be improved and altered by adding a coating onto the internal foam surfaces.[96,100,103-105]

Solid foams with interconnected porosity are good candidates for structured catalytic supports.[97,98,106] The foam structure leads to a low pressure drop and turbulent flow, which increases interaction between the catalyst and reactant. For conventional structured catalytic supports, such as honeycombs and monoliths, a mesoporous layer is added to further increase the surface area before the active metal catalysts are added.[107-113] This strategy can also be used for solid foam catalytic supports.

Chemical vapor deposition (CVD) is one choice to create a coating on the internal foam surfaces. For example, several reports[114,105,95] have detailed the synthesis of carbon nanofibers onto the surfaces of carbon foams. Additionally, Kobashi *et al* [96] reported CVD deposition of a diamond coating on carbon foam. In these CVD methods, a two-

step process was used. In first step, a catalyst or seed layer was coated on the foam by a solution phase method, and in second step, the carbon nanofiber or diamond coating was deposited onto the foam by chemical vapor deposition. Although the CVD method shows good coating quality, it is relatively expensive and time consuming. Another disadvantage of CVD is that only a limited number of materials can be deposited due to the gas phase reaction.

Another method to coat open celled foam is by liquid phase deposition. Scheffler and coworkers[99] and Bonaccorsi and coworkers[115] reported coating a thin zeolite layer onto foams by direct hydrothermal synthesis. However, this process is complicated, and the final coating thickness is also limited. An easier and faster liquid phase coating alternative is dip coating. This method has been widely used in conventional catalyst industry to create a "washcoat" onto monolith and foam structures. The washcoat is usually made by immersing and removing the foam or monolith from a sol-gel solution or slurry of particles; sometimes vacuum is used to assist filling of the pores or channels.[104] To avoid blockage after drying, the excess liquid trapped is usually removed by blowing compressed air [97,98,106,107] or rotating.[116] The development of protocols for these processes has been empirical.

In this paper, a method to coat open cell foam by a combination of dip coating and spin coating is developed and studied systematically. The emphasis of the research is on the coating process and understanding the experimental parameters that influence thickness and uniformity. The process is then demonstrated with two coating systems that have catalytic applications: γ-alumina and zeolite.

5.2 Experimental Materials and Methods

5.2.1 Solid foams

Carbon foams were purchased from ERG Aerospace Corporation. The structure of the foam consists of solid interconnecting struts that enclose a central void or "cell". Pores in the cell are defined as the openings in the cell, as shown in Figure 5.1. Foams are characterized by the number of pores per inch (PPI). In this research, carbon foams with 10, 20 and 30 PPI were used. Foams were cleaned ultrasonically in acetone and water, and dried in the oven at 70 ℃ for 1 hour before use. For consistency, all foam pieces were 2" x 2" x 0.8" in dimension.

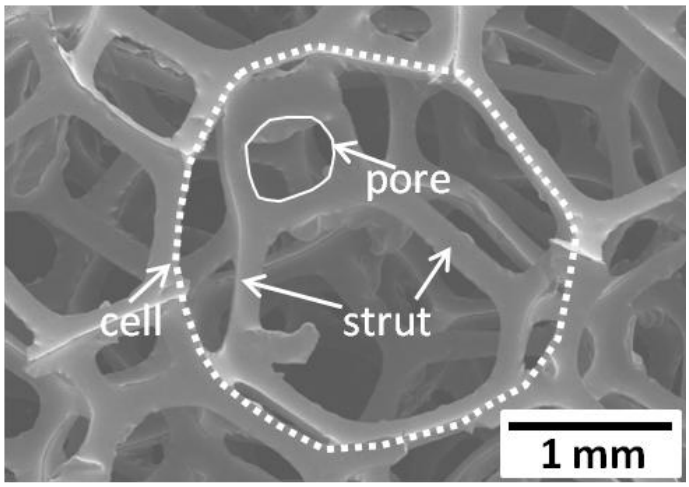

Figure 5.1 SEM image of a fractured 30PPI carbon foam.

5.2.2 Model coating solutions

To study the liquid deposition process, solutions of glycerol and water were used. Required amounts of glycerol and water were mixed thoroughly and put in an ultrasonic

bath for 30 minutes before use. Glycerol/water solutions with a range of viscosities were prepared. The viscosity and surface tension of solution were measured by a viscometer (Brookkfield DV-II+) and a tensionmeter (Kruss K10ST), respectively. See Table 5.1. Unlike viscosity, the surface tension of the solutions did not vary much. For some experiments, the surface tension of the solution was adjusted by a surfactant (Aerosol MA80% from Cyanamid). The amount of the surfactant was less than 0.1 wt%.

Table 5.1 Viscosity and surface tension of glycerol/water solutions

Glycerol	Viscosity (cP)	Surface Tension (mN/m)
70%	23	66.7
80%	47	66.1
90%	142	65.7
95%	419	65.2

5.2.3 Dip coating

A computer controlled linear driven stage from Parker Automation was used for dip coating. See Figure 5.2. The withdrawal speeds could be precisely controlled from 0.05 to 500 mm/s. A weight monitoring module from Futek Advanced Sensor Technology, Inc was attached to the arm of the linear driven stage. The weight of the foam, attached to the linear stage, was measured dynamically during dip coating process. The results are presented as an average coating thickness:

$$\text{Average Coating Thickness} = \frac{\dfrac{\text{Coated Foam Weight - Initial Foam Weight}}{\text{Surface Area of Foam}}}{\text{Density of Coating Liquid}} \qquad (5.1)$$

where the initial foam weight is the weight of the bare foam measured before the experiment and the coated foam weight is taken as the weight of the coated foam as soon as it was withdrawn completely from the solution. All foam pieces were the same size. The surface area was calculated from the manufacturer's specific surface area data and the foam weight. The withdrawal speed was limited to 5 mm/s, because at higher speeds there was significant drainage of the entrapped liquid after the complete withdrawal from the solution.

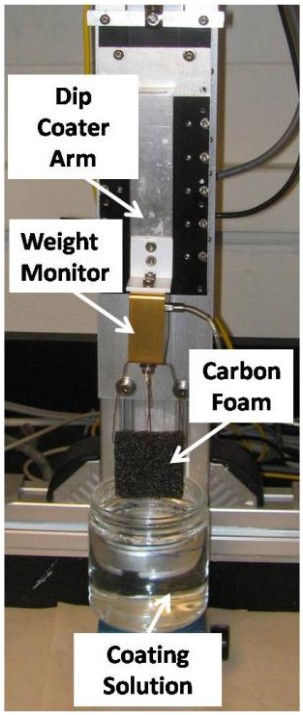

Figure 5.2 The setup for dip coating, including a computer controlled stage and a dynamic weight monitoring system.

5.2.4 Spin treatment

A commercial spin coater (Headway Research, Inc PWM320) was modified for spin treatment of foam. The solid foam, after dip coating, was mounted onto an adaptor, as shown in Figure 5.3. The spin time, spin speed and acceleration could be precisely controlled. As described later, initial experiments showed that the amount of liquid initially loaded into the foam by dip coating was not important to the final amount of liquid on the foam. Therefore, a simple dip coating by hand procedure was used. The size of the foam was kept constant at 2” x 2” x 0.8”.

A spin treatment was used to remove the excess trapped liquid from the foam and to re-distribute the coating liquid more uniformly over the internal surface of the foam after dip coating. To track the coating thickness, the initial bare foam was weighed before the experiment, and the final coated foam weight was determined by weighing the foam immediately after the spin treatment. The average coating thickness is calculated using Equation (5.1).

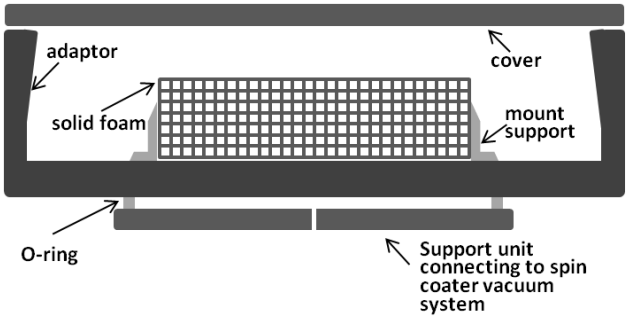

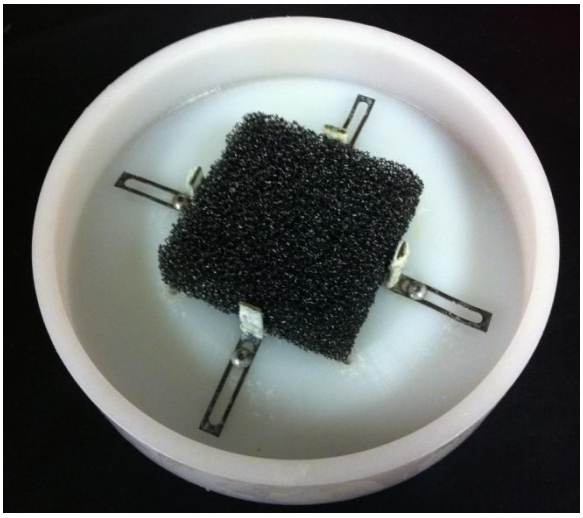

Figure 5.3 Schematic cross-section (top) and photograph (bottom) of the adaptor used to hold the foam on the Headway Research spin coater during spin treatment.

5.2.5 Alumina coatings

Aqueous alumina coating suspensions contained 5 wt% boehmite (AlOOH) powder, 10 wt% γ-Al_2O_3 powder and 2 wt% poly(vinyl alcohol). Dispersible boehmite powder (Sasol; Dispal 23N4-80) has an average dispersed particle size of 90 nm. The

specific surface area after activation at 500 ℃ for 3 hours is 200 m^2/g. Gamma alumina powder (Sumitomo Chemicals, ADP G015) has an individual particle size of 50 nm and the specific surface area is 150 m^2/g. Polyvinyl alcohol (Celanese, Celvol 523) has a molecular weight in the range of 85,000 to 124,000 g/mol. To prepare the suspension, boehmite powder was first dispersed in distilled water by stirring at 500 rpm at room temperature for 1 hour. γ-Al_2O_3 powder was then added, and the mixture was stirred for another 12 hours before diluted nitric acid was added to adjust the pH of the suspension to 3.5. Lastly, aqueous polyvinyl alcohol solution (10 wt%) was added, and the mixture was stirred for at least 12 hours before use.

Before coating, carbon foam was dip coated and spin treated with pure water. This procedure helped the suspension wet the foam and fill all the voids during dip coating. The wetted foam was then coated with alumina suspension by dip coating followed by a spin treatment at 2000 RPM for 60 s. For multiple coatings, the specimen was dried in the oven at 70°C for 1 hour between each coating layer. The coated foam was then heated at 2 ℃/min to 600 ℃ and held there for 3 hours to convert boehmite to γ-Al_2O_3.

5.2.6 Zeolite coatings

The coating liquid for zeolite coatings was a suspension of zeolite nanoparticles with platelike morphology (0.4 wt%) in a polystyrene (9.6 wt%)/toluene (90 wt%) solution. The zeolite, MCM-22(P) with Si/Al ratio of 20, was synthesized[117] and was exfoliated by shear in a polymer melt.[118]

The zeolite coating was made onto aluminum oxide foam obtained from Hi-Tech Ceramics Inc. (45 PPI). The morphology of this support is very similar to the carbon foam structure shown in Figure 1. The dip and spin approach was used with a spin speed of 1500 rpm and the spin time of 30 seconds. The dip and spin coating process was repeated 5 times to increase the coating thickness. Between each repetition, the coating was dried at 80 °C for at least 3 hours. Then the coated alumina foam was heated at 540 °C for 6 hours to thermally decompose and remove the polystyrene. A heating and cooling rate of 1 °C/min were used.

5.3 Results and Discussion

5.3.1 Dip coating

Figure 4 shows a plot of dynamic weight change for a 10PPI carbon foam as it is immersed into and withdrawn from a glycerol/water solution. The positions of solid foam relative to the liquid level are also shown. Before the experiment, the balance was zeroed with dry foam attached; therefore, the y-axis is the weight relative to the dry foam weight. On initial immersion, the foam contacts the solution at point B. Because the carbon foam is relatively hydrophobic, the measured weight dropped steeply as the liquid resisted penetration into the foam pores. After that, continuing to point C, the measured weight decreased gradually due to buoyancy. Air bubbles were observed within the foam as it entered the solution, but most of these rose to the surface as the foam moved deeper into the solution. At point D, the foam was almost completely immersed into the solution. The steep increase in weight after point D occurred when the foam was completely beneath the solution surface. At this time, some trapped air bubbles were still observed. Then the foam was withdrawn from the solution. Until point F, no weight change occurred as the whole foam was still immersed in the solution. At point F, the foam started to emerge from the solution, and the weight increased gradually due to loss of buoyancy. At point G, about ¼ of the foam was out of the solution, as calculated by the ratio of projected lengths of curve FG to FH onto x axis. From point G, the weight increase rate was reduced because the liquid trapped within the foam cells started to drain back to the solution reservoir. The competition between the weight decrease by drainage and the weight increase by loss of buoyancy resulted in the roughness in the data from G

to H. By studying different withdrawal speeds, we noted that the ratio of the projected lengths of curve FG to GH on time axis increased with increasing withdrawal speed; there was less time for liquid drainage at higher withdrawal speed. At point H, the foam was withdrawn completely from the solution and the foam weight dropped back suddenly because of the vanishing of the meniscus. The final weight gain was recorded as the weight value at point I.

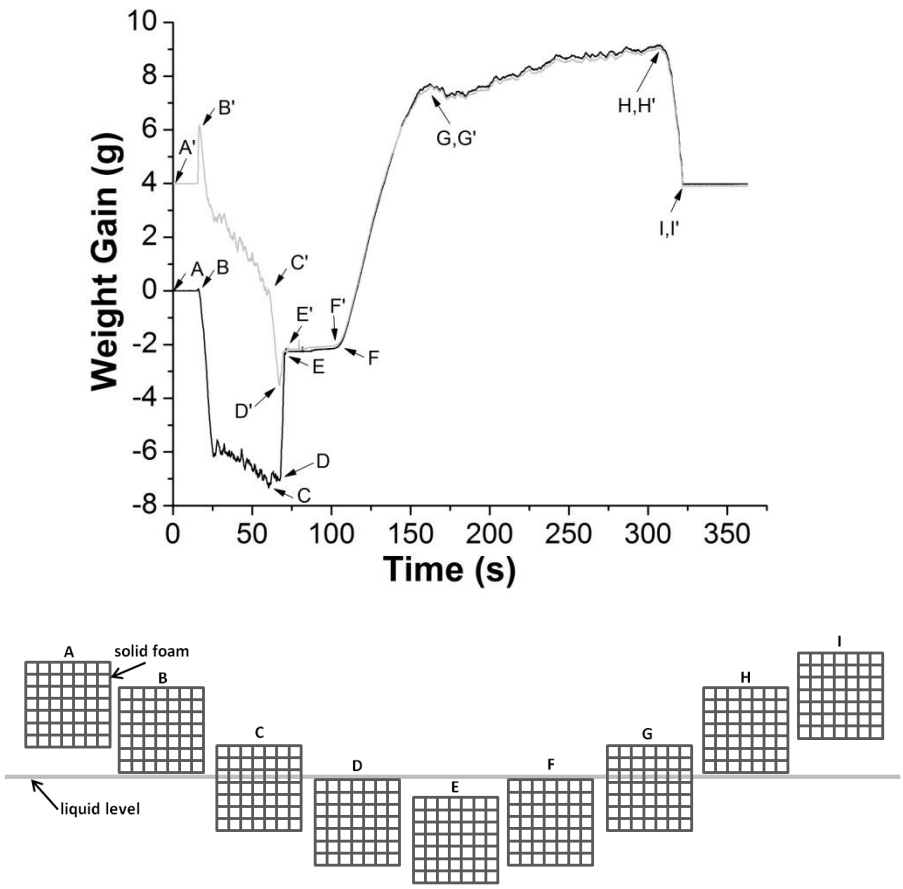

Figure 5.4 Weight of a 10 PPI carbon foam, relative to its dry weight, measured as it was immersed at 1 mm/s and withdrawn at 0.25 mm/s from a 90 wt% glycerol/10% water solution. Path ABCDEFGHI is the initial data taken with dry foam, and path A'B'C'D'E'F'G'H'I' is the data for a second cycle of immersion and withdrawal. (top). A schematic drawing of foam position relative to liquid level. (bottom)

The A’B’C’D’E’F’G’H’I’ path in Figure 5.4 is dynamic weight data for a second immersion and withdrawal from the solution. The starting foam weight was the final foam weight after the first cycle. Unlike the dry foam, the wet foam surface is wet by the solution, and therefore on immersion capillarity pulls the foam down, leading to a sudden measured weight increase at point B’. From Point B’ to C’, liquid climbs up the foam through porous structure due to capillary force. This effect increased the foam weight and it competed continuously with the buoyancy effect, which decreased the foam weight. Similar to the discussion above, this competition resulted in the roughness of curve B’C’. At point C’, the ¼ of the foam that is still above the liquid level is filled with the liquid, and hence the capillary driven flow disappeared. The weight decrease rate increased and the curve became smooth from point C’ to D’. By varying dip in speed, it was found that the ratio of the projected length of curve B’C’ to C’D’ on time axis increased with increasing speed. At point D’, the foam was totally immersed into the solution and the meniscus disappeared, which caused a steep weight decrease. Fewer air bubbles were trapped within the foam during this second immersion. From E’ to I’, the weight changes were similar to those for the first dip coating. These results indicated that the formation of a liquid layer on the foam in the initial dip coating step helped to diminish the trapped air bubbles but otherwise did not dramatically affect the amount of liquid retained in the foam after the dip coating cycle. For the experiments described below, the foams were immersed and withdrawn from the coating solution once before the main dip coating procedure.

Figure 5.5 shows the effect of withdrawal speed on the average coating thickness from dip coating of glycerol/water solutions onto 10PPI carbon foam. The data show that the thickness, h, increased with withdrawal speed, U, according to a power law with $h \mu U^n$. The power law exponent, n, increases from 0.18 to 0.32 as the glycerol concentration, and hence the viscosity, increases. In other words, the dependence of thickness on the withdrawal rate becomes steeper as the viscosity increases. In these experiments, the thickness is expected to vary indie the foam as the liquid distribution was not uniform, as discussed more below. Nevertheless, the average coating thickness provides a good measure of the amount of liquid trapped in the foam.

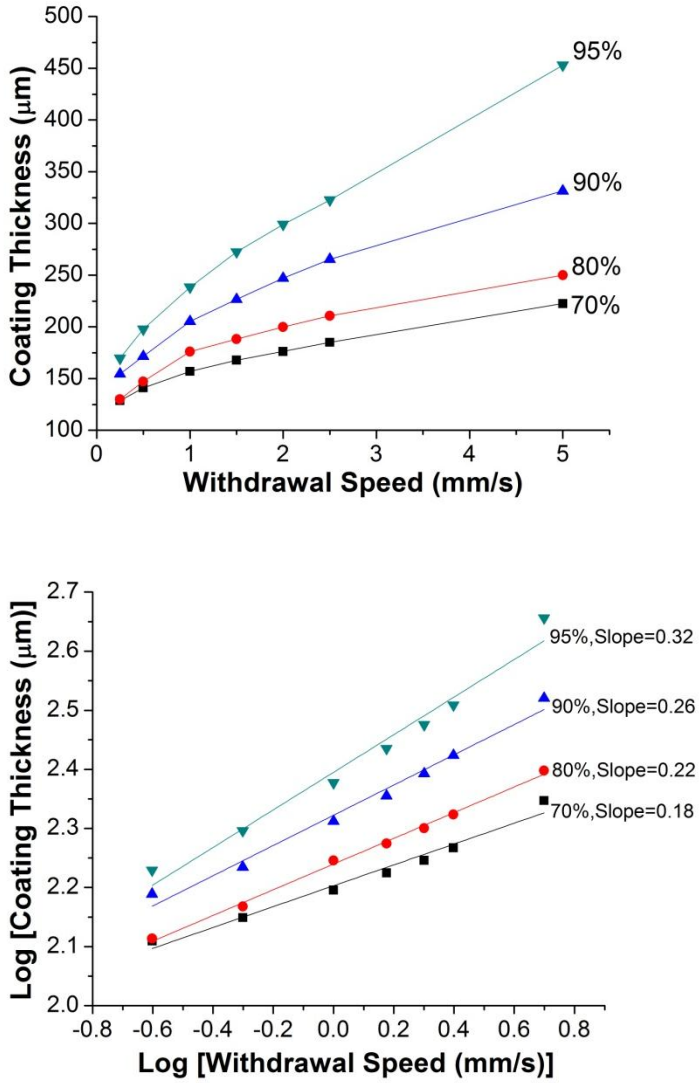

Figure 5.5 Effect of withdrawal speed on the average coating thickness from dip coating of glycerol/water solutions onto 10PPI carbon foam. Data are labeled with the wt% glycerol in the solution.

The effect of coating liquid viscosity on average coating thickness is shown in Figure 5.6. The average coating thickness also followed a power law relationship with viscosity, η, where $h \mu h^m$. The exponent m varies from 0.1 to 0.25 as withdrawal speed

increases. At lower withdrawal speeds, the thickness increase depends less on the solution viscosity.

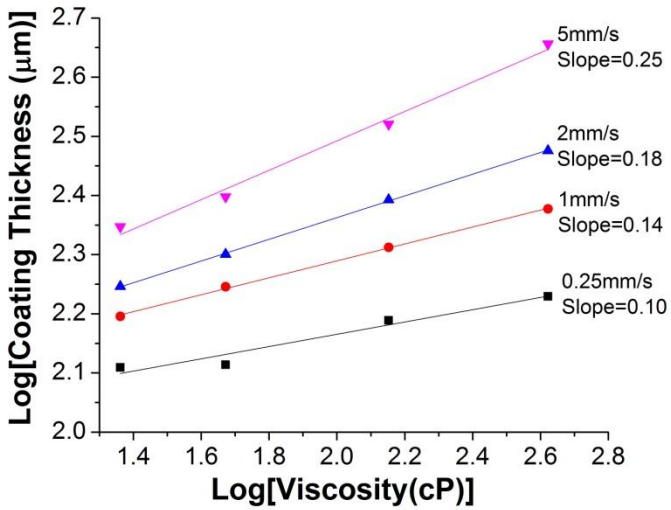

Figure 5.6 Effect of viscosity (in cP) on the average coating thickness from dip coating glycerol/water solutions onto 10 PPI carbon foam. Data are labeled with the withdrawal speed. The slope shown is the results from linear least squares fitting.

Data in Figure 5.5 and Figure 5.6 demonstrate that the amount of liquid deposited in the foam depends both on viscosity and the withdrawal rate, and that the effects of these two parameters are coupled. In the dip coating of a nonporous plate, the coating thickness is determined by the balance between viscous drag, which pulls liquid up with the moving substrate, and gravity and surface tension from the curved liquid-vapor meniscus, which both act in the opposite direction. The effect of viscosity and withdrawal speed on thickness is given by the Landau-Levitch equation[119]:

$$h = 0.94 \frac{(\eta U)^{2/3}}{\gamma^{1/6} (\rho g)^{1/2}} \tag{5.2}$$

For the open cell foam, the relationship between thickness and the process variables is complicated due to the internal structure, which influences the dynamics of the competing effects listed above. Viscous drag is responsible for pulling liquid upward and gravity causes a downward flow. However, the viscous drag effect, which is proportional to ηU, is not as strong in the coating of foam as compared with the flat plat, as evidenced by comparing the exponents in the power law relationships. The surface tension effect is more complex. Similar to the flat plate, there is an external liquid-vapor meniscus, which pulls liquid downward, but there are also a multitude of internal menisci that are more highly curved and trap liquid within the cells. In fact, contrary to the flat plat effect, lowering the surface tension of the coating solution by adding a surfactant leads to less liquid in the foam, a lower average thickness. See Figure 5.7. The rough surface of the foam may also play a role in pinning contact lines internally.

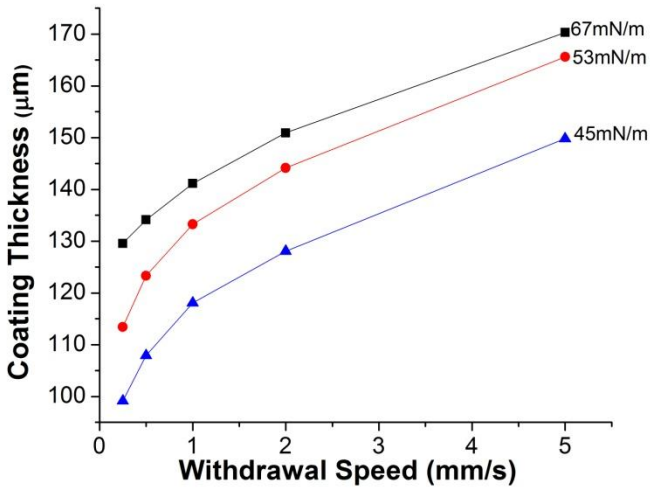

Figure 5.7 Effect of surface tension effect on the average thickness from dip coating of 70% glycerol/30% water solution of various surface tensions onto 30PPI carbon foam. Data are labeled with the surface tension of the solution.

Thickness trends for coatings on 30 PPI foam were the same as those shown for 10 PPI. See Figure 5.8. However, the average coating thickness deposited on the 30 PPI foam was less than that on the 10 PPI foam for a given coating liquid and withdrawal rate. The difference became more apparent as the withdrawal rate increased. The 30 PPI foams had both smaller cell and pore sizes, and smaller strut dimensions (see Figure 5.1 for structural features). The origin of the pore size effect requires more investigation but could be related to the strut dimension. The thickness of coatings on fibers decreases as the fiber radius decreases due to the influence of the meniscus curvature.[120] By analogy, the thickness on the thinner struts of the 30 PPI foam is less than that on the thicker struts of the 10 PPI foam. For foams with much higher PPI values and smaller pore sizes, such as 80 PPI foam, the hydrophobic surface of the carbon causes problems. Air bubbles are trapped into the pores and the foam floats on the surface of the coating solution. In this case, nitric acid surface functionalization treatment [121] can be used to make carbon foam surface hydrophilic.

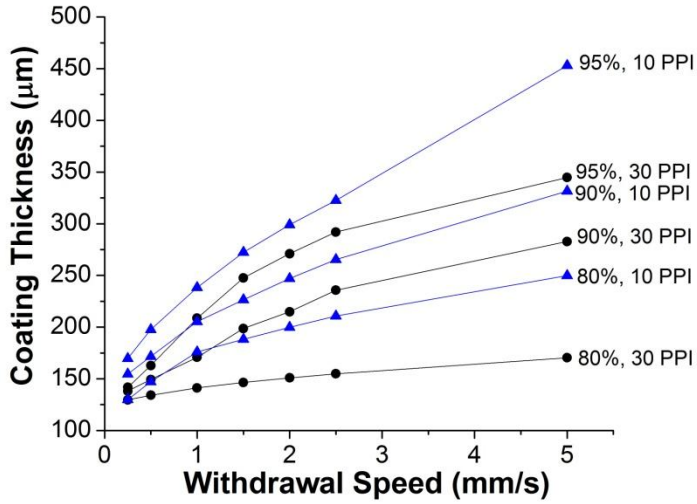

Figure 5.8 Effect of withdrawal speed on the average coating thickness from dip coating of glycerol/water solutions onto 10 PPI and 30 PPI carbon foam. Data are labeled with the % glycerol in the solution and the pore content of the foam.

One important advantage of open celled carbon foam is its low pressure drop due to its large quantity of void space. However, visual observations indicated that some of the glycerol/water solution was trapped in the voids of the foam after dip coating process. To further investigate this phenomenon, a dispersion of 10wt% boehmite in water was used as the coating solution. After the foam was completely withdrawn from the solution, excess liquid was observed to be trapped in the foam pores. During drying, some trapped liquid drained to the bottom part of the foam due to gravity, and some was retained as a thin film that covered the circular windows that connect the cells. See Figure 5.9. After drying, solidified films block the pores and potentially degrade properties. Varying the dip coating speed (i.e., lowering the speed) did not improve the situation. Therefore, dip

coating alone is not an effective coating technique and it is important to remove the trapped liquid.

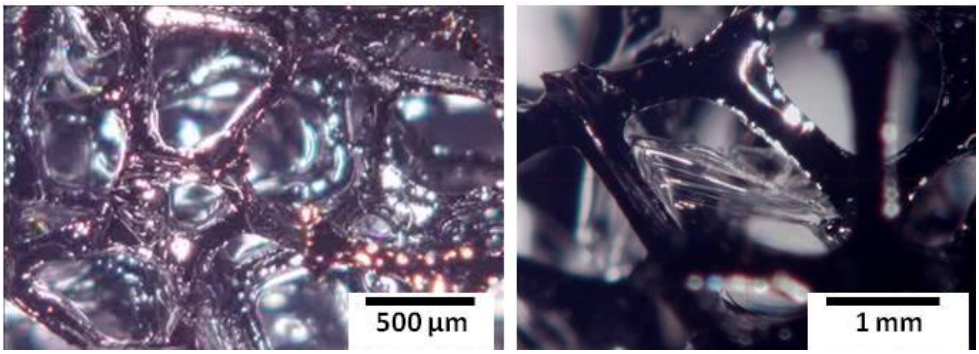

Figure 5.9 Optical images of Excess liquid trapped in the pores of carbon foam (left). A solidified film formed on the pore window (right).

5.3.2 Spin treatment

Figure 5.10 shows the effect of initial average coating thickness after dip coating on the average coating thicknesses after the spin coating treatment. The initial average coating thickness, calculated with equation (1), was varied coating at different withdrawal speeds. The dip coated foams were then spin treated at 1500 rpm for 30 seconds. After spinning, the foam was weighed to calculate the final coating thickness, again based on equation (1). The result shows that the final coating thickness was independent of the initial liquid load or the dip coating withdrawal speed. This independence required that the spinning speed and time be above a critical level. For example, the critical spin speed and time combination for 90% glycerol solution was determined to be 1500 rpm and 30 seconds. Because the exact amount of liquid initially loaded into the foam by dip coating was not important to the final amount of liquid on the foam, a simple dip coating by hand procedure was used in spin treatment study.

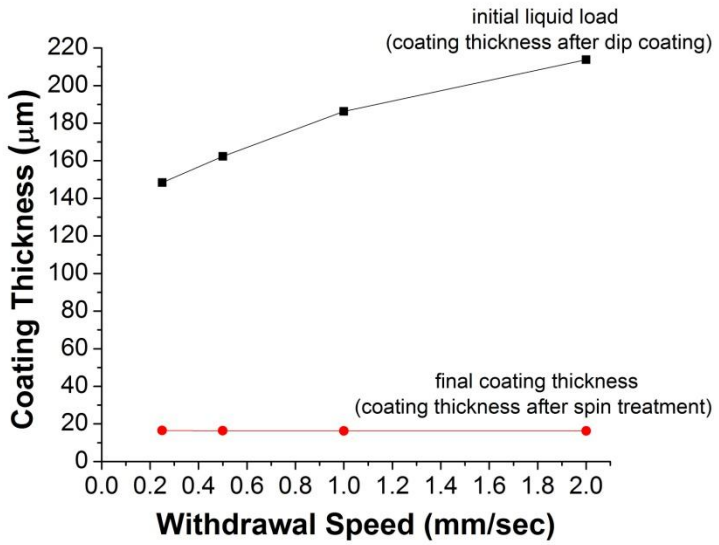

Figure 5.10 Effect of initial liquid load on final coating thickness for 30 PPI carbon foam dip coated with 90% glycerol 10% water at various withdrawal speeds and spin treated at speed of 1500 rpm for 30 seconds.

Figure 5.11 shows the effect of spin time on coating thickness for 30 PPI carbon foam coated with 100% glycerol and 80% glycerol/20% water solution at various spin speeds. The coating thickness decreased with increasing spin time initially, but after about 60s, the thickness decrease slowed down and started to flatten out.

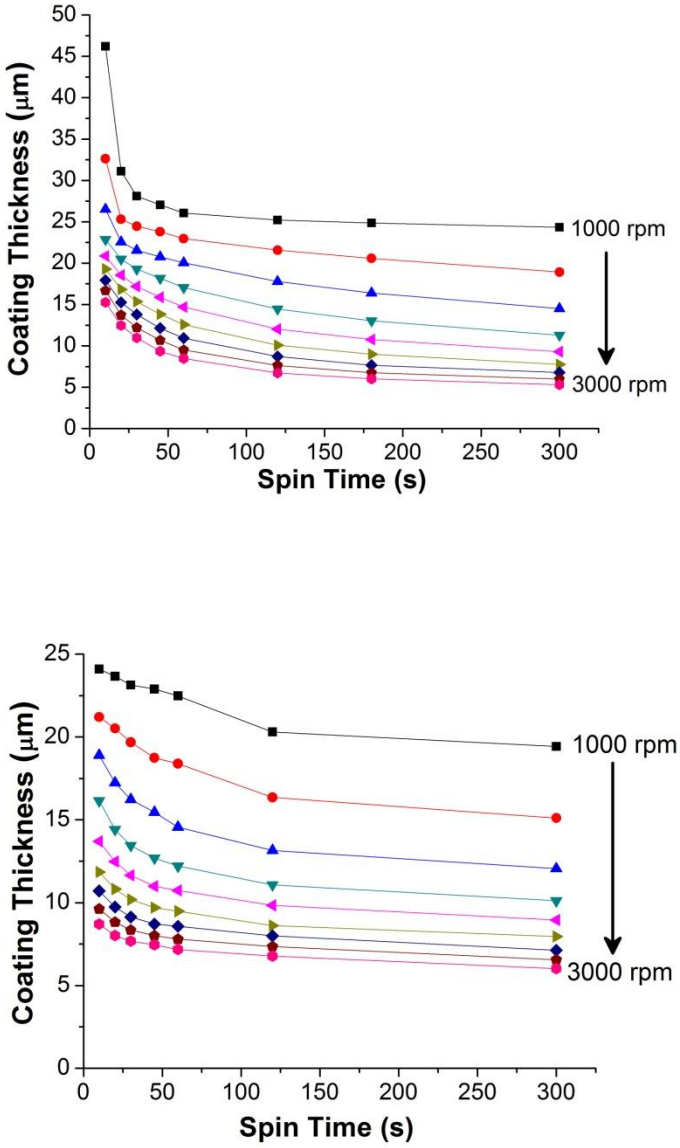

Figure 5.11 Effect of spin time on coating thickness for 30 PPI carbon foam dip coated with 100% glycerol (above) and 80%glycerol 20%water (below) and spin treated at speeds from 1000 rpm to 3000 rpm with each increment of 250 rpm.

The relationship between coating thickness and spin time for the foam coating is similar to that for spin coating on a flat surface.[122] In spin coating of a flat substrate, the

substrate is flooded with excess liquid; this liquid is removed very quickly in a surge as the spinning begins. The pockets of excess liquid in the foam should likewise be susceptible to fast removal by centrifugal forces. Then as the data shows, the coating thins quickly at first and then more slowly during the 'spin-off' stage. In spin coating of a flat substrate, this stage involves centrifugal forces driving the liquid outward and resistance from viscous forces in the thin liquid layer. The coating thins and approaches a nearly constant value, because the resistance to flow increases as the thickness decreases. Eventually, flow essentially stops for all practical purposes. (In real coatings, drying influences this stage and arrests the flow.) This final thickness is smaller for higher spinning rates and lower viscosity liquids. The same factors appear to be at work in the spinning of foams. There is a quick and then gradual thinning with time for both coating liquids shown in Figure 11 with the more viscous liquid creating thicker coatings for a given spin speed. The intricate structure of the foam should also enter into liquid flow during spinning though the data do not elucidate these effects.

Figure 5.12 shows the effect of spin speed and solution viscosity on coating thickness for 30PPI carbon foam dip coated with 80% (low viscosity) and 100% (high viscosity) glycerol and spin treated for 2 minutes. The coating thickness decreases with increasing spin speed for solutions with both high and low viscosity liquids. The linear fit to the log (thickness)-log(speed) plot is similar to that found for spin coating of flat substrates.[123] For these model coating liquids, the final coating thickness should trend toward the same value. Evaporation from the 80% glycerol/20% water solution would cause this layer to become similar in viscosity to the 100% glycerol layer; therefore given

enough time, the two coatings should meet the same limitation in thickness due to the viscous resistance to flow. At the slower speeds in Figure 5.12, two minutes appears not to be long enough for the coatings to reach this stage, but at the faster speeds, both coatings reach about the same thickness.

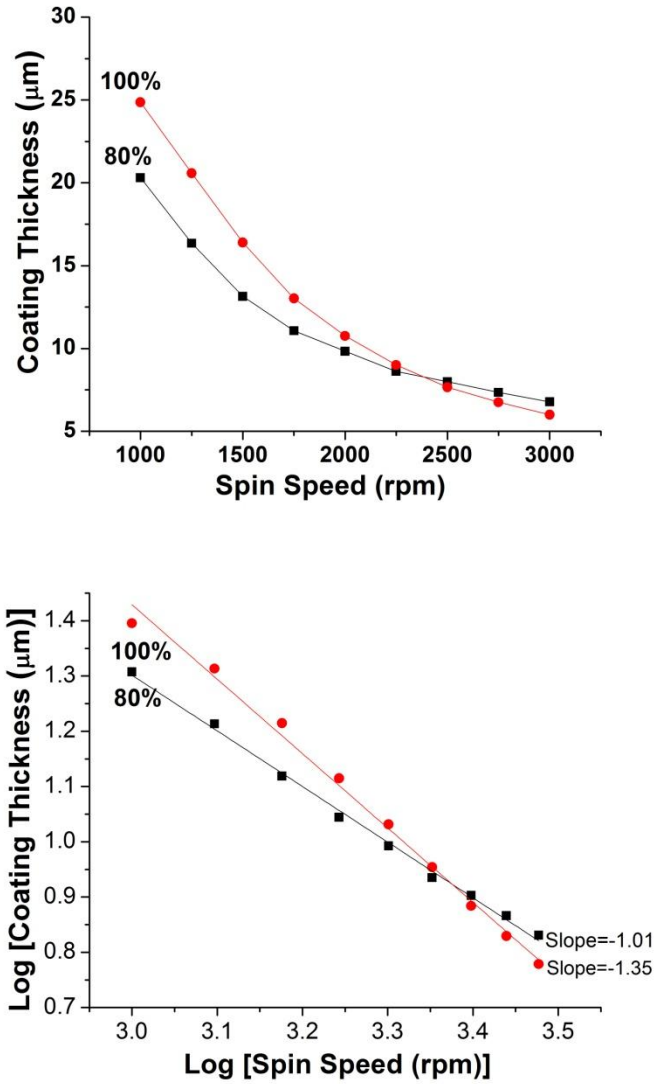

Figure 5.12 Effect of spin speed and solution composition on the coating thickness from spinning 30PPI carbon foams. Data are label with the % glycerol. The spin time is 120 seconds and the slope shown is determined by linear least squares fitting.

Figure 5.13 shows the coating thickness ratio of 10 PPI to 30 PPI carbon foam after spinning with 80% glycerol solution. The data show that average thickness of the coating on 10 PPI carbon foam was more than twice that on 30PPI carbon foam at various spin time and speed combinations, but the differences between 20 PPI and 10 PPI were less. Interestingly, this result is similar to the differences noted in dip coating and again, a possible reason for coating thickness difference might be the difference in strut diameter.

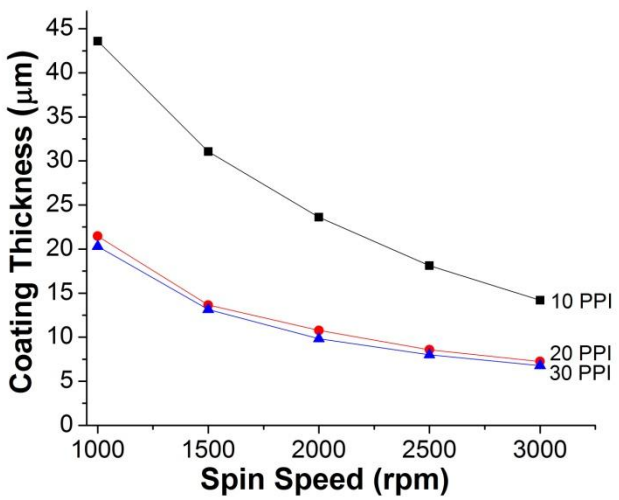

Figure 5.13 Effect of spin speed on the average coating thickness for spin coating of 80% glycerol/20% water solution onto 10, 20 and 30 PPI carbon foams. The spinning time was 120 s.

5.3.3 Alumina and zeolite coatings

The dip and spin coating process was used to create alumina and zeolite coatings on carbon foam. The process was carried out in the same way as glycerol/water solution. Figure 5.14 shows that a relatively uniform coating formed on the internal surface of the

carbon foam after drying. Based on cross section image, the coating thickness at the edge of the foam was similar to that in the center. Spin coating theory for flat surface claims that the coating thickness is independent on the location of the substrate.[123] This characteristic seems also to be true for foam structure. The flux due centrifugal force is proportional to the distance from the spin center. However, the liquid volume that needs to be removed at certain point is also proportional to the distance from the spin center. Therefore, the coating thickness at the foam edge is similar to that at the center of the foam. However, thickness uniformity was only demonstrated on a 2” x 2” x 0.8” foam and more work is needed to explore uniformity on larger pieces.

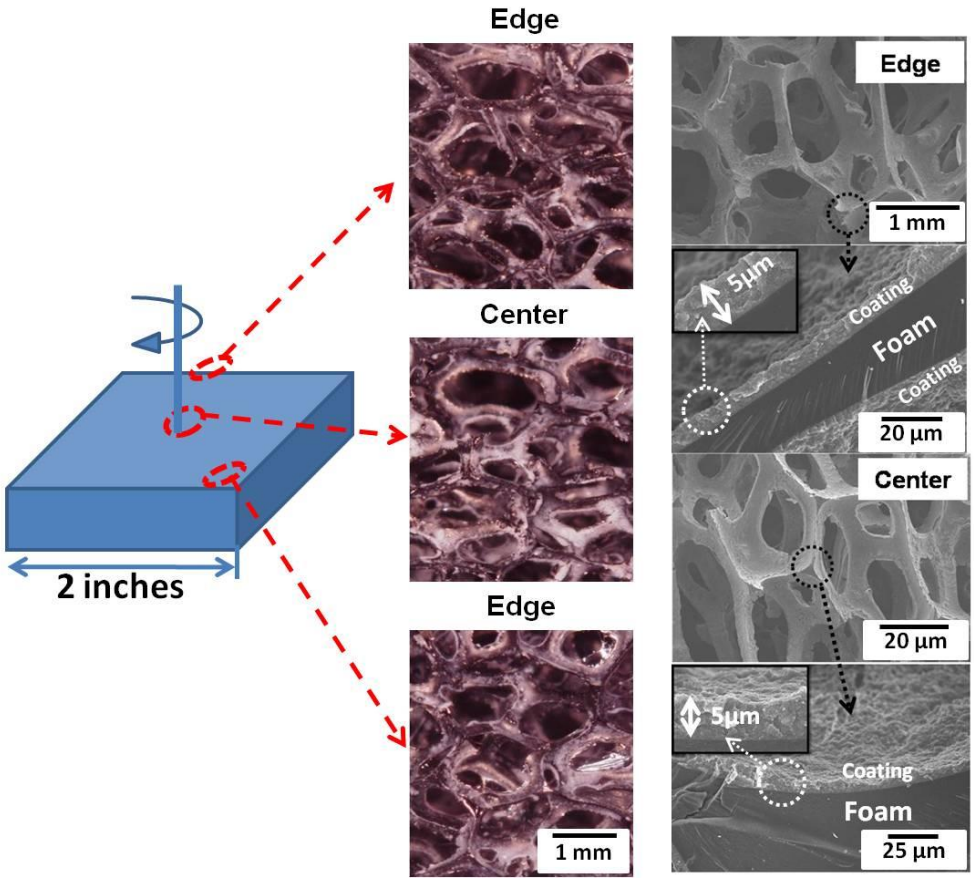

Figure 5.14 Optical micrographs (left) and SEM top view and cross section (right) of alumina coating onto carbon foam with spin treatment. (2000 rpm; 30 secs)

Although the average coating thickness was relatively uniform over the foam macroscopically, the coating thickness varied microscopically. One example of local coating thickness variation at the edge of one strut is shown in Figure 5.15. For catalytic applications, nonuniformities on this level are not likely to cause performance problems. Uneven coatings have also been observed in coatings prepared in monolith channels.[124] Multiple depositions were needed to build up the coating thickness. A reasonable washcoat thickness for catalytic applications is about 10-100 μm.[124] However, due to cracking, multiple depositions were needed to build up the coating thickness for real catalytic application. Figure 5.15 is a high magnification SEM image of the alumina coating on a foam strut after three depositions and calcinations.

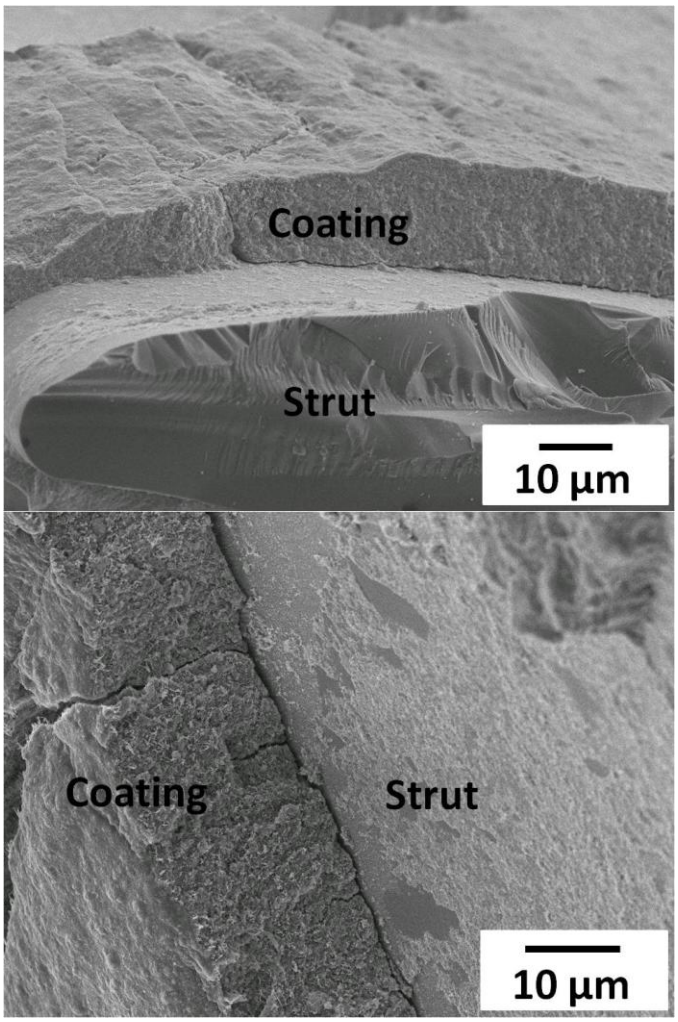

Figure 5.15 SEM micrographs of alumina coatings using three depositions and calcinations on 30 PPI carbon foam: variation in coating thickness near the edge of a strut (left) and coating thickness at the center of the strut (right).

Lastly, the dip and spin process was used to create coatings of exfoliated zeolite on alumina open cell foam supports. The alumina support was chosen because it is compatible with the catalytic tests. Figure 5.16 shows a continuous zeolite coating composed of nanosized exfoliated sheets on the foam surface. The coating was quite uniform over the foam surface.

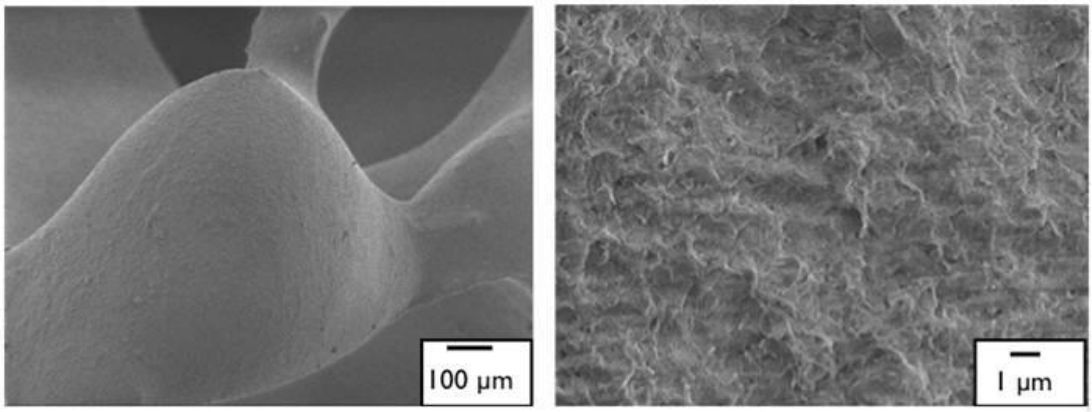

Figure 5.16 SEM micrographs of the exfoliated MCM-22 zeolite coating on the alumina foam. Low magnification (left) and high magnification (right).

In summary, a systematic study of coating onto open celled foam has been carried out. While the dip coating process allows for a controlled amount of liquid to be deposited in the foam, the uniformity is not sufficient even at low dip coating speeds. Therefore a two step treatment is used to create uniform coatings. In the first step dip coating is used to load liquid into the foam, and in the second step a spin treatment removes the excess trapped liquid and redistributes the liquid to form a uniform coating over the internal surface of the foam. Although the foam structure is quite complex, the relationship between the coating thickness and experimental variables remains relatively simple and predictable. The coating process was successfully applied to form alumina coatings onto carbon foams and zeolite coatings onto alumina foams for catalytic applications.

Chapter 6 Summary

First part of the thesis (Chapter1-4) covers the study of salt crystal whisker growth on solution saturated nanoporous coating.

Salt crystal whiskers were formed using nanoporous coatings as a platform for growth. The nanoporous coating was dip coated onto substrate from colloidal silica solution and the whisker growth was carried out in a relative humidity controlled environment. The steps in the growth process were established by characterizing the effects of solution concentration and relative humidity on growth. A visualization method was used to track liquid front rise in the porous coating, and to study the liquid transport phenomenon. The results showed that solution was pulled into the porous coating by capillarity; concurrent evaporation led to building of concentration in the pore liquid and a whisker growth zone where the concentration reached a critical level for formation of salt crystals. Calculation of balance between capillary driven flow and water evaporation flux showed that the rise of salt solution in the porous coating was much higher than that of pure water and this suggested that local crystallization in the pores might helped to raise the liquid front. The Peclet number was also calculated and confirmed that salt ions supersaturation could be reached at the growth zone for whisker growth. The effect of relative humidity and salt concentration on whisker growth results squared with the theoretical calculation of liquid transport.

A whisker base growth mechanism was then proposed based on the experimental results. Whisker growth occurred by ion addition to the crystal surface that was in contact with the porous coating. This growth mechanism also explained the formation of sheet-like crystal observed in experiments.

Effects of other experimental variables on whisker growth were also studied. The effect of porous coating thickness on whisker growth showed that whisker quantity increased with increasing coating thickness. The study of porous coating particle size effect indicated that whisker lateral size depended on the size of the coating particle. The study of whisker growth angle demonstrated that whiskers could grow and stood perpendicular to the porous coating at any growth angle. This indicates the existence of liquid layer at the whisker base during growth, and this liquid layer supplies salt ion for continuous whisker growth and provides support to keep whisker standing. The calculation of force and torque balance was also carried out and it confirmed that the support from the liquid layer at the whisker base was sufficient to provide stability during whisker growth and tilt. Cryo SEM was also used to study whisker growth and it also indicated the existence of the liquid layer at whisker base.

A new free particle method was developed for whisker growth. Copious amounts of whiskers were generated from a salt solution containing nanoparticles in contact with a bare substrate under controlled relative humidity conditions. Whiskers grew on the self-assembled nanoporous coating formed on the bare substrate. Here, the step of capillary flow into the coating was eliminated and growth occurs rapidly, apparently by the same growth mechanism.

Inspired by the liquid transport and the crystal sheet growth mechanism, two strategies were investigated to reduce the lateral dimension of whisker. Firstly, a patterned substrate with coated and uncoated stripes was used to limit liquid supply during whisker growth. However, because of the technical difficulty to reduce pattern size to nanometer scale, the whisker width was not significantly reduced. Secondly, finely ground salt particle was used as seeds to initiate simultaneous whiskers growth. With proper seed concentration and proper porous coating, the whisker width was successfully reduced to as small as 50 nm.

While this research project focused mainly on KCl, this whisker growth method could also be adapted to create whisker and sheet from other water soluble materials, such as NaCl and KBr.

The second part of the thesis (Chapter 5) covered the research project of coating onto open celled foam. The open celled foam is a type of solid foam with interconnected pore structure and has various applications including heat exchanger, energy absorber and structured catalyst support. The properties of the solid foam could be improved and altered by adding a coating to deliver multifunctional characteristics. However, it is difficult to get controllable, repeatable and uniform coating onto 3 dimensional foam structures by conventional coating process. A systematic study of coating onto open celled foam was carried out and a noval two step coating process that combined dip coating and spin treatment was developed. Dip coating is used to load liquid into the foam and the spin treatment is used to remove the excess trapped liquid and redistribute the liquid to form a uniform coating over the internal surface of the foam. Although the foam structure is quite complex, the relationship between the coating thickness and

experimental variables remains relatively simple. The coating process has been successfully applied to form alumina coating onto carbon foam and zeolite coating onto alumina foam for catalytic applications.

References

1. F.R.N. Nabarro and P.J. Jackson. "Growth of crystal whiskers," Growth and perfection of crystals, Proceedings of the international conference on crystal growth.,Cooperstown, NY: John Wiley & Sons, 14-98 (1958).

2. A.P. Levitt, "Whisker Technology," Wiley- Interscience, New York, 1970, (1970).

3. S.S. Brenner, "Properties of Whiskers," Growth and perfection of crystals, Proceedings of the international conference on crystal growth.,Cooperstown, NY: John Wiley & Sons, 157-90 (1958).

4. W.V. Fred, "Electroplated Tin and Tin Whiskers in Lead Free Electronics," (2004).

5. G. Turchanyi, T. Horvath and I. Tarjan. "Sodium Chloride Whiskers," Nature, 193, 867-8 (1962).

6. C C Evans, *Whiskers;* pp. 71. Mills & Boon Limited, London, 1972.

7. N. Kato, "Fibrous growth of NaClO3 on single crystal," Journal of the Physical Society of Japan, 10, 1024-5 (1955).

8. M. Hayashi and T. Shichiri. "Theoretical and experimental study of the growth of perfect cyrstals," Journal of Crystal Growth, 21, 254-60 (1974).

9. P. Charsley and P.E. Rush. "The growth of inorganic salt whiskers from solution," Philosophical Magazine, 3, 508-12 (1958).

10. B.E. Powell and B.M. McKibben. "Alkali halide filamentary crystals," Journal of Crystal Growth, 8, 276-8 (1971).

11. B.E. Powell, "L-Alanine filamentary crystals." Journal of Crystal Growth, 18, 307-8 (1973).

12. H.A. Fells and J.B. Firth. "Some Observations on the Preparation and Properties of Silicic Acid Gel," Journal of Physical Chemistry, 29, 241-8 (1925).

13. W.S. Hinegardner, "Needle-shaped crystals of Sodium Chloride," Journal of the Amercian Chemical Society, 55, 1461-2 (1933).

14. P.J. Shlitchta, "Comparison of copper whiskers with ultrafine wires," Growth and perfection of crystals, Proceedings of the international conference on crystal growth.,Cooperstown, NY: John Wiley & Sons, 214-8 (1958).

15. C.G. Herring J.K., Phys Rev, 85, 1060 (1952).

16. Masanori N. Mitsunori S., "Superconducting properties of single-crystal whiskers of $(Y_{0.86}Ca_{0.14})Ba_2Cu_3O_x$ grown from precursors containing calcium and tellurium," Applied physics letters, 82, 1899-901 (2003).

17. P.W. Julio d.P. Atkins, *Physical Chemistry;* W. H. Freeman, NEW YORK, 2002.

18. Bush science department, "Solubility and Solutions," 2010, (2004).

19. J.S. Langer, "Instabilities and pattern formation in crystal growth," Reviews of Modern Physics, **52,** 1-28 (1980).

20. J.W. Mullin, *Crystallization (4th Edition) BOOK;* Oxford; Boston : Butterworth-Heinemann, 2001.

21. l. Tarjan and M. Matrai. "Laboratory manual on crystal growth," Akademiai Kiado, Budapest 1972, (1972).

22. J.C. Brice, "The growth of crystals from liquids (Book)," American Elsevier Publishing Co. Inc., New York, 1973, (1973).

23. F.C. Frank, "The influence of dislocations on crystal growth," Discuss. Faraday Soc., 5, 48-54 (1949).

24. G.W. Sears, "A mechanism of whisker growth," Acta Metallurgica, 3, 367-9 (1955).

25. S. Amelinckx, "Growth of alkali halide whiskers from solution," Physica (The Hague), 24, 390-2 (1958).

26. R.J. Davey, J.W. Mullin and M.J.L. Whiting. "Habit modification of succinic acid crystals grown from different solvents," Journal of Crystal Growth, 58, 304-12 (1982).

27. G.L. Kenneth, "Snowflake," <www.snowcrystals.com> (2007).

28. Y.M. Yang S., "Atomicstic nature of NaCl nucleation at the solid liquid interface," The journal of chemical physics, 126, 044708 (2007).

29. Y.M. Yang S., "Dissolution dynamics of NaCl nanocrystal in liquid water," Physical Review E, 72, 012602-1,012602-4 (2005).

30. D. Zahn, "Atomicstic mechanism of NaCl nucleation from an aqueous solution," Physica Review Letter, 92, 040801-1,040801-4 (2004).

31. H.S. Shinto T., "Free energy profiles for Na^+ and Cl^- adsortpion onto water/NaCl crystal interfaces evaluated by molecular dynamics simulation," Jouranl of chemical engineering of Japan, 31, 771-9 (1998).

32. R. Schmidt, Diss Kiel Halle, (1911).

33. W. Zhen, "Presentation and dossier of whisker growth on porous substrate," Dossier (2003).

34. T. Shichiri and N. Kato. "The growth and dissolution of NaCl whiskers in aqueous solution," Acta Metallurgica, 13, 785-96 (1965).

35. T. Shichiri, "Growth mechanism of sodium chloride whiskers," Journal of Crystal Growth, 24-25, 350-3 (1974).

36. N. Yellin, L. Ben-dor and N. Zelingher. "Whisker growth by means of porous glass," J. Mater. Sci., 21, 2648-50 (1986).

37. N. Yellin, N. Zelingher and L. BenDor. "CA membranes as habit modifiers for the growth of whiskers of inorganic salts," J. Mater. Sci., 21, 504-6 (1986).

38. R. Ueda, M. Ono and F. Tokugawa. "Growth, morphology, and twisting of whiskers of some water-soluble ferroelectric crystals," Journal of Physics and Chemistry of Solids, Supplement, 381-4 (1967).

39. G.W. Sears, "Fibrous growth of sodium chlorate," Journal of Chemical Physics, 26, 1549-52 (1957).

40. K. Ali, A.A. Shah, S. Bilal and A.A. Shah. "Surface tensions and thermodynamic parameters of surface formation of aqueous salt solutions: III. Aqueous solution of KCl, KBr and KI," Colloids Surf. Physicochem. Eng. Aspects, 337, 194-9 (2009).

41. T. Matsumoto, "Growth of sodium chloride whiskers from aqueous solution," Kogakuin Daigaku Kenkyu Hokoku, 17, 32-7 (1965).

42. G. Matthai and G. Syrbe. "Whisker growth of alkali halides," Z. Naturforsch, 12a, 174 (1957).

43. S. Iijima, "Carbon nanotube," Nature, 354, 56 (1991).

44. I.S. Evans, "Salt Crystallization and Rock Weathering: A Review," Revue de Geomorphologie Dynamique, 19, 155-77 (1970).

45. C. Rodriguez-Navarro and E. Doehne. "Salt weathering: Influence of evaporation rate, supersaturation and crystallization pattern," Earth Surf. Process. Landforms, 24, 191-209 (1999).

46. R.J. Flatt, "Salt damage in porous materials: how high supersaturations are generated," J. Cryst. Growth, 242, 435-54 (2002).

47. P. Theoulakis and A. Moropoulou. "Salt crystal growth as weathering mechanism of porous stone on historic masonry," Journal of Porous Materials, 6, 345-58 (1999).

48. M. Steiger, "Crystal growth in porous materials-I: The crystallization pressure of large crystals," J. Cryst. Growth, 282, 455-69 (2005).

49. G.W. Scherer, R. Flatt and G. Wheeler. "Materials science research for the conservation of sculpture and monuments," MRS Bulletin, 26, 44-50 (2001).

50. S.Z. Lewin and A.E. Charola. "Aspects of crystal growth and recrystallization mechanisms as revealed by scanning electron microscopy," Scan. Electron Microsc., 551-8 (1980).

51. A.E. Charola and S.Z. Lewin. "EFFLORESCENCES ON BUILDING STONES - SEM IN THE CHARACTERIZATION AND ELUCIDATION OF THE MECHANISMS OF FORMATION," Scan. Electron Microsc., 379-86 (1979).

52. S.Z. Lewin, "the Mechanism of Masonry Decay through Crystallization," Conservation of Historic Stone Buildings and Monuments, 120-44 (1982).

53. A.S. Goudie, "Salt weathering simulation using a single-immersion technique," Earth Surf. Process. Landforms, 18, 369- (1993).

54. Y.T. Puyate and C.J. Lawrence. "Wick action at moderate Peclet number," Phys. Fluids, 10, 2114- (1998).

55. Y.T. Puyate, C.J. Lawrence, N.R. Buenfeld and I.M. McLoughlin. "Chloride transport models for wick action in concrete at large Peclet number," Phys. Fluids, 10, 566- (1998).

56. Y.T. Puyate and C.J. Lawrence. "Wick action at moderate Peclet number," Phys. Fluids, 10, 2114-16 (1998).

57. D.D. Brewer, J. Allen, M.R. Miller, et al. "Mechanistic principles of colloidal crystal growth by evaporation-induced convective steering," Langmuir, 24, 13683-93 (2008).

58. S. Amelinckx, "Mechanism for the growth of whiskers from solution on an impervious substrate," J. Chem. Phys., 31, 1687-8 (1959).

59. P.C. Hiemenz and R. Rajagopalan. *Principles of Colloid and Surface Chemistry;* New York : Marcel Dekker, 1997.

60. N. Fries, K. Odic, M. Conrath and M. Dreyer. "The effect of evaporation on the wicking of liquids into a metallic weave," J. Colloid Interface Sci., 321, 118-29 (2008).

61. W.L. McCabe and J.C. Smith. *Unit Operations of Chemical Engineering;* Boston: McGraw-Hill, 2005.

62. H. Zhang and S. Han. "Viscosity and density of water+sodium chloride+potassium chloride solutions at 298.15 K," J. Chem. Eng. Data, 41, 516-20 (1996).

63. D.R. Lide, "CRC Handbook of Chemistry and Physics," (2008).

64. E.R. Washburn, "The creep of solutions," J. Phys. Chem, 31, 1246-8 (1927).

65. G.W. Scherer, "Crystallization in pores," Cem. Concr. Res., 29, 1347-58 (1999).

66. N. Shahidzadeh-Bonn, S. Rafai, D. Bonn and G. Wegdam. "Salt crystallization during evaporation: Impact of interfacial properties," Langmuir, 24, 8599-605 (2008).

67. T. Shichiri, "Growth and observation of sodium chloride whisker," Kotai Butsuri, 8, 561-5 (1973).

68. G.W. Scherer, "Structure and properties of gels," Cement and Concrete Research, 29, 1149-57 (1999).

69. S. Taber, "The origin of veins of the asbestiform minerals," Proceedings of the national academy of sciences, 2, 659-64 (1916).

70. T. Shichiri and N. Kato. "Regrowth of NaCl whiskers from pure and poisoned solutions," J. Cryst. Growth, 3-4Spe, 384-90 (1968).

71. T. Shichiri, H. Kinoshita and N. Kato. "Regrowth of NaCl and KCl whiskers in aqueous solution," Journal of the Physics and Chemistry of Solids, 385-8 (1967).

72. S. Amelinckx, "Dislocation patterns in potassium chloride," Acta Metallurgica, 6, 34-58 (1958).

73. P. Bennema, G. Bogels, D. Bollen, T. Mussig and H. Meekes. "Crystal surfaces and crystal growth mechanisms: application to crystals having the NaCl structure and especially silver halide crystals," Imaging Science Journal, 49, 1-32 (2001).

74. J.H. Zhang, P. Zhan, Z.L. Wang, W.Y. Zhang and N.B. Ming. "Preparation of monodisperse silica particles with controllable size and shape," J. Mater. Res., 18, 649-53 (2003).

75. D. Quere and H. Di Neglio. "Meniscus on a fibre," Adv. Colloid Interface Sci., 48, 141-50 (1994).

76. M. Law, J. Goldberger and P. Yang. "Semiconductor nanowires and nanotubes," Annual Review of Materials Research, 34, 83-122 (2004).

77. T. Shichiri, H. Kinoshita and N. Kato. "Regrowth of NaCl and KCl whiskers in aqueous solution," Journal of the Physics and Chemistry of Solids, 385-8 (1967).

78. S. Amelinckx, "Decoration of dislocations in alkali halide whiskers," J. Appl. Phys., 29, 1610-1 (1958).

79. T.D. Reynolds, S.K. Kalpathy, S. Kumar and L.F. Francis. "Dip coating of charged colloidal suspensions onto substrates with patterned wettability: Coating regime maps," J. Colloid Interface Sci., 352, 202-10 (2010).

80. C.B. Murray, C.R. Kagan and M.G. Bawendi. "Synthesis and characterization of monodisperse nanocrystals and close-packed nanocrystal assemblies," Annual Review of Materials Science, 30, 545-610 (2000).

81. S. Sarig, A. Glasner, J.A. Epstein and N. Eidelman. "Growth of potassium chloride crystals," J. Cryst. Growth, 39, 255-66 (1977).

82. T. Annen and M. Epple. "A facile synthesis of dispersable NaCl nanocrystals," Dalton Transactions, 9731-4 (2009).

83. C.W. Harmon, R.L. Grimm, T.M. Mclntire, et al. "Hygroscopic Growth and Deliquescence of NaCl Nanoparticles Mixed with Surfactant SDS," J Phys Chem B, 114, 2435-49 (2010).

84. M.J. Bierman, Y.K.A. Lau, A.V. Kvit, A.L. Schmitt and S. Jin. "Dislocation-driven nanowire growth and Eshelby twist," Science, 320, 1060-3 (2008).

85. S.A. Morin, M.J. Bierman, J. Tong and S. Jin. "Mechanism and kinetics of spontaneous nanotube growth driven by screw dislocations," Science, 328, 476-80 (2010).

86. N.W. Moore, J. Luo, J.Y. Huang, S.X. Mao and J.E. Houston. "Superplastic nanowires pulled from the surface of common salt," Nano Letters, 9, 2295-9 (2009).

87. R. Baughman, A. Zakhidov and W. de Heer. "Carbon nanotubes - the route toward applications," Science, 297, 787-92 (2002).

88. T. Hayashi and M. Endo. "Carbon nanotubes as structural material and their application in composites," Compos. Pt. B-Eng., 42, 2151-7 (2011).

89. G.K. Mor, O.K. Varghese, M. Paulose, K. Shankar and C.A. Grimes. "A review on highly ordered, vertically oriented TiO2 nanotube arrays: Fabrication, material properties, and solar energy applications RID B-9455-2009," Solar Energy Mater. Solar Cells, 90, 2011-75 (2006).

90. A. Bianco, K. Kostarelos and M. Prato. "Applications of carbon nanotubes in drug delivery," Curr. Opin. Chem. Biol., 9, 674-9 (2005).

91. V. Popov, "Carbon nanotubes: properties and application," Mater. Sci. Eng. R-Rep., 43, 61-102 (2004).

92. K. Peng, Y. Xu, Y. Wu, Y. Yan, S. Lee and J. Zhu. "Aligned single-crystalline Si nanowire arrays for photovoltaic applications," Small, 1, 1062-7 (2005).

93. Q. Hou, D.W. Grijpma and J. Feijen. "Porous polymeric structures for tissue engineering prepared by a coagulation, compression moulding and salt leaching technique." Biomaterials, 24, 1937-47 (2003).

94. N.C. Gallego and J.W. Klett. "Carbon foams for thermal management," 41, 1461-6 (2003).

95. M. Calvo, A. Arenillas, R. Garcia and S.R. Moinelo. "Growth of carbon nanofilaments on coal foams," Fuel, 88, 46-53 (2009).

96. K. Kobashi, T. Tachibana, C. Ichihara and A. Kobayashi. "Electron field emission from diamond-coated carbon foam," Diamond and Related Materials, 18, 1081-4 (2009).

97. P. Chin, X. Sun, G.W. Roberts and J.J. Spivey. "Preferential oxidation of carbon monoxide with iron-promoted platinum catalysts supported on metal foams," Applied Catalysis A: General, 302, 22-31 (2006).

98. L. Giani, G. Groppi and E. Tronconi. "Mass-transfer characterization of metallic foams as supports for structured catalysts," Industrial and Engineering Chemistry Research, 44, 4993-5002 (2005).

99. F. Scheffler, R. Herrmann, W. Schwieger and M. Scheffler. "Preparation and properties of an electrically heatable aluminium foam/zeolite composite," Microporous and Mesoporous Materials, 67, 53-9 (2004).

100. Y. Peng and J.T. Richardson. "Properties of ceramic foam catalyst supports: One-dimensional and two-dimensional heat transfer correlations," Applied Catalysis A: General, 266, 235-44 (2004).

101. M.V. Twigg and J.T. Richardson. "Theory and applications of ceramic foam catalysts," Chem. Eng. Res. Design, 80, 183-9 (2002).

102. M.V. Twigg and J.T. Richardson. "Fundamentals and applications of structured ceramic foam catalysts," Industrial and Engineering Chemistry Research, 46, 4166-77 (2007).

103. E.J.A. Pope, A. Almazan and K. Kratsch. "Caged alumina particles in reticular foam," J Am Ceram Soc, 74, 2715-17 (1991).

104. Y. Kawai, G.D. Alton and J.-. Bilheux. "An inexpensive and fast method for infiltration coating of complex geometry matrices for ISOL production target applications," Nuclear Instruments & Methods in Physics Research, Section B (Beam Interactions with Materials and Atoms), 241, 991-5 (2005).

105. P.W.A.M. Wenmakers, D.S. Van, B.F.M. Kuster and J.C. Schouten. ""Hairy Foam": Carbon nanofibers grown on solid carbon foam. A fully accessible, high surface area, graphitic catalyst support," Journal of Materials Chemistry, 18, 2426-36 (2008).

106. F. Maldonado-Hodar, S. Morales-Torres, F. Ribeiro, et al. "Development of carbon coatings for cordierite foams: An alternative to cordierite honeycombs," Langmuir, 24, 3267-73 (2008).

107. C. Agrafiotis, A. Tsetsekou and A. Ekonomakou. "Effect of particle size on the adhesion properties of oxide washcoats on cordierite honeycombs," J. Mater. Sci. Lett., 18, 1421-4 (1999).

108. C. Agrafiotis and A. Tsetsekou. "Effect of powder characteristics on washcoat quality. Part II: zirconia, titania washcoats - multilayered structures," Journal of the European Ceramic Society, 20, 825-34 (2000).

109. C. Agrafiotis and A. Tsetsekou. "Deposition of meso-porous -alumina coatings on ceramic honeycombs by sol-gel methods," Journal of the European Ceramic Society, 22, 423-34 (2002).

110. G. Germani, A. Stefanescu, Y. Schuurman and A.C. van Veen. "Preparation and characterization of porous alumina-based catalyst coatings in microchannels," Chemical Engineering Science, 62, 5084-91 (2007).

111. X. Quan, H. Sun, S. Chen, H. Zhao and Y. Zhao. "Preparation of well-adhered -Al2O3 washcoat on metallic wire mesh monoliths by electrophoretic deposition," Appl. Surf. Sci., 253, 3303-10 (2007).

112. J. Jia, J. Zhou, J. Zhang, Z. Yuan and S. Wang. "The influence of preparative parameters on the adhesion of alumina washcoats deposited on metallic supports," Appl. Surf. Sci., 253, 9099-104 (2007).

113. V. Meille, S. Pallier and P. Rodriguez. "Reproducibility in the preparation of alumina slurries for washcoat application - role of temperature and particle size distribution," Colloids Surf. Physicochem. Eng. Aspects, 336, 104-9 (2009).

114. M. Cantoro, V.B. Golovko, S. Hofmann, et al. "Wet catalyst assisted growth of carbon nanofibers on complex three-dimensional substrates," Diamond and Related Materials, 14, 733-8 (2005).

115. L. Bonaccorsi, A. Freni, E. Proverbio, G. Restuccia and F. Russo. "Zeolite coated copper foams for heat pumping applications," Microporous and Mesoporous Materials, 91, 7-14 (2006).

116. F.C. Moates, T.E. McMinn and J.T. Richardson. "Radial reactor for trichloroethylene steam reforming," AICHE J., 45, 2411-8 (1999).

117. C. Delitala, M.D. Alba, A.I. Becerro, et al. "Synthesis of MCM-22 zeolites of different Si/Al ratio and their structural, morphological and textural characterisation," Microporous and Mesoporous Materials, 118, 1-10 (2009).

118. S. Maheshwari, E. Jordan, S. Kumar, et al. "Layer structure preservation during swelling, pillaring, and exfoliation of a zeolite precursor," J. Am. Chem. Soc., 130, 1507-16 (2008).

119. L.L. Landau B., "Dragging of a liquid by a moving plate," Acta Physicochimica U.R.S.S, XVII, 43-54 (1742).

120. D. Quere, *"Fluid coating on a fiber,"* pp. 347-84 in Vol. 31, Anonymous Annual Reviews Inc, Palo Alto, CA, United States, 1999.

121. M. Carmo, M. Linardi and J.G.R. Poco. "Characterization of nitric acid functionalized carbon black and its evaluation as electrocatalyst support for direct methanol fuel cell applications," Applied Catalysis A: General, 355, 132-8 (2009).

122. L.E. Scriven, "Physics and applications of dip coating and spin coating," Mater. Res. Soc. Symp. Proc., 121, 717-29 (1988).

123. D.E. Bornside, C.W. Macosko and L.E. Scriven. "Spin coating of a PMMA/chlorobenzene solution," J. Electrochem. Soc., 138, 317-20 (1991).

124. L. Villegas, F. Masset and N. Guilhaume. "Wet impregnation of alumina-washcoated monoliths: Effect of the drying procedure on Ni distribution and on autothermal reforming activity," Applied Catalysis A: General, 320, 43-55 (2007).